

Interfacing continuous and discrete Hilbert spaces in quantum optics and quantum information

by

Niranjan Sridhar

New Delhi, India

Bachelor of Technology, Engineering Physics, 2009
Indian Institute of Technology Bombay

A Dissertation presented to the Graduate Faculty of the University
of Virginia in Candidacy for the degree of Doctor of Philosophy

Department of Physics
University of Virginia

November 2015

UNIVERSITY OF VIRGINIA

Abstract

Department of Physics

Doctor of Philosophy

by Niranjan Sridhar

My doctoral thesis details my research on two major projects. Both projects investigate the correspondence between the discrete (photon number) and the continuous (quadrature) representation of optical states. Understanding the relationships between the two representations is very important for the investigation of quantum physics phenomena. Moreover it has significant applications in quantum computing where it is found that discrete-variable bases are easier to error-correct but some continuous-variable architectures are more scalable. Research in the connection between the two representation might help develop new architectures for scalable fault-tolerant quantum computing.

Acknowledgements

I have known I would be doing a PhD from a very young age. Even before I had stepped foot in University of Virginia, I had read and heard what I thought was everything to know about academia. Yet these last 6 years somehow still managed to surprise and annoy, delight and frustrate. And now near the end, I feel a sense of satisfaction, one that comes only from learning.

I hope that this acknowledgement, in some small way captures the gratitude I have for all the people in my life, the ones who have made this journey possible and enjoyable.

First and foremost, of course, I must thank my advisor Prof. Olivier Pfister. He represents everything that drove me to academia, a passionate teacher, an inspired scientist and a considerate advisor. Olivier has made every conversation in the last 5 years a learning experience, in more than just physics. He set high standards for everyone in the lab and then helped us achieve it without ever getting frustrated or impatient. If I take nothing else but a fraction of the zen-like patience Olivier has shown me, my PhD would have been worth it.

I must also thank our collaborators - Aaron Miller, Nick Menicucci, Rafael Alexander, Thomas Gerrits, Adriana Lita, Sae Woo Nam and his group at NIST and Saikat Guha, Jon Habif and their group at Raytheon BBN. Each one of them were vital contributors without whom our shared projects would not have been possible. I particularly enjoyed the conversations with Aaron, Nick and Saikat, who are all incredibly helpful and likeable, besides being stunningly brilliant scientists.

And of course I must thank my lab mates, who have been my companions in this voyage. Reihaneh Shahrokhshahi, for being my mentor in the lab and for having the most frank arguments I have ever had, you have my utmost respect. Moran Chen, by being an ally and a friend, by being so smart yet so direct, by centering discussions when they inexorably went too far off course, you were an invaluable anchor for our lab and me. And thank you Pei Wang, for many long conversations, for sharing many of my perspectives and interests, for being so diligent and for saving me from being outnumbered in the lab. Thank you also to Matt Pysher, Raphael Pooser, Russell Bloomer, Jietai Jing, and Hussain Zaidi who were always most helpful in our brief interactions.

I would like to thank my committee for taking the time to read my thesis and attend my defense. Throughout the years they have given me the gift of perspective by forcing me to analyze my work through a different lens. I would also like to thank all the staff and faculty at the physics department, particularly Dawn and Tammie Shifflett and Chris Floyd, for handling all my requests with generous care.

I want to thank all my friends I have found at UVa, my friends from undergraduate and beyond. Your friendship made the work fun, the good times cherished memories and the bad times tolerable.

Finally I would like to thank my parents. Everything I have ever done is a direct result of their tireless support and encouragement. Last but far from the least, I would like to thank my wife Sana, who fills every day of my life with the strength and the motivation to be a better person.

Contents

Abstract	i
Acknowledgements	ii
List of Figures	vii
Symbols	ix
1 Introduction	1
1.1 The Nature of Light	3
1.1.1 Light as a Harmonic Oscillator	3
1.1.2 Quadrature measurements	5
1.1.2.1 Homodyne detection	7
1.1.3 Photon number measurement	9
1.1.3.1 Photon-number-resolving detection	9
1.2 The Wigner function	10
1.3 Measurement of the Wigner function	18
1.3.1 Motivation and previous work	18
1.3.2 Quantum tomography by counting photons	20
1.4 Quantum Entanglement	21
1.5 Schwinger representation	24
1.5.1 Mathematical formulation	24
1.5.2 Physical meaning	24
1.5.3 Previous work	26
1.6 Summary	28
2 From Light to Spins	29
2.1 Introduction	29
2.1.1 Stabilizers and Nullifiers	29
2.2 Squeezed states to Spins : Bipartite case	31
2.2.1 Nullifiers, stabilizers and constants of the motion	31
2.2.2 Quantum evolution of Schwinger spin operators	33
2.3 Multipartite spin nullifiers	37
2.3.1 Three-spin systems	37
2.3.1.1 Three-Qmode chain	38

2.3.1.2	Thee-Qmode ring: CVGHZ state	39
2.3.2	Four-spin systems	40
2.3.2.1	Four-Qmode chain and ring CV states	40
2.3.2.2	Four-Qmode GHZ state	45
2.4	Multipartite spin entanglement	46
2.4.1	Derivation of the spin state for Qbits	46
2.4.2	Entanglement characterization	48
2.5	Effect of Non-Ideal Experimental Conditions	49
2.6	Conclusion	50
3	Tomography using photon-number-resolving detection	52
3.1	Photon-number-resolving detection setup	52
3.1.1	Signal acquisition	54
3.1.2	Signal processing and photon “pileups”	55
3.1.3	Detection efficiency	58
3.2	Experimental Setup	59
3.2.1	Displacement	59
3.2.2	Setup	61
3.2.3	Procedure	62
3.3	Results and analysis	63
3.3.1	Reconstruction	63
3.3.2	Verification	65
3.4	Conclusion	68
4	Conclusion	69
A	Derivation of the 4 spin entangled state	71
B	Quantum Computing with Schwinger Spins	77
B.1	General optics-spins framework	77
B.2	Quantum Computing with Spins	78
B.3	Error Correction with Spin operators	82
C	Programming and Data Analysis	83
C.1	ON/OFF script	83
C.2	Tomography	86
D	Quantum optics in the time domain	91
D.1	Introduction	91
D.1.1	Coherent states in time	93
D.2	Time evolution in the time domain	94
D.3	Interesting states in the time domain	94
D.3.1	Spontaneous Parametric Down-Conversion (SPDC)	94
D.3.2	SPDC with a filter cavity	96

D.3.2.1	Effect of cavity on modes in time domain	96
D.3.3	Hong-Ou-Mandel interference	99
D.4	Detection	101
D.4.1	Coherent State	103
D.4.2	SPDC	105
D.4.3	Hong-Ou-Mandel interference	110
D.4.4	HOM after filter cavity	113
D.5	Future Work	117
E	Fock state tomography	118
E.1	Generation of single photon state	119
E.1.1	Theory	119
E.1.2	Experiment	119
	Bibliography	122

List of Figures

1.1	Balanced Homodyne Detection	7
1.2	Wigner function of a vacuum state	13
1.3	Wigner function of Fock state $ n = 1\rangle$	14
1.4	Wigner function of coherent state with $\alpha = 2 + 2i$	15
1.5	Evolution of coherent state $ \alpha\rangle$ under a phase shift θ . As $ \alpha $ increases, $\Delta\theta$ decreases.	16
1.6	Wigner function of squeezed vacuum state with $r = 0.5$	17
1.7	Arbitrary spin measurements (along direction (θ, ϕ)) can be performed with a phase shift ϕ , two polarizing beamsplitters (PBS), a halfwave plate (HWP) whose axes are at $\theta/4$ rad from the PBSs, and two photon-number-resolving detectors (PNRD1,2).	26
2.1	Two sets of 2-mode squeezed states, 1-2 and 3-4, can be viewed through the Schwinger representation as 2 effective spins (blue ellipses). The black dots represent Qmodes and the red edges denote the non-zero G_{jk} terms in the squeezing Hamiltonian.	34
2.2	Two sets of 3 Qmodes, 1-3 and 4-6, cast as 3 effective spins (blue ellipses).	38
2.3	Two sets of 3 Qmodes, 1-3 and 4-6, as 3 effective spins (blue ellipses).	39
2.4	Chain H-graph, square cluster state, $H^{(0)}$	41
2.5	Square H-graph, square cluster state, $H^{(1)}$	41
2.6	Ring H-graph, $H^{(2)}$	41
2.7	The 4-mode Hamiltonians studied in this paper. The green edges denote a change sign in the corresponding two-mode squeezing term with respect to the red edges.	41
2.8	Two 4-Qmode GHZ states, 1-4 and 5-8, paired as 4 Schwinger spins (blue ellipses).	46
3.1	Principle of operation of the TES. When the TES is temperature-biased at the edge of the superconducting transition T_{bias} — or on the steep transition slope — any temperature variation δT due to photon absorption is translated into a measurable resistance change δR	53
3.2	An example of raw TES data showing a single photon detection event. The detection peak can be clearly distinguished from the noise.	54

3.3	Raw TES data for a CW beam showing distinct one-, two-, and three-photon peaks. The signal levels are indicated by the red dashed lines.	55
3.4	Steps in the processing of raw analog data into quantized photon-count data. (a), a small sample of the raw data. shows 3 single peaks and 1 “piled up” double peak, where the last photon was detected before the detector was cooled back the nominal bias temperature. (b), rising edge detection results. The procedure correctly detected 5 rising edges. (c), encoded signals, made of the photon detection times along with the value of the maximum peak height within $1.2 \mu\text{s}$ of each event. (d), final quantized photon-counts determined using the thresholds defined in the histogram of peak heights in Fig. 3.5.	57
3.5	Histogram of peak heights from the sample of Fig. 3.4(a). The histogram bins define the photon-number quantization thresholds.	58
3.6	Experimental setup for the quantum tomography of a coherent state using a coherent field input and photon number measurements. The signal optical path is that of the quantum state to be measured. The probe optical path is that of the “local oscillator” whose field generates the phase-space displacement. PBS: polarizing beam splitter; EOM: electro-optic modulator; HWP: halfwaveplate; ND: neutral density; HV = high voltage.	60
3.7	The measured Wigner functions and contours of, top, vacuum; center, a coherent state; bottom, a phase-diffused coherent state. All plots are interpolated for 22 amplitude points and 40 phase points.	64
3.8	Gaussian fit (top) and residuals (bottom) of the coherent-state tomographic data. The fit function was $W_{\text{fit}}(q, p) = a + b \exp[-m (q - q_0)^2 + (p - p_0)^2]$. The correlation coefficient was $R^2 = 0.966$	66
E.1	Type-II PPKTP crystal down-converts green photons into infra-red photon pairs used to create heralded Fock states	119
E.2	Type-II PPKTP crystal downconverts green photons into infra-red photon pairs used to create heralded Fock states	120

Symbols

P	phase quadrature	$\frac{a-a^\dagger}{i\sqrt{2}}$
Q	amplitude quadrature	$\frac{a+a^\dagger}{\sqrt{2}}$
N	number operator	$a^\dagger a$
A_θ	general quadrature	$ae^{i\theta} + a^\dagger e^{-i\theta}$
$H_n(x)$	n th order hermite polynomial in x	
$L_n(x)$	n th order laguerre polynomial in x	
$D(\alpha)$	displacement operator	$e^{\alpha a - \alpha^* a^\dagger}$
$S(\kappa t)$	squeezing operator	$e^{i\kappa t(a^2 - a^{\dagger 2})}$
BS	beam splitter	
FC	filter cavity	
LO	local oscillator	
CV	continuous variable	
CW	continuous wave	
ND	neutral density	
HWP	half-wave plate	
PBS	polarizing beam splitter	
EOM	electro-optic modulator	
FSR	free spectral range	
BHD	balanced homodyne detection	
TMSS	two-mode squeezed state	
PNR	photon-number-resolving	
APD	avalanche photo-diode	
TES	transition edge sensor	
MUS	minimum uncertainty state	
GKP	Gottesman-Kitaev-Preskill	
OPA	optical parametric amplifier	

OPO	optical parametric oscillator
EPR	Einstein-Podolski-Rosen
GHZ	Greenberger-Horne-Zeilinger
HOM	Hong-Ou-Mandel
PNRD	photon-number-resolving detection
FWHM	full width half maximum
H-graph	Hamiltonian graph
TMSS	two mode squeezed state
SPDC	spontaneous parametric down-conversion
PPKTP	periodically poled potassium titanyl phosphate

Chapter 1

Introduction

The nature of light has been a source of great fascination and controversy throughout history. Before the discovery of quantum physics, all physical objects were believed to be either particles or waves. The first modern mathematical description of light was Newton's corpuscular theory which treated light as a stream of particles. Particle theories of light are very successful at explaining certain phenomena like reflection and polarization. However they fail to provide a good description of many other optical phenomena. The wave theory of light, attributed to Huygens, had much more success explaining diffraction, interference, refraction and colors.

In 1845, Maxwell's theory of electromagnetism established what is now known as the classical theory of light. The success of the theory firmly established light as an electromagnetic wave. However over the next fifty years, certain newly discovered or proposed phenomena were found to be at odds with the theory, e.g. the photoelectric effect and the rather imaginatively named "ultraviolet catastrophe".

At the dawn of the twentieth century, in what is widely regarded as the seminal discovery leading to quantum physics, Max Planck realized that the catastrophe could be averted by assuming that light could only be absorbed in packets of energy or quanta. Albert Einstein took this idea and developed it into his explanation of the photoelectric effect treating light as a collection of particles or photons, a result that won him the Nobel Prize. Eventually with advancements in technology the discrete nature of light was experimentally verified using photographic plates that could detect individual photons.

The coming years saw the rapid development of quantum physics. According to quantum physics, the evolution of a physical object is described by the Schrodinger wave equation. The solution to the Schrodinger equation is called the wavefunction, which is not a directly measurable quantity but a distribution of probability amplitudes. The wavefunction describes the object completely, can be complex valued and the square modulus of the wavefunction gives the probability density function of physical attributes such as position or momentum. Thus every object is, in a sense, a wave. In the context of quantum optics, the continuous spatio-temporal distribution of the electromagnetic field constitutes the wavefunction of the photon. The wave-like properties of light such as interference and diffraction can be explained using the wavefunction.

However, as mentioned above, the quantum description of light is not complete without its particle nature. The quantization of the electromagnetic field using quantum electrodynamics provides the framework of treating light as a gas of bosonic particles or photons. The wavefunction can therefore be replaced by creation and annihilation of these photons, in direct analogy to atoms in quantum field theory. Thus, the energy of the electromagnetic field is proportional to the number of photons and the detection of light can only be done in these discrete units. Numerous phenomena such as the photoelectric effect and Compton scattering highlight the particle-like behaviour of photons.

This dichotomous behaviour is not an inconsistency but a central feature of quantum physics. Wave-particle, or continuous-discrete, duality is the cornerstone of our current understanding of how nature behaves. Theoretical and experimental demonstration of this duality is an important test of quantum physics and a useful tool for exploring new phenomena.

Moreover, using continuous and discrete Hilbert spaces together can provide new insights and opportunities in applications such as quantum computing and quantum information. Our ability to store and process information depends crucially on the physical system we use as the information carrier. The theoretical and experimental techniques vary widely over different technologies of generating and manipulating quantum systems. Exploring the continuous-discrete interface in the context of quantum information is therefore imperative in order to make full use of and further our current understanding of the quantum world.

1.1 The Nature of Light

In this section, we will provide some background information of quantum optics that are relevant to this thesis. The references for the following sections are Prof. Olivier's notes from Quantum Optics and Quantum Information course [1] and D. F. Walls and G. J. Milburn's Quantum Optics [2].

1.1.1 Light as a Harmonic Oscillator

Today, the nature of light is firmly established as a quantum harmonic oscillator. A mode of light is characterized by the frequency, ω , of oscillation of its electro-magnetic field \vec{E} , the field polarization \hat{e} and the direction of propagation or wavevector \hat{k} . Each mode is an independent quantum harmonic oscillator. The number of photons in the field mode is the excitation level of the harmonic oscillator. Each photon is a packet of energy $\hbar\omega$, where \hbar is the Planck's constant, corresponding to a single level difference of a harmonic oscillator. The allowed frequencies of the mode are decided by the harmonic oscillator potential given by the time independent Schrödinger equation for the mode.

The time-independent Schrödinger equation for a harmonic oscillator is

$$H\psi(x) = \left(\frac{P^2}{2m} + \frac{kX^2}{2} \right) \psi(x) = E\psi(x).$$

In the context of optics, position and momentum of the harmonic oscillator correspond to the amplitude (Q) and phase (P) quadrature, respectively. We can define these quadratures from the above equation by setting $Q \rightarrow X\sqrt{\frac{k}{\hbar\omega}}$ and redefining $P \rightarrow P\sqrt{\frac{1}{m\hbar\omega}}$ to get

$$H = \frac{\hbar\omega}{2}(Q^2 + P^2). \quad (1.1)$$

We can define ladder operators as the annihilation operator, a , and creation operator, a^\dagger ,

$$\begin{aligned} a &= \frac{1}{\sqrt{2}}(Q + iP), \\ a^\dagger &= \frac{1}{\sqrt{2}}(Q - iP), \\ \implies H &= \hbar\omega(a^\dagger a + 1/2), \end{aligned} \quad (1.2)$$

where a, a^\dagger are mutually adjoint operators which follow the bosonic commutation relation $[a, a^\dagger] = 1$. Operators of two different harmonic oscillators commute with each other giving us the general commutation relation

$$[a_i, a_j^\dagger] = \delta_{i,j} = \delta(\omega_i - \omega_j) \delta(k_i - k_j) \delta_{\hat{e}_i, \hat{e}_j}. \quad (1.3)$$

The allowed energy values of this Hamiltonian are quantized as

$$E_n = \hbar\omega \left(n + \frac{1}{2} \right), \quad (1.4)$$

where n is an integer representing the number of photons in the mode and the eigenvalue of the operator N ,

$$N = a^\dagger a, \quad (1.5)$$

known as the photon number operator. The creation and annihilation operators are not Hermitian and therefore do not correspond to any observables that we can measure. However we can see the physical meaning of these operators.

The quantized electromagnetic field \mathbf{E} can be written as a function of path \mathbf{r} and time t as

$$\begin{aligned} \mathbf{E}_{\omega,k}(\mathbf{r}, t) &= \sqrt{\frac{\hbar\omega}{2V\epsilon}} \left(a_{\omega,k} e^{i(\mathbf{k}\cdot\mathbf{r} - \omega t - \theta)} + a_{\omega,k}^\dagger e^{-i(\mathbf{k}\cdot\mathbf{r} - \omega t - \theta)} \right), \\ &= E_{\omega,k}^0 \left(a_{\omega,k} e^{i(\mathbf{k}\cdot\mathbf{r} - \omega t - \theta)} + a_{\omega,k}^\dagger e^{-i(\mathbf{k}\cdot\mathbf{r} - \omega t - \theta)} \right), \end{aligned} \quad (1.6)$$

$$= \sqrt{2}E_{\omega,k}^0 (Q_{\omega,k} \cos(\mathbf{k} \cdot \mathbf{r} - \omega t - \theta) - P_{\omega,k} \sin(\mathbf{k} \cdot \mathbf{r} - \omega t - \theta)), \quad (1.7)$$

using Eq. (1.2). It is then clear that Q and P correspond to the real and imaginary parts of the normalized quantized electromagnetic field since,

$$Q = \frac{a + a^\dagger}{\sqrt{2}} = \frac{E_{\omega,k}(0, 0, 0)}{\sqrt{2}E_{\omega,k}^0}, \quad (1.8)$$

$$P = \frac{a - a^\dagger}{i\sqrt{2}} = \frac{E_{\omega,k}(0, 0, \frac{\pi}{2})}{\sqrt{2}E_{\omega,k}^0}. \quad (1.9)$$

Using the commutation relation Eq. (1.3), we can see that

$$[Q_i, P_j] = i\delta_{i,j} = i\delta(\omega_i - \omega_j) \delta(k_i - k_j) \delta_{\hat{e}_i, \hat{e}_j}. \quad (1.10)$$

Therefore Q and P are the quadrature components of the electromagnetic field vector. A $\frac{\pi}{2}$ phase evolution on the mode transforms Q into P and P into $-Q$ in close analogy with the phase evolution of the classical rotating electromagnetic field. The generalized quadrature, A_θ is then simply the electromagnetic field rotated by an arbitrary phase shift,

$$A_\theta = \frac{E(0, 0, \theta)}{\sqrt{2}E_{\omega,k}^0} = \frac{1}{\sqrt{2}} (ae^{-i\theta} + a^\dagger e^{i\theta}). \quad (1.11)$$

We can measure the intensity and the amplitude of the electromagnetic field by measuring the photon number and the quadratures, which are Hermitian operators and therefore correspond to real-valued observables.

1.1.2 Quadrature measurements

Quadrature measurement results can, in theory, be any real value between $-\infty$ to ∞ . We denote $|q\rangle, |p\rangle$ that are eigenstates of the quadrature operators Q, P ,

$$Q|q\rangle = q|q\rangle, \quad P|p\rangle = p|p\rangle. \quad (1.12)$$

The bases $|q\rangle, |p\rangle$ are complete, orthogonal bases, meaning we can write any state as a superposition of orthogonal vectors, i.e

$$\begin{aligned}\langle q | q' \rangle &= \delta(q - q'), & \langle p | p' \rangle &= \delta(p - p'), \\ \int_{-\infty}^{\infty} dq |q\rangle \langle q| &= \int_{-\infty}^{\infty} dp |p\rangle \langle p| = 1, \\ |\psi\rangle &= \int_{-\infty}^{\infty} dq |q\rangle \langle q | \psi \rangle = \int_{-\infty}^{\infty} dq \psi(q) |q\rangle \\ |\psi\rangle &= \int_{-\infty}^{\infty} dp |p\rangle \langle p | \psi \rangle = \int_{-\infty}^{\infty} dp \tilde{\psi}(p) |p\rangle\end{aligned}$$

Like their position and momentum analogues, the q and p bases are related by Fourier transform,

$$\tilde{\psi}(p) = \frac{1}{\sqrt{2\pi}} \int_{-\infty}^{\infty} \psi(q) e^{-iqp} dq. \quad (1.13)$$

Amplitude quadrature measurements give us expectation value and variance,

$$\begin{aligned}\langle \psi | Q | \psi \rangle &= \int_{-\infty}^{\infty} dq' \psi^*(q') \langle q' | Q \int_{-\infty}^{\infty} dq \psi(q) |q\rangle \\ &= \int_{-\infty}^{\infty} dq |\psi(q)|^2 q \\ \langle \psi | Q^2 | \psi \rangle &= \int_{-\infty}^{\infty} dq' \psi^*(q') \langle q' | Q^2 \int_{-\infty}^{\infty} dq \psi(q) |q\rangle \\ &= \int_{-\infty}^{\infty} dq |\psi(q)|^2 q^2 \\ (\Delta Q)^2 &= \langle \psi | Q^2 | \psi \rangle - \langle \psi | Q | \psi \rangle^2\end{aligned} \quad (1.14)$$

The commutation relation $[Q, P] = i$, implies that both P and Q cannot be measured on the state simultaneously. This translates into the corresponding Heisenberg inequality

$$\Delta Q \Delta P \geq 1/2. \quad (1.15)$$

For an pure amplitude eigenstate $|q_0\rangle$, i.e a state with $\psi(q) = \delta(q - q_0)$, the variance $\Delta Q = 0$, hence $\Delta P \rightarrow \infty$.

1.1.2.1 Homodyne detection

Quadrature measurements are commonly made using homodyne detection. Homodyne measurement employs an optical element called the beamsplitter (BS) which is simply a partially reflecting mirror.

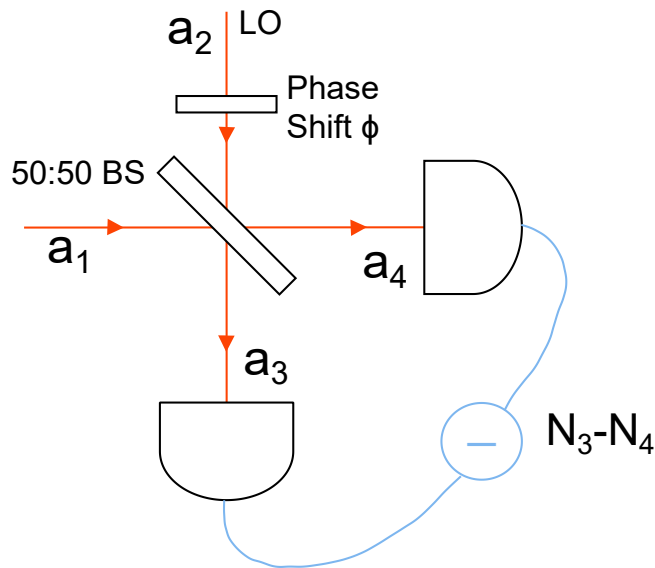


FIGURE 1.1: Balanced Homodyne Detection

A BS takes two optical modes a_1, a_2 in and puts two modes a_3, a_4 out. In practice, this requires the two input optical modes to be aligned at the BS such that the output modes at each port are perfectly matched. At the BS, each photon of each mode goes to either one of the two output modes with a probability decided by the characteristics of the BS. The quantum Hamiltonian of the BS and its effective transformation on the modes are given by,

$$H_{BS} = \hbar\kappa(a_1a_2^\dagger + a_1^\dagger a_2) \quad (1.16)$$

$$a_3 = a_1 \cos \kappa t + a_2 \sin \kappa t \quad (1.17)$$

$$a_4 = a_1 \sin \kappa t - a_2 \cos \kappa t \quad (1.18)$$

Therefore by controlling κ, t we can control the degree of mixing between modes a_1 and a_2 . We can pose that $\sin \kappa t$ is the reflectivity ρ and $\cos \kappa t$ is the transmissivity

τ so that $\rho^2 + \tau^2 = 1$. Now we can understand homodyne detection, which we will just briefly outline.

We shall only look at balanced homodyne detection (BHD) so $\rho = \tau = \frac{1}{\sqrt{2}}$. The two detectors at the output of the BS measure the photon number at the output, which can be written in terms of the input as

$$\begin{aligned} a_3^\dagger a_3 &= \frac{1}{2}(a_1^\dagger + a_2^\dagger)(a_1 + a_2), \\ N_3 &= \frac{1}{2}(a_1^\dagger a_1 + a_2^\dagger a_2 + a_1 a_2^\dagger + a_1^\dagger a_2), \\ a_4^\dagger a_4 &= \frac{1}{2}(a_1^\dagger - a_2^\dagger)(a_1 - a_2), \\ N_4 &= \frac{1}{2}(a_1^\dagger a_1 + a_2^\dagger a_2 - a_1 a_2^\dagger - a_1^\dagger a_2), \\ N_+ &= N_3 + N_4 = a_1^\dagger a_1 + a_2^\dagger a_2, \end{aligned} \tag{1.19}$$

$$N_- = N_3 - N_4 = a_1 a_2^\dagger + a_1^\dagger a_2, \tag{1.20}$$

where N_+ , N_- denote the sum and difference of the photon number measured at the two outputs.

Now if a_1 is the quantum state we want to measure, then the key here is to make the a_2 a bright classical field in a coherent state. The coherent state mode is also known as the local oscillator (LO). We shall explore coherent states further in section 1.2, but here it suffices to mention that a coherent state $|\beta\rangle$ is an eigenstate of the annihilation operator. We have $\langle\beta|a|\beta\rangle = \beta$ and $\langle\beta|a^\dagger|\beta\rangle = \beta^*$, where $\beta = |\beta|e^{i\theta}$, $|\beta|^2$ is the mean intensity and θ is the phase of the mode. Now the effective difference measurement becomes

$$\begin{aligned} \langle N_- \rangle &= {}_2\langle\beta|{}_1\langle\psi|a_1 a_2^\dagger + a_1^\dagger a_2|\psi\rangle_1|\beta\rangle_2 \\ &= |\beta|{}_1\langle\psi|(a_1 e^{-i\theta} + a_1^\dagger e^{i\theta})|\psi\rangle_1 \\ &= \sqrt{2}|\beta|\langle A_\theta \rangle. \end{aligned} \tag{1.21}$$

Since $|\beta|$ is a known classical field, measurement of the photon number difference is a direct measurement of generalized quadrature A_θ . Using the phase of the local oscillator in mode a_2 we can measure any quadrature of mode a_1 , so that $\theta = 0$ corresponds to Q and $\theta = \pi/2$ corresponds to P.

1.1.3 Photon number measurement

Now let's look at the discrete space. The photon number can, in theory, take whole number values from 0 to ∞ . The eigenstates of the number operator are simply the energy eigenstates of the harmonic oscillator. Eigenstates of the number operator $|n\rangle$ have energy $\hbar\omega(n + \frac{1}{2})$. The $\frac{\hbar\omega}{2}$ term is known as zero point energy and is the energy of the ground state ($n = 0$). This energy is not measurable or convertible into work, and hence we can drop it out of the energy terms from here on. The number states are the energy eigenstates of the harmonic oscillator or Fock states,

$$N|n\rangle = a^\dagger a|n\rangle = n|n\rangle \quad (1.22)$$

Fock states are orthogonal $\langle n|m\rangle = \delta_{mn}$, and form a complete basis i.e we can write any state ψ as a superposition of Fock states.

$$\begin{aligned} \sum_{n=0}^{\infty} |n\rangle \langle n| &= 1, \\ |\psi\rangle &= \sum_{n=0}^{\infty} c_n |n\rangle, \end{aligned} \quad (1.23)$$

where $c_n = \langle n|\psi\rangle$. The creation and annihilation operator increase and decrease the photon number respectively,

$$a|n\rangle = \sqrt{n}|n-1\rangle \quad (1.24)$$

$$a^\dagger|n\rangle = \sqrt{n+1}|n+1\rangle \quad (1.25)$$

Photon-number-resolving measurements collapse the wavefunction of the measured state to the Fock state basis.

1.1.3.1 Photon-number-resolving detection

As noted above, even homodyne measurement requires photon number measurements. However the devices commonly used for quadrature measurements, such as silicon and InGaAs photo-diodes, are not used for photon number measurements. This is because these detectors can only resolve photo-currents of the order of 10^8 photons per second because of substantial dark current. The large photon numbers and statistical errors wash out the quantum properties of the photon number

measurement, instead these detector can be said to be measuring field intensities. As we saw in Eq. (1.21), homodyne detection operates in the regime of bright classical fields. The LO amplifies the quantum signal of quadrature measurement by the coherent field magnitude and thus these detectors can be used very well for homodyne measurements.

True photon number resolving measurement turns out to be a very difficult engineering problem, one that nevertheless has seen great progress in recent years. Until recently photon number measurement could only be done using single photon detectors such as avalanche photo-diodes (APD). APD's are extremely sensitive, their noise is below the single photon level. However they have no resolution i.e they cannot differentiate between 1 and 2 or n photons and they have low quantum efficiency i.e they miss a lot of photons. While these might seem like fatal problems, APD's have been used widely as photon number measurement devices in post-selection experiments where only 0 or 1 photon is expected. A post-selection measurement is a conditional measurement conditioned upon an event, which for an APD is a photon detection event. This ensures that only the detection events are counted and the loss of the APD is neglected. As long as the probability of encountering higher photon numbers is negligible, an APD is a legitimate photon number measurement.

Sae Woo Nam's group at the National Institute of Standards and Technology in Boulder, Colorado has recently developed a new superconducting transition edge sensor detector that can resolve photon numbers between 1 and 5 photons at 1064 nm with 95 % quantum efficiency [3]. We collaborated with Sae Woo Nam's group and with funding from an NSF Major Research Instrumentation grant, acquired one 8-channel TES detector which is currently in our lab at University of Virginia. The working principle of the detector is elaborated in section 3 .

1.2 The Wigner function

The Wigner quasi-probability distribution or the Wigner function was first introduced by Eugene Wigner [4] in 1932 to study quantum corrections to classical statistical mechanics. It is a mapping of the complex wavefunction onto a real

valued function in the phase space of Hermitian operators, define as,

$$W(q, p) = \frac{1}{\pi} \int_{-\infty}^{\infty} \psi^*(q + y)\psi(q - y)e^{2ipy} dy \quad (1.26)$$

where ψ is the wavefunction and q and p are amplitude and phase quadrature here but could be any conjugate variable pair.

The Wigner function integrated along any variable, i.e the marginal distribution, yields the measurement distribution of the conjugate variable,

$$\int_{-\infty}^{\infty} W(q, p) dp = |\psi(q)|^2. \quad (1.27)$$

For an ensemble of classical particles, the probability distribution informs us about the probability of finding a particle in a given location in phase space. The Wigner function plays an analogous role for quantum states and provides a very descriptive way to see the distinction between classical and quantum states.

A classical state is one that can be described using classical physics. The Wigner function of such a state is a positive definite distribution.

Certain phenomena such as non-zero variances for quadratures due to Heisenberg inequality cannot be described classically. Another example of non-classical state is the squeezed state that we will see in the next section. However, these can still be explained using Wigner functions that are positive everywhere. The properties of such states, despite being non-classical, could in principle be described as probability distributions of ensembles.

However some quantum states (such as Fock states) can have Wigner functions with negative values, which can never happen with a probability distribution. Therefore, the Wigner function taking negative values is considered a signature of quantum physics.

We look at some of these states that are commonly encountered in quantum optics in both the continuous and discrete Hilbert spaces and their Wigner functions.

Vacuum state

The vacuum state is ground state of the quantum harmonic oscillator. A field in vacuum state has zero photons i.e it has no light. The vacuum state is represented as $|0\rangle$ in the photon number basis. In the amplitude quadrature basis, the vacuum state is given by a Gaussian wavefunction

$$\begin{aligned} |0\rangle &= \int_{-\infty}^{\infty} |q\rangle \langle q| 0\rangle \\ &= (\pi)^{-1/4} \int_{-\infty}^{\infty} e^{-q^2/2} |q\rangle. \end{aligned} \quad (1.28)$$

Thus the vacuum state has a non-zero electromagnetic field distribution, even though it has zero photons. Indeed,

$$\begin{aligned} \langle 0 | (\Delta Q)^2 | 0 \rangle &= \langle 0 | Q^2 | 0 \rangle - \langle 0 | Q | 0 \rangle^2 \\ &= 1/2 - 0 = 1/2 \end{aligned} \quad (1.29)$$

We could also write the vacuum state in the phase quadrature basis, and similarly get $(\Delta P)^2 = 1/2$. Thus $\Delta Q \Delta P = 1/2$, the lowest value allowed by Heisenberg inequality making the vacuum state a minimum uncertainty state (MUS). This variance in the quadrature measurement is also known as “shot noise”.

A mode cannot have less than zero photons, thus the vacuum state is nullified by the annihilation operator

$$a|0\rangle = 0 \quad (1.30)$$

We can find the Wigner function of this state

$$\begin{aligned} W(q, p) &= \frac{1}{\pi^{3/2}} \int_{-\infty}^{\infty} e^{-(q+y)^2/2} e^{-(q-y)^2/2} e^{2ipy} dy \\ &= \frac{1}{\pi} e^{-q^2 - p^2} \end{aligned} \quad (1.31)$$

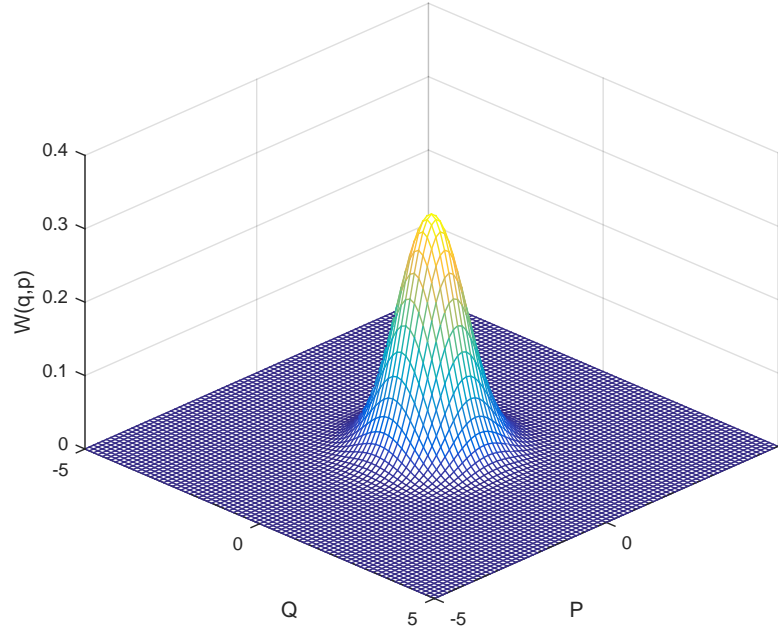


FIGURE 1.2: Wigner function of a vacuum state

Fock state

An n photon state, also known as a Fock state $|n\rangle$, has an n^{th} order Hermite polynomial distribution in amplitude and phase. As mentioned above, creation and annihilation operators transition between Fock states by raising and lowering the excitation level respectively. We use the Hermite polynomial expression of the quadrature-Fock Clebsch-Gordan coefficients [5] to express the Fock state in the quadrature basis,

$$\langle q|n\rangle = \pi^{-\frac{1}{4}}(2^n n!)^{-\frac{1}{2}} e^{-\frac{q^2}{2}} H_n(q), \quad (1.32)$$

where $H_n(q)$ is the Hermite polynomial of order n .

$$\begin{aligned} |n\rangle &= \int_{-\infty}^{\infty} |q\rangle \langle q|n\rangle \\ &= \pi^{-\frac{1}{4}}(2^n n!)^{-\frac{1}{2}} \int_{-\infty}^{\infty} e^{-\frac{q^2}{2}} H_n(q) |q\rangle \end{aligned} \quad (1.33)$$

The Wigner function of a Fock state is

$$\begin{aligned} W(q,p) &= \pi^{-\frac{1}{2}}(2^n n!)^{-1} \frac{1}{\pi} \int_{-\infty}^{\infty} e^{-\frac{(q+y)^2}{2}} H_n(q+y) e^{-\frac{(q-y)^2}{2}} H_n(q-y) e^{2ipy} dy \\ &= \frac{(-1)^n}{\pi} e^{-(q^2+p^2)} L_n(2(q^2+p^2)) \end{aligned} \quad (1.34)$$

where L_n is the Laguerre-Gaussian polynomial of order n . We can see that vacuum

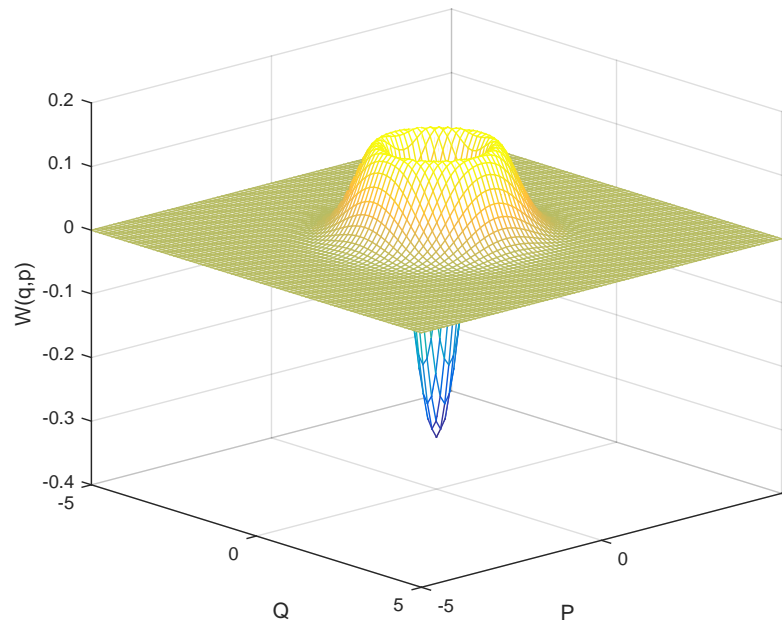


FIGURE 1.3: Wigner function of Fock state $|n = 1\rangle$

and Fock states are symmetric under rotations in phase space. Optical phase shifts are rotations in quadrature phase space, therefore vacuum and Fock states are invariant under optical phase shifts.

Intuitively we can think of Fock states as the signature of quantization of energy and therefore a proof of the quantum nature of light.

Coherent state

Coherent state can be obtained by the action of the displacement operator, $D(\alpha) = e^{\alpha a^\dagger - \alpha^* a}$ on the vacuum state.

$$\begin{aligned} |\alpha\rangle &= D(\alpha)|0\rangle \\ |\alpha\rangle &= e^{-|\alpha|^2/2} \sum_{n=0}^{\infty} \frac{\alpha^n}{\sqrt{n!}} |n\rangle \end{aligned} \quad (1.35)$$

The coherent state is an eigenstate of the annihilation operator

$$a|\alpha\rangle = \alpha|\alpha\rangle. \quad (1.36)$$

Hence the coherent state subjected to losses stays a coherent state. If the displacement parameter α is zero, then the resultant coherent state is simply the vacuum state. The Wigner function of the coherent state is a Gaussian function identical to the vacuum state, only displaced from the origin

$$W(q, p) = \frac{1}{\pi} e^{-(q - \text{Re}(\alpha))^2 - (p - \text{Im}(\alpha))^2} \quad (1.37)$$

Note that this state is not identical under phase shift. A phase shift would rotate

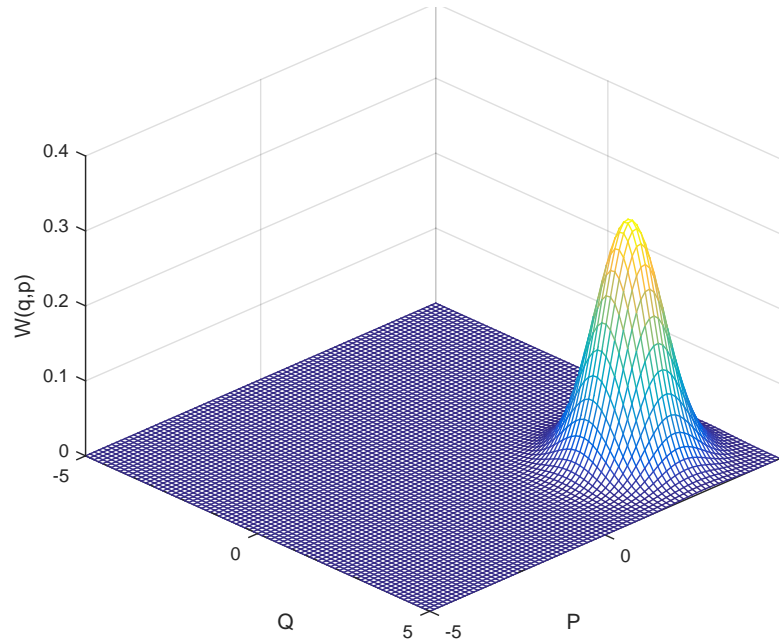


FIGURE 1.4: Wigner function of coherent state with $\alpha = 2 + 2i$

the state with respect to the coordinates by the angle of the phase shift. In fact the larger the displacement from the origin, the higher is the resolution of the angular distance. Therefore we can intuitively see why bright coherent states are used as phase references.

Squeezed state

A squeezed-vacuum light source, can be created by a process that creates photons in pairs. A commonly used method is parametric down-conversion in a nonlinear crystal such as periodically poled Potassium titanyl phosphate (PPKTP). Focusing a green coherent state in a PPKTP crystal causes it to convert green photons into two infrared (IR) photons. Since the IR photons are always emitted in pairs, the

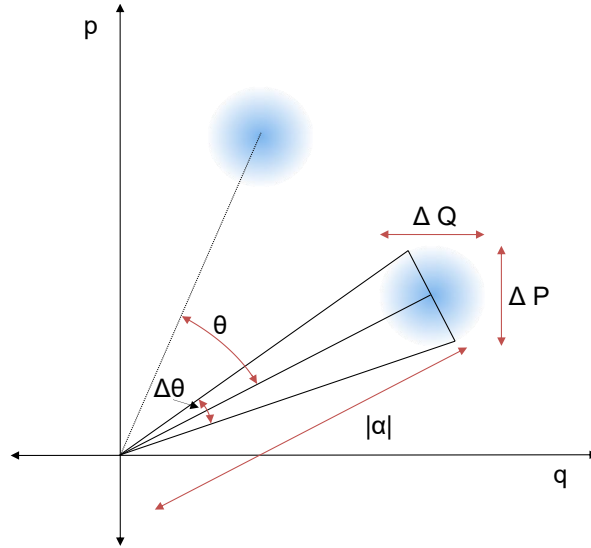


FIGURE 1.5: Evolution of coherent state $|\alpha\rangle$ under a phase shift θ . As $|\alpha|$ increases, $\Delta\theta$ decreases.

IR generation Hamiltonian can be described as,

$$H = \frac{i\hbar\kappa}{2}(a^{\dagger 2} - a^2) \quad (1.38)$$

Here $a^{\dagger 2}$ is the two-photon creation operator and a^2 is the two-photon annihilation operator. The squeezed state can be obtained by the evolving the initial state with the squeezing Hamiltonian, i.e applying $S(\kappa t) = e^{-\frac{\kappa t}{2}(a^{\dagger 2} - a^2)}$ on the vacuum state.

$$\begin{aligned} |r\rangle &= S(r)|0\rangle, \\ |r\rangle &= \frac{1}{\cosh r} \sum_{n=0}^{\infty} \tanh^n r |2n\rangle, \end{aligned} \quad (1.39)$$

where $r = \kappa t$. We find that for the squeezed state,

$$(\Delta Q)^2 = e^{-2r}, \quad (\Delta P)^2 = e^{2r}. \quad (1.40)$$

We see that the variance in one quadrature is squeezed and the variance in the conjugate quadrature is anti-squeezed, hence the name squeezed state. In the limit of $r \rightarrow \infty$, a squeezed state becomes a quadrature eigenstate $|q=0\rangle$.

The Wigner function of a squeezed state is shown in Fig. 1.6. As we can see it is still a positive definite Gaussian function although it is not symmetric in q and p .

Squeezed vacuum is a special case of the set of all squeezed states which are formed by the action of the squeezing operator on a general state.

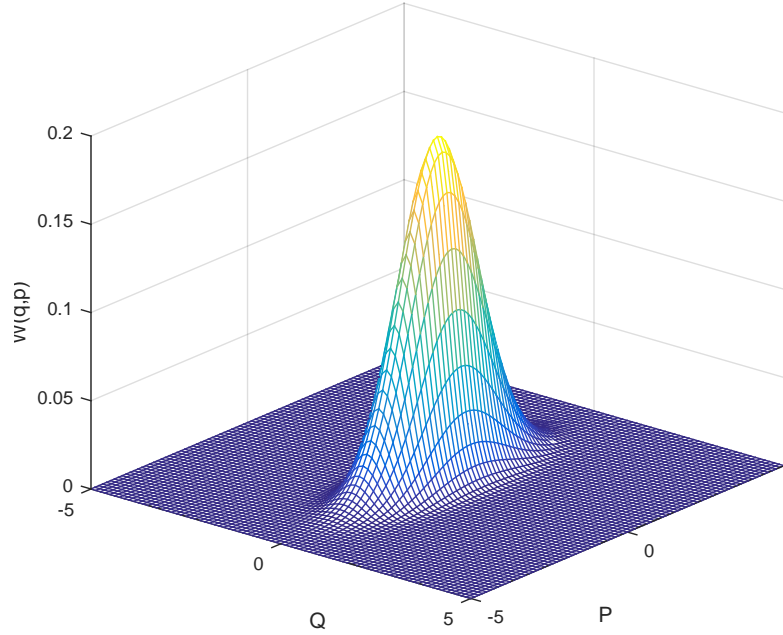


FIGURE 1.6: Wigner function of squeezed vacuum state with $r = 0.5$

Two-mode squeezed state

A two-mode squeezed state, or TMSS, can be created using a process that creates photons in pairs in different modes. Type-II PPKTP crystals, for example, emit photon pairs where one photon is horizontally polarized and one is vertically polarized. Therefore the Hamiltonian for this process is given by

$$H = i\hbar\kappa(a_1^\dagger a_2^\dagger - a_1 a_2). \quad (1.41)$$

The two mode squeezed state can be obtained by evolving the initial two mode state by the Hamiltonian. Applying $S_{12}(\kappa t) = \exp(-\kappa t(a_1^\dagger a_2^\dagger - a_1 a_2))$ on the vacuum state, we get

$$\begin{aligned} |r\rangle_{12} &= S_{12}(r) |0\rangle_1 |0\rangle_2 \\ |r\rangle_{12} &= \frac{1}{\cosh r} \sum_{n=0}^{\infty} \tanh^n r |n\rangle_1 |n\rangle_2 \end{aligned} \quad (1.42)$$

where $r = \kappa t$. The variances of individual mode quadratures are large, but since the two mode are not separable, we can check the variances of two mode operators.

$$\begin{aligned} \Delta(Q_1 \pm Q_2) &= e^{\pm r} \\ \Delta(P_1 \pm P_2) &= e^{\mp r} \end{aligned} \quad (1.43)$$

In a two-mode squeezed state (TMSS), its the sums and differences of quadratures of the two modes that are squeezed and anti-squeezed. In the limit of infinite squeezing $r \rightarrow \infty$, we have $e^{-r} \rightarrow 0$ and therefore

$$Q_1 = Q_2, \quad P_1 = -P_2. \quad (1.44)$$

This is the optical analogue of the canonical Einstein-Podolsky-Rosen (EPR) state [6, 7], hence the TMSS is also known as the EPR state. The EPR state is an example of an entangled state and will be explored further in chapter 2. The Wigner function of two mode states is four-dimensional but still Gaussian in the $(Q_1 - Q_2, P_1 + P_2)$ subspace.

1.3 Measurement of the Wigner function

1.3.1 Motivation and previous work

The complete characterization of the quantum state, a.k.a. quantum state tomography or quantum tomography, of a physical system plays a key role in physics. As newer experiments and techniques allow the generation of more exotic states, tomography becomes very important to quantify and certify the success of such techniques. This is particularly important in quantum information and quantum computing applications where the success of the information processing and error correction depends on characteristics of the quantum resources [8].

Measurement of a single observable does not uniquely identify a quantum state. For example, even though $\frac{1}{\sqrt{2}}(|0\rangle + |1\rangle)$ and $\frac{1}{\sqrt{2}}(|0\rangle - |1\rangle)$ are two distinct quantum states, they have the same distribution of measurement results in the logical basis, 0 with 50% probability and 1 with 50% probability. On the other hand, the wavefunction and Wigner function can both determine a state uniquely. However the wavefunction is complex valued, and as such is not an observable. The Wigner function however, is a well behaved, real-valued function which can be measured.

Measurement of Wigner function by transforming the canonically conjugate quadrature amplitude measurements is well known. Using the measurement histograms of a sufficient number of rotated field quadratures, the Wigner function can be

reconstructed using rather involved numerical inverse Radon transform postprocessing [9, 10, 11]. As this method requires quadrature measurements, it is also known as optical homodyne tomography.

An alternate and more direct method to measure the Wigner function, free of the encumbrance of the reconstruction process [12], was first proposed by Antoine Royer [13] in 1976. It was later demonstrated experimentally in atomic states by Dietrich Leibfried et al [14], and for optical states by Banaszek and Wódkiewicz [15]. The optical state tomography which we shall focus on in this thesis relies on ideal photon counting, a.k.a. photon-number-resolving (PNR) detection. As mentioned before, PNR detection is difficult to achieve and a good method to circumvent this experimental difficulty has been to use detectors with single-photon sensitivity, such as APD's and work at photon fluxes low enough that there would be a negligible probability of more than one photon in the detection's temporal window. Under such conditions, Banaszek et al. demonstrated coherent-state quantum tomography [16], with an effective restriction to the $\{|0\rangle, |1\rangle\}$ subset of the Fock basis.

In this work, we reproduced Banaszek et al.'s seminal experiment and extended it, we believe for the first time, to the regime where much more than one photon is present in the detection window. Our PNR detector was a superconducting transition-edge sensor (TES), of system detection efficiency above 90% [3]. These detectors can distinguish between 0 to 5-photon Fock states at 1064 nm with high system detection efficiency, no dead time, and near zero dark count. Therefore only the TES can measure the state without any fair sampling assumption. We believe this to be a step towards more direct state reconstruction of non-classical states (i.e., with minimal numerical postprocessing) which, to the best of our knowledge, has not yet been achieved.

Here we outline the theoretical foundation proposed by Royer and adapted by Banaszek et al for optical quantum tomography with PNR measurements.

1.3.2 Quantum tomography by counting photons

The Wigner function [4] of a single mode of the quantum electromagnetic field of density operator ρ can be alternatively written [10] as

$$W(q, p) = \frac{1}{\pi} \int_{-\infty}^{\infty} e^{2iyp} \langle q - y | \rho | q + y \rangle dy, \quad (1.45)$$

where $|q \pm y\rangle$ belong to the amplitude quadrature eigenbasis. This is a generalization of the Wigner function definition in Eq. (1.26) to include statistical mixtures described by a density operator ρ . For pure states $|\psi\rangle$ the density operator simply becomes $\rho = |\psi\rangle\langle\psi|$ and Eq. (1.45) reduces to Eq. (1.26). Now if we write $\rho = \sum_{n,n'} \rho_{nn'} |n\rangle\langle n'|$ in the Fock basis and use the Hermite polynomial expression, it is then straightforward to obtain the following remarkable relation from the orthogonality of Hermite polynomials

$$\begin{aligned} W(q, p) &= \frac{1}{\pi} \int_{-\infty}^{\infty} e^{2iyp} \sum_{\{n,n'\}=0}^{\infty} \langle q - y | n \rangle \rho_{nn'} \langle n | q + y \rangle dy, \\ W(0, 0) &= \frac{1}{\pi} \sum_{\{n,n'\}=0}^{\infty} \rho_{nn'} \int_{-\infty}^{\infty} \frac{dy}{\sqrt{\pi} 2^n n!} H_n(-y) H_{n'}(y) e^{-y^2}, \\ W(0, 0) &= \frac{1}{\pi} \sum_n^{\infty} (-1)^n \rho_{nn} \\ &= \frac{1}{\pi} \langle \psi | \left(\sum_n (-1)^n |n\rangle\langle n| \right) | \psi \rangle = \frac{1}{\pi} \langle \Pi \rangle. \end{aligned} \quad (1.46)$$

Here the right-hand side can be construed as the expectation value of the operator $\Pi = \sum_n (-1)^n |n\rangle\langle n|$, the photon-number parity operator. Since ρ_{nn} is the probability of counting n photons in ρ , it is therefore clear that the value of the Wigner function at the origin can be obtained directly from the statistics of ideal PNR measurements. The Wigner function in the rest of the quantum phase space is then accessed by simply displacing the quantum state ρ . The displacement operator we encountered in section 1.2, when applied on an arbitrary state $|\psi\rangle$ with Wigner function $W(q, p)$ has the effect of displacing the Wigner function to $W_{disp}(q + Re(\alpha), p + Im(\alpha))$. Therefore

$$W_{disp}(0, 0) = W(-Re(\alpha), -Im(\alpha)) \quad (1.47)$$

Thus displacing the quantum state by α and measuring the parity measure (Eq. (1.46)) of the resultant state gives us the $W(-\alpha)$ of the original state. By scanning the displacement parameter α we can measure the Wigner function at every point in phase space.

This method therefore directly gives us entire Wigner function of a state and no back-projection algorithms are required. This reduces not only the mathematical overhead but also makes the complete characterization of a quantum state directly accessible by measurement. We will use this theoretical foundation in our experiment which will be detailed in chapter 3.

1.4 Quantum Entanglement

Quantum entanglement is the source of some of the most counter-intuitive and well-known quantum phenomena. Indeed violation of the Bell inequality [17], one of the most celebrated tests of the completeness of quantum mechanics, requires entangled systems.

A quantum system is said to be an entangled state if it is made of two or more physical systems but cannot be factorized into states of the separate subsystems.

As with many other quantum properties, entanglement can be demonstrated in both continuous- and discrete-variable systems. The simplest discrete system is a two level system, called Qbit¹ or quantum bit. Just as a bit of information is stored as either 0 or 1, the two states of a Qbit are labeled $|0\rangle, |1\rangle$. Now consider the two Qbit states

$$|\psi\rangle = |0\rangle_1 |0\rangle_2 + |0\rangle_1 |1\rangle_2 + |1\rangle_1 |0\rangle_2 + |1\rangle_1 |1\rangle_2 \quad (1.48)$$

$$|\phi\rangle = |0\rangle_1 |0\rangle_2 + |1\rangle_1 |1\rangle_2 \quad (1.49)$$

ψ is not entangled, while state ϕ is. This can be seen by attempting to factorize the state into two subsystems.

$$|\psi\rangle = (|0\rangle_1 + |1\rangle_1) \otimes (|0\rangle_2 + |1\rangle_2) \quad (1.50)$$

$$|\phi\rangle = |0\rangle_1 |0\rangle_2 + |1\rangle_1 |1\rangle_2 \quad (1.51)$$

¹We adopt in this thesis the more harmonious spelling of David Mermin's [18].

ϕ cannot be factorized into two systems and hence is entangled. This is the well-known Bell state which is a bipartite entangled state. Another well-known entangled state we will see later in this thesis is the Greenberger-Horne-Zeilinger (GHZ) state [19].

The simplest continuous variable entangled system is the TMSS we saw in section 1.2. In analogy with Qbits, we call these a continuous-variable quantum modes or Qmodes. In the limit of infinite squeezing, the TMSS can be written as,

$$|TMSS\rangle = \int_{-\infty}^{\infty} |q\rangle_1 |q\rangle_2 dq \quad (1.52)$$

which is clearly not separable.

The quantum effects of superposition, entanglement and collapse of the wavefunction due to measurement can be applied together to get some drastic effects which have no classical analogue. Some of the proposed applications include quantum teleportation [20], quantum communication [21] and quantum computing [22]. Since most complex systems are made of a lot of interacting systems, understanding large scale entanglement allows us to study such complex behaviour [23]. At a fundamental level entangled systems are highly non-classical and as such are a very useful tool to study the quantum-classical transition and testing the validity of quantum mechanics itself. We will not elaborate on these concepts as they are beyond the scope of this thesis. We only note here that generation of entangled systems, especially large multipartite entangled systems is an extremely active area of research.

However, entanglement is extremely difficult to create and protect from environmental decoherence. Qbits systems are most commonly used in entanglement experiments since the theoretical framework of such systems is very well developed. Qdits, or d-level systems, can be considered an extension of Qbits. However, the theoretical protocols and their experimental proposals are not very well known and are far behind Qbits today. Continuous variable systems are Qdits where d goes to infinity.

Continuous-variable (CV) entanglement is a highly interesting and active field because it provides a new outlook on quantum information, offers rich perspectives such as massive scalability potential [24, 25, 26, 27], and can rely on the mature quantum optical experimental techniques of squeezed-state generation.

In particular, our group and collaborators have discovered [25, 28] and begun to demonstrate [26] massively scalable continuous-variable cluster entanglement in the quantum optical frequency comb, which opens up opportunities towards generating macroscopic entangled states. Such states are a big step towards measurement based quantum computing, a computing protocol which requires the generation of highly entangled cluster states as a resources and measurement operations to perform computations.

However there is a downside to using continuous variable systems. Real squeezed states are “approximate” entangled states, meaning that finitely squeezed states are an approximation to the maximally entangled states in the limit $r \rightarrow \infty$. Numerous works have found that this represents a fundamental “no-go” for all-Gaussian (in terms of the Wigner function) key quantum processes such as Bell inequality violation [17], entanglement distillation [29], and quantum error correction [30].

Considerable progress has been made recently towards tackling this problem. The solutions require either non-Gaussian measurements/gates on Gaussian states [31] or Gaussian gates on non-Gaussian states. Much research has focused on generation of non-Gaussian states [32, 33, 34, 35]. Generation of such states with high purity is very difficult and therefore the most feasible protocols use some form of distillation to get high quality states out of a large pool of low quality states [36].

Here we explore the former approach by first casting Gaussian states as effective spins, by use of the Schwinger representation [37]. Spin measurements will then coincide with photon-number-resolving measurements [3], which are known to be non-Gaussian measurements [38]. To the best of our knowledge, no clear protocol exists yet that uses simple photon number measurements to perform error correction of Gaussian states but it should, in principle, be possible.

Another goal is to ascertain whether the Schwinger representation would be a possible bridge from massively scalable Gaussian entanglement to massively scalable spin entanglement and, possibly, quantum simulation [23] of entangled spin lattices.

In section 1.5 we review the Schwinger representation, a. k. a. the quantum Poincaré sphere, or quantum Stokes parametrization, and illustrate its physical significance.

1.5 Schwinger representation

1.5.1 Mathematical formulation

In the Schwinger representation, two bosonic fields, say of annihilation operators a_1 and a_2 , are used to define an effective spin angular momentum \vec{J} , as follows

$$J_x = \frac{1}{2}(a_1^\dagger a_2 + a_1 a_2^\dagger) \quad (1.53)$$

$$J_y = \frac{1}{2i}(a_1^\dagger a_2 - a_1 a_2^\dagger) \quad (1.54)$$

$$J_z = \frac{1}{2}(a_1^\dagger a_1 - a_2^\dagger a_2), \quad (1.55)$$

which can easily be shown to obey the canonical commutation relations of an angular momentum. The spin ladder operators are

$$J_+ = J_x + iJ_y = a_1^\dagger a_2 \quad (1.56)$$

$$J_- = J_x - iJ_y = a_1 a_2^\dagger. \quad (1.57)$$

Finally the spin magnitude is

$$J^2 = J_x^2 + J_y^2 + J_z^2 = \frac{a_1^\dagger a_1 + a_2^\dagger a_2}{2} \left(\frac{a_1^\dagger a_1 + a_2^\dagger a_2}{2} + 1 \right) \quad (1.58)$$

and can be shown to be a scalar operator—consistent with the total energy of the two modes of the electromagnetic field. This leads us to the physical significance of this mathematical representation.

1.5.2 Physical meaning

As just remarked, J^2 represents the total energy of the two-mode field. This begets the adoption of the Fock basis $|n_1\rangle_1 |n_2\rangle_2$. Indeed, consider the action of the J^2 and J_z operators of a two-mode number state, using Eq. (1.55) and Eq. (1.58):

$$J^2 |n_1\rangle_1 |n_2\rangle_2 = \frac{n_1 + n_2}{2} \left(\frac{n_1 + n_2}{2} + 1 \right) |n_1\rangle_1 |n_2\rangle_2 \quad (1.59)$$

$$J_z |n_1\rangle_1 |n_2\rangle_2 = \frac{n_1 - n_2}{2} |n_1\rangle_1 |n_2\rangle_2. \quad (1.60)$$

This proves that the two-mode Fock states are the spin eigenstates $|jm\rangle$, with

$$j = \frac{n_1 + n_2}{2} \quad (1.61)$$

$$m = \frac{n_1 - n_2}{2}. \quad (1.62)$$

Hence the spin magnitude is the total photon number and the z -component of the spin is the photon number difference. The other two components of this effective spin are equally meaningful: Eqs. (1.53-1.54) clearly show that $J_{x,y}$ are interference terms of fields 1 and 2, respectively in phase and in quadrature.

Note that in this paper we will often use interchangeably for the total photon number and spin magnitude operators the SU(2) Casimir operator

$$J_0 = \frac{1}{2}(a_1^\dagger a_1 + a_2^\dagger a_2), \quad (1.63)$$

whose eigenvalue is j and which verifies $J^2 = J_0(J_0 + 1)$.

From these considerations, we easily deduce that measurements of the effective spin *along any direction* can then be made using variable beamsplitters and photon number resolving detection [39, 40, 41], as depicted in Fig. 1.7.

The detected fields are

$$b_1 = a_1 \cos \frac{\theta}{2} + a_2 e^{-i\phi} \sin \frac{\theta}{2} \quad (1.64)$$

$$b_2 = -a_1 \sin \frac{\theta}{2} + a_2 e^{-i\phi} \cos \frac{\theta}{2} \quad (1.65)$$

and the corresponding photon numbers are

$$\begin{aligned} b_1^\dagger b_1 &= N_1 \cos^2 \frac{\theta}{2} + N_2 \sin^2 \frac{\theta}{2} \\ &\quad + (a_1^\dagger a_2 e^{-i\phi} + a_1 a_2^\dagger e^{i\phi}) \cos \frac{\theta}{2} \sin \frac{\theta}{2} \end{aligned} \quad (1.66)$$

$$\begin{aligned} b_2^\dagger b_2 &= N_1 \sin^2 \frac{\theta}{2} + N_2 \cos^2 \frac{\theta}{2} \\ &\quad - (a_1^\dagger a_2 e^{-i\phi} + a_1 a_2^\dagger e^{i\phi}) \cos \frac{\theta}{2} \sin \frac{\theta}{2} \end{aligned} \quad (1.67)$$

so that

$$N_+ = b_1^\dagger b_1 + b_2^\dagger b_2 = \frac{1}{2}(N_1 + N_2) = J_0 \quad (1.68)$$

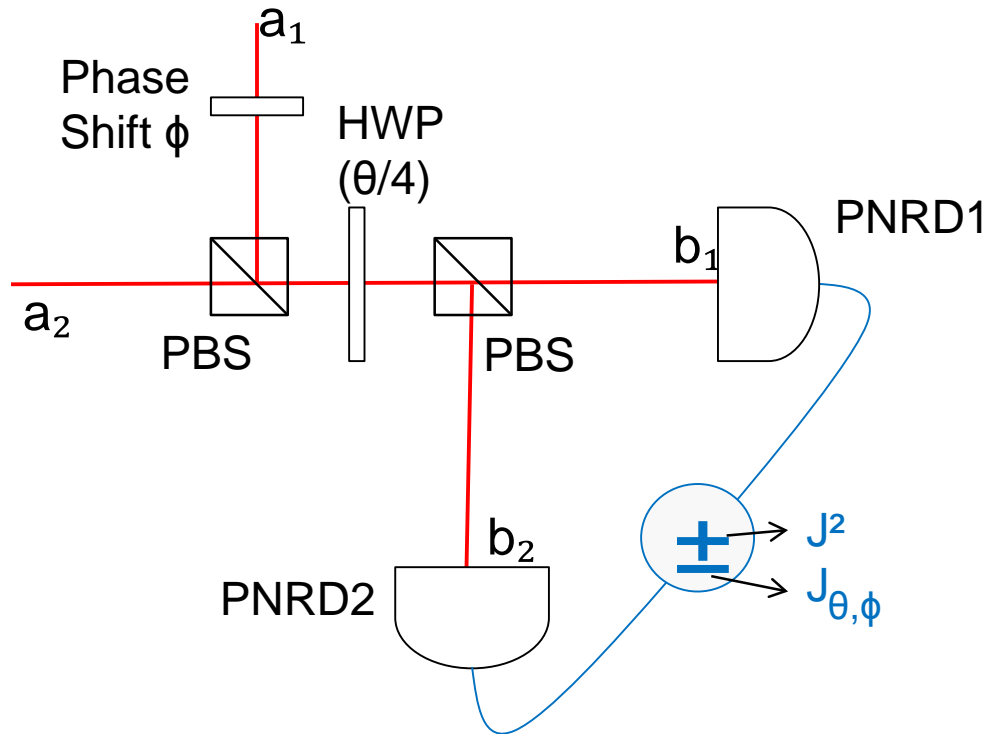


FIGURE 1.7: Arbitrary spin measurements (along direction (θ, ϕ)) can be performed with a phase shift ϕ , two polarizing beamsplitters (PBS), a halfwave plate (HWP) whose axes are at $\theta/4$ rad from the PBSs, and two photon-number-resolving detectors (PNRD1,2).

and

$$\begin{aligned}
 N_- &= b_1^\dagger b_1 - b_2^\dagger b_2 \\
 &= \frac{N_1 - N_2}{2} \cos \theta + \frac{a_1^\dagger a_2 e^{-i\phi} + a_1 a_2^\dagger e^{i\phi}}{2} \sin \theta \\
 &= J_z \cos \theta + (J_x \cos \phi + J_y \sin \phi) \sin \theta
 \end{aligned} \tag{1.69}$$

which prescribes how to set the half-wave plate θ and the phase shift ϕ to measure any component of the spin, together with its magnitude.

1.5.3 Previous work

The Schwinger representation has been widely used over the years, starting from the group theoretical modeling of interferometers by Yurke et al. in 1986 [39].

In 2002, Bowen et al. experimentally demonstrated single-spin squeezing from two-mode squeezed light [42].

In 2005, C. Gerry and J. Albert proposed using a beamsplitter with a Fock state input to violate Bell inequality using the Holstein-Primakoff spin representation [43]. In this representation, *single-mode* Fock states correspond to J_z eigenstates (as opposed to the two Qmodes in the Schwinger representation), the vacuum state $|0\rangle$ corresponds to the $|j, -j\rangle$ state, and $|n\rangle$ to $|j, -j + n\rangle$. The photon number anti-correlation between the two output Qmodes of a beamsplitter can then be written as an entangled spin system.

In 2011, Evans and Pfister used an original proposal by Drummond and Reid [44, 45] to show theoretically [41] that entangled spins could be used to violate the Mermin inequality [46]. This proposal uses the photon correlation in the two-mode squeezed state produced by parametric down-conversion (PDC) in an optical parametric amplifier (OPA) to create perfectly entangled spins of arbitrary magnitude. Indeed, two independent OPAs (labeled 1 and 2) emit a tensor product of TMSS (or EPR) states state [47],

$$|EPR^2\rangle = \sum_{n_1=0}^{\infty} \frac{\tanh^{n_1} r_1}{\cosh r_1} |n_1\rangle_{A1} |n_1\rangle_{B1} \otimes \sum_{n_2=0}^{\infty} \frac{\tanh^{n_2} r_2}{\cosh r_2} |n_2\rangle_{A2} |n_2\rangle_{B2}, \quad (1.70)$$

which can be rewritten in the Schwinger representation of spins A ($A1, A2$) and B ($B1, B2$), to a local optical phase shift left and assuming equal squeezing parameters $r_1 = r_2 = r$, as a superposition of *maximally entangled* states of zero total spin:

$$|EPR^2\rangle = \sum_{j=0}^{\infty} \frac{\tanh^{2j} r}{\cosh^2 r} \sum_{m=-j}^j (-1)^{j-m} |j, m\rangle_A |j, -m\rangle_B \quad (1.71)$$

where $j = (n_1 + n_2)/2$ as before. Note that the recasting of Eq. (1.70) as spin eigenstates features a rather remarkable property: the entanglement amount, initially quantified by the squeezing parameter in the EPR state of Eq. (1.70), becomes independent of r when the entangled part of the state is expressed as an $SU(2)$ eigenstate in Eq. (1.71), as can be clearly seen from its rightmost sum. In Eq. (1.71), the squeezing parameter r only conditions the probability of observing a particular spin magnitude j , *not the degree of entanglement*. For each and every value of j , the entanglement is maximal and independent of r ! This requires, however, projecting Eq. (1.71) into a single value of j , for example by a (preferably non-destructive) measurement of the total photon number.

The aforementioned bipartite entanglement property provides us with a strong motivation for investigating connections between Gaussian and spin entanglement

in the multipartite case.

1.6 Summary

In summary, we have laid out the foundation and motivation of this thesis. We have explained the motivation behind finding a way to use continuous variable entanglement to simulate entanglement in discrete systems.

In chapter 2, we detail our results towards finding such a system using multimode squeezed states that can be commonly generated in the lab. We have also explained the significance of Wigner function in characterizing quantum states.

In chapter 3, we detail the experiment we performed to demonstrate, for the first time, the direct detection of the Wigner function using photon number resolving detection.

We then conclude in chapter 4.

Chapter 2

From Light to Spins

2.1 Introduction

Here we detail the work done on the correspondence of multimode squeezed states and entangled Schwinger spin states. This work was published in Physics Review A in January 2014 [48].

In section 2.2 we look at the theoretical methods that allow us to find spin operators that are constants of motion of the squeezing Hamiltonian and can be used to define the states that they necessarily nullify. We then reexamine the example of bipartite spin entanglement using two EPR pairs. In section 2.3, we extend the results of our systematic derivations of the spin nullifiers to twin tri- and quadripartite CV states. In section 2.4, we make use of these results to derive the corresponding spin states in these cases, and examine their entanglement.

2.1.1 Stabilizers and Nullifiers

Studying quantum entanglement is easier through the use of the stabilizer formalism. A stabilizer of a state is an operator for which the state is an eigenstate with eigenvalue 1. A nullifier of a state is an operator for which the state is an eigenstate with eigenvalue 0. Therefore if St is a stabilizer and Nu a nullifier of

state $|\psi\rangle$ then,

$$\begin{aligned} St|\psi\rangle &= |\psi\rangle \\ Nu|\psi\rangle &= \mathbb{0}|\psi\rangle \end{aligned} \quad (2.1)$$

Naturally for every nullifier Nu , there is an operator e^{Nu} which is a stabilizer. Similarly for every stabilizer St , $\ln(St)$ is a nullifier.

To use the stabilizer formalism effectively, we have to use the Heisenberg picture. In the Heisenberg picture, instead of studying the evolution of the quantum states, we study the evolution of operators instead. We have already encountered the two mode squeezed state (TMSS) in equation 1.42

$$|TMSS\rangle_{12} = \frac{1}{\cosh^2 r} \sum_{n=0}^{\infty} \tanh^n r |n\rangle_1 |n\rangle_2$$

where $r = \kappa t$. We can write the squeezing evolution in the Schrödinger picture as

$$|TMSS\rangle_{out} = S_{12}(r) |0\rangle_{in}. \quad (2.2)$$

Alternatively in the Heisenberg picture, we look at the evolution of, say, an arbitrary operator M ,

$$\begin{aligned} \langle TMSS | M | TMSS \rangle_{out} &= \langle 0 | S_{12}^\dagger(r) M S_{12}(r) | 0 \rangle_{in} \\ &= \langle 0 | \tilde{M} | 0 \rangle_{in} \\ \implies \tilde{M}_{out} &= S_{12}^\dagger(r) M_{in} S_{12}(r) \end{aligned} \quad (2.3)$$

Therefore to evaluate the behaviour of the TMSS state, we can look at the evolution of the four two mode operators

$$\begin{aligned} S_{12}^\dagger(r) (P_1 + P_2) S_{12}(r) &= (P_1 + P_2) e^{-r} \\ S_{12}^\dagger(r) (Q_1 - Q_2) S_{12}(r) &= (Q_1 - Q_2) e^{-r} \\ S_{12}^\dagger(r) (P_1 - P_2) S_{12}(r) &= (P_1 - P_2) e^r \\ S_{12}^\dagger(r) (Q_1 + Q_2) S_{12}(r) &= (Q_1 + Q_2) e^r. \end{aligned} \quad (2.4)$$

Knowing the initial state and the above transformation uniquely identifies the evolution and the behaviour of the final state. Thus we can study the measurement results of the final state using the evolution of operators instead of evolution of the

states. The Heisenberg picture and the Schrödinger picture are completely equivalent, however the Heisenberg picture is often much easier to evaluate, especially in quantum optics.

Finally, in the limit of infinite squeezing $r \rightarrow \infty$, we have

$$\begin{aligned}(P_1 + P_2)_{out} &= e^{-r}(P_1 + P_2)_{in} \rightarrow 0 \\ (Q_1 - Q_2)_{out} &= e^{-r}(Q_1 - Q_2)_{in} \rightarrow 0.\end{aligned}\tag{2.5}$$

Therefore $(P_1 + P_2)_{in}$ and $(Q_1 - Q_2)_{in}$ are the nullifiers of the infinitely squeezed TMSS.

These squeezed operators are also the *variance-based entanglement witnesses* [49] of the state, i.e measuring this operator can tell us whether the state is entangled. This Heisenberg picture for defining CV entangled states is therefore a direct analog of the stabilizer formalism used to describe Qbit entanglement [50], and these squeezed (and antisqueezed) Qmodes provide a good starting point for understanding the relationship between CV- and spin entanglement.

In the analysis that follows we will be extensively using the Heisenberg picture. We will attempt to characterize and gain information about the states by studying their nullifiers. Deriving the full Schrödinger state of the state for multipartite is extremely involved as can be seen in more detail in Appendix A. Using nullifiers to study the state is a way to simplify this process. Another motivation to use nullifiers is to find cluster states [51, 52, 8] that can be used in quantum computing and quantum information where stabilizer formalism is most useful. We believe our method is instructive and demonstrates a promising direction of research into the correspondence between spins and squeezed states.

2.2 Squeezed states to Spins : Bipartite case

2.2.1 Nullifiers, stabilizers and constants of the motion

We write the complete basis of the quadrature operators for n quantum modes (“Qmodes”) as a vector $(Q, P)^T$ where $Q = (Q_1, \dots, Q_n)$, $P = (P_1, \dots, P_n)$. We use

multimode quadratic squeezing Hamiltonians of the form

$$\begin{aligned} H &= i\hbar\kappa \sum_{j,k} (a_j^\dagger G_{jk} a_k^\dagger - a_j G_{jk} a_k) \\ &= \frac{\hbar\kappa}{2} (Q^T G P + P^T G Q), \end{aligned} \quad (2.6)$$

where $\kappa > 0$ and G is the H(amiltonian)-graph adjacency matrix [53, 54], whose 0 and 1 entries inform on which Qmodes of the field are subjected to a two-mode squeezing interaction. We can find the evolution of the operator vector under the action of this Hamiltonian. From the physical point of view, diagonalizing G solves the Heisenberg-equation system [24]

$$\dot{Q} = \kappa G Q \quad (2.7)$$

$$\dot{P} = -\kappa G P. \quad (2.8)$$

From the mathematical, graph theoretical point of view, diagonalizing G yields the spectrum of the H-graph. Let G_D be the diagonal form of G and M the diagonalization matrix, then

$$G = M^{-1} G_D M \quad (2.9)$$

and the ‘‘eigenoperators’’ $Q' = M Q$ and $P' = M P$ of course verify

$$\dot{Q}' = \kappa G_D Q' \quad (2.10)$$

$$\dot{P}' = -\kappa G_D P' \quad (2.11)$$

which leads to the familiar result that the negative eigenvalues of G imply amplitude-quadrature squeezing

$$Q'_j(t) = Q'_j(0) e^{-|G_{Djj}|r}, \quad (2.12)$$

where $r = \kappa t$ is the squeezing parameter, and that the positive eigenvalues imply phase-quadrature squeezing

$$P'_k(t) = P'_k(0) e^{-G_{Dkk}r}. \quad (2.13)$$

(Keep in mind that these primed Qmodes are linear superposition of the initial Qmodes $(Q, P)^T$). In the limit $r \gg 1$, the system evolves into a simultaneous

eigenstate of all the squeezed Qmodes, with eigenvalue 0. These are then the nullifiers of the state.

Note finally that a zero eigenvalue of G_D implies that the corresponding Qmode is neither squeezed nor antisqueezed, i.e. it commutes with the squeezing Hamiltonian and is a *constant of the motion*. The measurement noise of quantum optical constants of the motion is therefore simply the vacuum (or “shot”) noise level when they evolve from an initial vacuum state.

2.2.2 Quantum evolution of Schwinger spin operators

We return now to the Schwinger representation. Since all Schwinger spin operators are quadratic in field operators, we can form the time-evolved spins out the CV operators above. Therefore using the Heisenberg representation we can find the time-evolved spin operators. Of particular interest to us, in analogy with the Qbit stabilizer formalism, are the spin nullifiers.

Rewriting Eqs. (1.53-1.55) in terms of quadratures, we get

$$J_x = Q_1 Q_2 + P_1 P_2 \quad (2.14)$$

$$J_y = Q_1 P_2 - P_1 Q_2 \quad (2.15)$$

$$J_z = \frac{1}{2}(Q_1^2 + P_1^2 - Q_2^2 - P_2^2), \quad (2.16)$$

Now if we consider the set of all linear Qmode operators as either squeezed or anti-squeezed operators, we see that we can make 2 types of spin nullifiers.

The first type is formed by a product of two squeezed Qmodes. These will be perfect nullifiers in the limit of infinite squeezing.

The second type, however, is *independent of the squeezing* and is formed products of one squeezed and one anti-squeezed operator. If the squeezing strengths are equal, which we’ll assume throughout the rest of the paper, then these field-quadratic operators are constants of the motion. Moreover, if these products are normally ordered, then they nullify the initial vacuum state by virtue of $a|0\rangle = 0$ and, being constants of the motion, they will also nullify the final state of the multimode squeezing Hamiltonian, whatever the value of the squeezing parameter.

It so happens that all Schwinger spin operators defined by Eqs. (1.53-1.55) and Eqs. (2.14-2.16) nullify the vacuum state. Therefore we can find all spin nullifiers of any Schwinger state by systematically taking all the normally ordered products of squeezed and anti-squeezed quadratures, given by Eqs. (2.14-2.16). Again, even though these nullifiers are constructed out of squeezed and anti-squeezed operators, they will be nullifiers independent of the squeezing parameter r .

Let's illustrate the above concepts in the familiar case of two 2-mode EPR pairs coupled to form two entangled spins (Fig. 2.1), as already evoked in the Schrödinger picture in Eqs. (1.70-1.71). The Hamiltonian for this system is

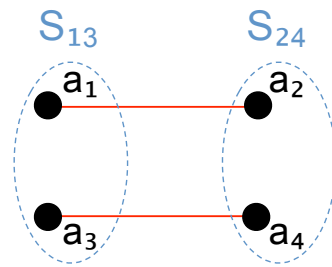


FIGURE 2.1: Two sets of 2-mode squeezed states, 1-2 and 3-4, can be viewed through the Schwinger representation as 2 effective spins (blue ellipses). The black dots represent Qmodes and the red edges denote the non-zero G_{jk} terms in the squeezing Hamiltonian.

$$H = i\hbar\kappa(a_1^\dagger a_2^\dagger + a_3^\dagger a_4^\dagger - a_1 a_2 - a_3 a_4) \quad (2.17)$$

$$= \hbar\kappa(Q_1 P_2 + P_1 Q_2 + Q_3 P_4 + P_3 Q_4) \quad (2.18)$$

$$= \frac{\hbar\kappa}{2}(Q^T G P + P^T G Q) \quad (2.19)$$

where

$$G = \begin{pmatrix} 0 & 1 & 0 & 0 \\ 1 & 0 & 0 & 0 \\ 0 & 0 & 0 & 1 \\ 0 & 0 & 1 & 0 \end{pmatrix}, \quad (2.20)$$

which is the adjacency matrix of the H-graph of the state in Fig. 2.1 (red edges). In later examples, we shall only use the H-graph to represent the Hamiltonian

instead of the G matrix. As we outlined above, we now diagonalize G yielding

$$G_D = \begin{pmatrix} 1 & 0 & 0 & 0 \\ 0 & -1 & 0 & 0 \\ 0 & 0 & 1 & 0 \\ 0 & 0 & 0 & -1 \end{pmatrix}, \quad M = \begin{pmatrix} 1 & 1 & 0 & 0 \\ -1 & 1 & 0 & 0 \\ 0 & 0 & 1 & 1 \\ 0 & 0 & -1 & 1 \end{pmatrix}. \quad (2.21)$$

Therefore, we have

$$Q'_{1,2}(t) = Q_1(t) \pm Q_2(t) = (Q_1 \pm Q_2)e^{\pm r} \quad (2.22)$$

$$P'_{1,2}(t) = P_1(t) \pm P_2(t) = (P_1 \pm P_2)e^{\mp r} \quad (2.23)$$

$$Q'_{3,4}(t) = Q_3(t) \pm Q_4(t) = (Q_3 \pm Q_4)e^{\pm r} \quad (2.24)$$

$$P'_{3,4}(t) = P_3(t) \pm P_4(t) = (P_3 \pm P_4)e^{\mp r}. \quad (2.25)$$

We get 8 linearly independent operators that can be constructed out of the combinations of the original 8 quadrature operators, 4 squeezed, and 4 anti-squeezed. Now using products of one squeezed and one anti-squeezed operator, we can get $4 \times 4 = 16$ linearly independent quadratic (spin) constants of the motion.

Out of these, only 6 can be defined according to Eqs. (2.14-2.16). As pointed out above, all Schwinger operators are nullifiers of the initial vacuum state, therefore any that are also constants of motion of the squeezing transformation are squeezing-independent spin nullifiers for the final state as well. (We will be using a vacuum initial state for the rest of the thesis as well.) These are

$$(P_1 + P_2)(P_1 - P_2) + (Q_1 + Q_2)(Q_1 - Q_2) + (P_3 + P_4)(P_3 - P_4) + (Q_3 + Q_4)(Q_3 - Q_4) = 4(J_{013} - J_{024}) = 0 \quad (2.26)$$

$$(P_1 + P_2)(P_1 - P_2) + (Q_1 + Q_2)(Q_1 - Q_2) - (P_3 + P_4)(P_3 - P_4) - (Q_3 + Q_4)(Q_3 - Q_4) = 4(J_{z13} - J_{z24}) = 0 \quad (2.27)$$

$$(P_1 + P_2)(P_3 - P_4) + (P_1 - P_2)(P_3 + P_4) + (Q_1 + Q_2)(Q_3 - Q_4) + (Q_1 - Q_2)(Q_3 + Q_4) = 4(J_{x13} - J_{x24}) = 0 \quad (2.28)$$

$$(P_1 + P_2)(Q_3 + Q_4) + (P_1 - P_2)(Q_3 - Q_4) - (Q_1 + Q_2)(P_3 + P_4) - (Q_1 - Q_2)(P_3 - P_4) = 4(J_{y13} + J_{y24}) = 0 \quad (2.29)$$

which correspond to the spin definition of Fig. 2.1.

It can be verified that their eigenstate does indeed have the form of Eq. (1.71)—with the proper Qmode-labeling conventions, and to local optical phase shifts left [41]. Indeed, the 4 nullifiers can then be written as $J_k = J_{k13} + J_{k42} \quad \forall k \in \{x, y, z\}$ and $J_{013} - J_{042}$. Therefore, the final state is an eigenstate of total spin along x,y and z with eigenvalue zero, which corresponds to the total spin-zero state of Eq. (1.71).

The last two spin nullifiers are

$$\begin{aligned} & (P_1 + P_2)(P_3 - P_4) - (P_1 - P_2)(P_3 + P_4) + (Q_1 + Q_2)(Q_3 - Q_4) \\ & - (Q_1 - Q_2)(Q_3 + Q_4) = 4(J_{x23} - J_{x14}) = 0 \end{aligned} \quad (2.30)$$

$$\begin{aligned} & (P_1 + P_2)(Q_3 + Q_4) - (P_1 - P_2)(Q_3 - Q_4) - (Q_1 + Q_2)(P_3 + P_4) \\ & + (Q_1 - Q_2)(P_3 - P_4) = 4(J_{y23} + J_{y14}) = 0 \end{aligned} \quad (2.31)$$

However, these operators pertain to spin pairings that are different from Fig. 2.1, gathering Qmodes 1-4 and 2-3 instead of 1-3 and 2-4. We can easily check that if we did use this spin definition, we can again define the final state as a total spin-zero state. This is an expected result since an EPR pair is symmetric about the exchange of the two modes.

The remaining 10 constants of motion cannot be written as Schwinger spin operators of the form Eqs. (2.14-2.16). We list them here,

$$\begin{aligned} & a_1^2 - a_2^2 + a_1^{\dagger 2} - a_2^{\dagger 2}, & a_3^2 - a_4^2 + a_3^{\dagger 2} - a_4^{\dagger 2}, \\ & a_1^2 + a_2^2 - a_1^{\dagger 2} - a_2^{\dagger 2}, & a_3^2 + a_4^2 - a_3^{\dagger 2} - a_4^{\dagger 2}, \\ & a_3 a_2 - a_4^{\dagger} a_1^{\dagger}, & a_4 a_1 - a_2^{\dagger} a_3^{\dagger}, & a_4 a_2 - a_3^{\dagger} a_1^{\dagger}, \\ & a_3 a_1 - a_4^{\dagger} a_2^{\dagger}, & a_1 a_2 - a_2^{\dagger} a_1^{\dagger}, & a_3 a_4 - a_4^{\dagger} a_4^{\dagger}. \end{aligned}$$

These are not normally ordered, i.e. they contain photon-number non-conserving operators such as $aa + a^{\dagger}a^{\dagger}$. Therefore these operators, even though constants of the motion, are not nullifiers since they do not nullify the initial vacuum state.

Similarly we can also check if any of the squeezed quadratic operators such as $(P_1 + P_2)(Q_1 - Q_2)$ form spin operators that would not be constants of motion but would be nullifiers in the limit $r \gg 1$. However, we found that all the remaining possible spin operators are linear combinations of squeezed and anti-squeezed operators and are therefore not nullifiers.

The next step is to apply this approach to more complicated CV multipartite entangled states. At this point, we must make clear that, even though we do conduct a systematic search for state nullifiers, we have left out (for now) the far-reaching considerations of Qdit-stabilizer groups and cluster-state definition and characterization, narrowing our scope to simply determining whether (and how) multipartite-entangled CV states can be mapped onto multipartite-entangled spin states.

We will show that this method of characterizing the spin state generated by a given quadratic Hamiltonian is analytically easy, especially since methods for finding CV squeezed and anti-squeezed operators are well known. Moreover, the converse process of finding a Hamiltonian to generate any desired spin state is non-trivial, thus our approach may be quite beneficial if interesting spin states are found. Here we shall only focus on the study of states with up to 4 spins, out of multipartite CV states which have been realized experimentally.

2.3 Multipartite spin nullifiers

We now turn to the casting of CV multipartite entangled states into spin states and investigating the entanglement of the latter. We naturally start with the simplest non-trivial examples of tripartite and quadripartite [53, 26] CV graph states.

2.3.1 Three-spin systems

By analogy with Fig. 2.1, we choose to examine the twin three-Qmode arrangements illustrated in Figs. 2.2 and 2.3: we can have a chain with 2 interactions, say 1-2 and 2-3, or we can have a triangle with 3 interactions, 1-2, 2-3 and 3-1. The CV nullifiers for the two systems will be different and hence the spin operators and constants of motion are expected to be different as well.

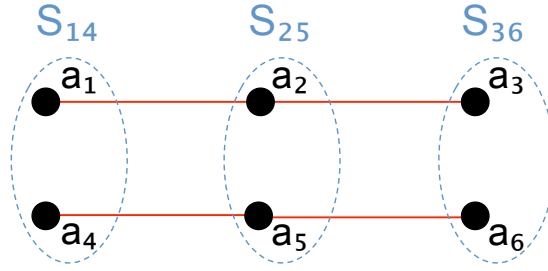


FIGURE 2.2: Two sets of 3 Qmodes, 1-3 and 4-6, cast as 3 effective spins (blue ellipses).

2.3.1.1 Three-Qmode chain

We can easily find the spin constants of motion of the state of Fig. 2.2 using the methods developed above. The CV nullifiers are readily obtained

$$Q'_2(r) = (Q_1 - \sqrt{2}Q_2 + Q_3) e^{-\sqrt{2}r} \quad (2.32)$$

$$P'_1(r) = (P_1 + \sqrt{2}P_2 + P_3) e^{-\sqrt{2}r} \quad (2.33)$$

$$Q'_5(r) = (Q_4 - \sqrt{2}Q_5 + Q_6) e^{-\sqrt{2}r} \quad (2.34)$$

$$P'_4(r) = (P_4 + \sqrt{2}P_5 + P_6) e^{-\sqrt{2}r} \quad (2.35)$$

from which we find that there are 10 spin constants of motion

$$J_{014} + J_{036} - J_{025} + \mathbb{1} = 0 \quad (2.36)$$

$$J_{z14} + J_{z36} - J_{z25} = 0 \quad (2.37)$$

$$J_{x14} + J_{x36} - J_{x25} = 0 \quad (2.38)$$

$$J_{y14} + J_{y36} + J_{y25} = 0 \quad (2.39)$$

$$J_{x16} + J_{x34} - J_{x25} = 0 \quad (2.40)$$

$$J_{y16} + J_{y34} + J_{y25} = 0 \quad (2.41)$$

$$J_{x15} + J_{x35} - J_{x24} - J_{x26} = 0 \quad (2.42)$$

$$J_{y15} + J_{y35} + J_{y24} + J_{y26} = 0 \quad (2.43)$$

$$J_{014} + J_{036} - J_{x13} - J_{x46} + \mathbb{1} = 0 \quad (2.44)$$

$$J_{z14} + J_{z36} - J_{x13} + J_{x46} = 0 \quad (2.45)$$

The existence of operators which mix different spin definitions is something we see again in this case. While a non-trivial property, it is not consistent with the spin definitions adopted in Fig. 2.2. It is not entirely clear how these nullifiers can be

used beyond the information they give us about the exchange symmetries of the modes, for example in this system, modes 4 and 6, and mode 1 and 3 are symmetric and can be interchanged. In our paper and in this thesis, we will only consider operators that conform to one specific definition of spins, in this case 1-4, 2-5, 3-6, as in Fig. 2.2. The 4 spin nullifiers in this case are given in Eqs. (2.36-2.39).

Another interesting point is that the number of nullifiers obeying a spin definition criteria has not increased, even though we added one spin.

2.3.1.2 Thee-Qmode ring: CVGHZ state

It is well known that a complete H-graph will yield a GHZ state [24]. We are therefore naturally curious about the spin state of Fig. 2.3. The CVGHZ nullifiers

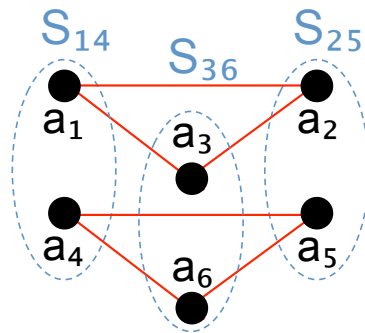


FIGURE 2.3: Two sets of 3 Qmodes, 1-3 and 4-6, as 3 effective spins (blue ellipses).

are well known [55, 24]:

$$P'_1(r) = (P_1 + P_2 + P_3) e^{-2r} \quad (2.46)$$

$$Q'_2(r) = (Q_1 - Q_2) e^{-r} \quad (2.47)$$

$$Q'_3(r) = (Q_2 - Q_3) e^{-r} \quad (2.48)$$

$$P'_4(r) = (P_4 + P_5 + P_6) e^{-2r} \quad (2.49)$$

$$Q'_5(r) = (Q_4 - Q_5) e^{-r} \quad (2.50)$$

$$Q'_6(r) = (Q_5 - Q_6) e^{-r} \quad (2.51)$$

and from these we find the spin constants of motion of this system to be

$$J_{y12} + J_{y23} + J_{y31} = 0 \quad (2.52)$$

$$J_{y45} + J_{y56} + J_{y64} = 0 \quad (2.53)$$

$$J_{y16} - J_{y14} + J_{y24} - J_{y26} = 0 \quad (2.54)$$

$$J_{y15} - J_{y14} + J_{y34} - J_{y35} = 0 \quad (2.55)$$

$$J_{y15} - J_{y14} + J_{y24} - J_{y25} = 0 \quad (2.56)$$

$$J_{y16} - J_{y14} + J_{y34} - J_{y36} = 0 \quad (2.57)$$

$$\begin{aligned} &J_{y14} + J_{y15} + J_{y16} + J_{y24} \\ &+ J_{y25} + J_{y26} + J_{y34} + J_{y35} + J_{y36} = 0 \end{aligned} \quad (2.58)$$

Interestingly enough, *none* of the above nullifiers is consistent with the non-overlapping spin pairings in the spin definitions of Fig. 2.3! Therefore it becomes difficult to conceive of merely characterizing a three-spin system, let alone quantifying any spin entanglement, from these operators. (Recall that each spin correspond to a well-defined Qmode pair on which interference and photon-number measurements are made.) This particular arrangement of Qmodes in Fig. 2.3 thus seems to thoroughly defeat our approach, an interesting conclusion that stems solely from the Heisenberg viewpoint. Such is not the case, however, for the spin graph of Fig. 2.2. Before we investigate the spin state associated with it, we derive the spin nullifiers for some 4-spin cases.

2.3.2 Four-spin systems

2.3.2.1 Four-Qmode chain and ring CV states

We will not treat the 4-Qmode chain and the ring separately as these two are specific cases of a more general CV cluster state [51], as we first recall. (Note that it is the *complete* H-graph, not the *ring* H-graph, that gives a CVGHZ state. As is well known, these are the same for up to tripartite entanglement but become different for quadripartite and larger systems.) All the cases are depicted in Fig. 2.7.

The Hamiltonian for the 4-Qmode chain [Fig. 2.7(a)] is

$$H^{(0)} = i\hbar\kappa(a_1^\dagger a_2^\dagger + a_2^\dagger a_3^\dagger + a_3^\dagger a_4^\dagger) + H.c. \quad (2.59)$$

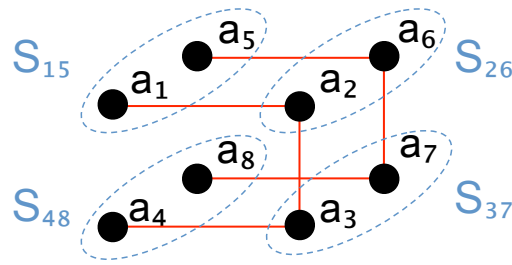
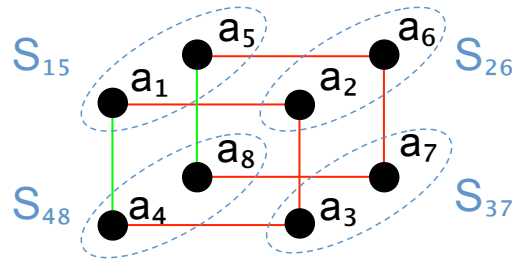
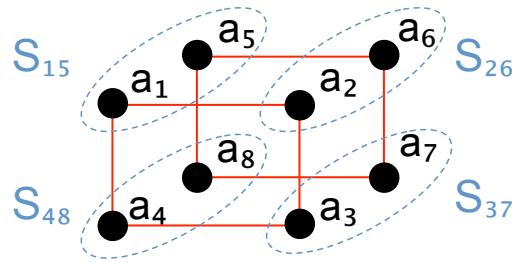

 FIGURE 2.4: Chain H-graph, square cluster state, $H^{(0)}$

 FIGURE 2.5: Square H-graph, square cluster state, $H^{(1)}$

 FIGURE 2.6: Ring H-graph, $H^{(2)}$

FIGURE 2.7: The 4-mode Hamiltonians studied in this paper. The green edges denote a change sign in the corresponding two-mode squeezing term with respect to the red edges.

and was implemented in our laboratory [26] and shown to generate a quadripartite entangled CV cluster state, of nullifiers

$$Q'_3(r) = [(Q_1 - Q_4) + \Phi(Q_3 - Q_2)]e^{-r\Phi} \quad (2.60)$$

$$P'_1(r) = [(P_1 + P_4) + \Phi(P_3 + P_2)]e^{-r\Phi} \quad (2.61)$$

$$Q'_2(r) = [\Phi(Q_1 + Q_4) - (Q_3 + Q_2)]e^{-\frac{r}{\Phi}} \quad (2.62)$$

$$P'_4(r) = [\Phi(P_1 - P_4) - (P_3 - P_2)]e^{-\frac{r}{\Phi}} \quad (2.63)$$

where $\Phi = (\sqrt{5} + 1)/2$ is the golden ratio. These nullifiers can be shown to be

equivalent, in the limit $r \gg 1$ and to local optical phase shifts left, to the nullifiers of a ring (or “square”) Qmode cluster-state [26]. Note also that a more general description of CV graph states in the presence of finite squeezing has since been expounded [56, 57].

However, a Qmode square cluster state can also be generated by the Hamiltonian of Fig. 2.7(b) [53, 26]

$$H^{(1)} = i\hbar\kappa(a_1^\dagger a_2^\dagger + a_2^\dagger a_3^\dagger + a_3^\dagger a_4^\dagger - a_4^\dagger a_1^\dagger) + H.c. \quad (2.64)$$

The solutions of the Heisenberg equations of motion for Eq. (2.64) are

$$Q'_2(r) = (Q_1 + Q_2 - \sqrt{2} Q_4) e^{-r\sqrt{2}} \quad (2.65)$$

$$Q'_3(r) = (Q_1 - Q_2 + \sqrt{2} Q_3) e^{-r\sqrt{2}} \quad (2.66)$$

$$P'_1(r) = (P_1 + P_2 + \sqrt{2} P_4) e^{-r\sqrt{2}} \quad (2.67)$$

$$P'_4(r) = (P_1 - P_2 - \sqrt{2} P_3) e^{-r\sqrt{2}}. \quad (2.68)$$

Like Eqs. (2.60-2.63), these squeezed operators exactly coincide with the same nullifiers of a square cluster state, to local phase shifts left and in the limit $r \gg 1$.

Finally, we consider the Hamiltonian of Fig. 2.7(c), which can be viewed as a two-mode squeezed state, each Qmode of which (1,2) being mixed with a vacuum mode (3,4) on a balanced beamsplitter. The resulting 4-Qmode Hamiltonian is

$$\begin{aligned} H^{(2)} &= U_{13}^\dagger U_{24}^\dagger (i\hbar\kappa a_1^\dagger a_2^\dagger + H.c.) U_{13} U_{24} \\ &= \frac{i\hbar\kappa}{2} (a_1^\dagger + a_3^\dagger)(a_2^\dagger + a_4^\dagger) + H.c. \\ &= \frac{i\hbar\kappa}{2} (a_1^\dagger a_2^\dagger + a_3^\dagger a_4^\dagger + a_3^\dagger a_2^\dagger + a_1^\dagger a_4^\dagger) + H.c. \end{aligned} \quad (2.69)$$

where $U_{kl} = \exp[-\frac{\pi}{4}(a_k^\dagger a_l + a_l^\dagger a_k)]$.

It is important to note that $H^{(0)}$, $H^{(1)}$ and $H^{(2)}$ only differ in the term of the 1-4 interaction, which is respectively zero [Eq. (2.59)], of opposite sign [Eq. (2.64)], and of the same sign [Eq. (2.69)] as the other terms, as is also clear from Fig. 2.7.

In $H^{(0)}$, the 1-4 interaction is absent. In $H^{(1)}$, the relative sign difference corresponds to having 3 non-linear parametric downconverting interactions and 1 upconverting interaction, while in $H^{(2)}$ all 4 interactions are downconverting ones.

We will see soon that the photon number correlations are similar in the 3 Hamiltonians, however, the field correlations are different. As a result, while $H^{(0)}$ and $H^{(1)}$ make quadripartite CV cluster states, $H^{(2)}$ does not.

To describe all cases of Fig. 2.7 in the most general fashion, we therefore consider the following 8-mode Hamiltonian

$$H_{1-4} = i\hbar\kappa(G_{12}a_1^\dagger a_2^\dagger + G_{23}a_2^\dagger a_3^\dagger + G_{34}a_3^\dagger a_4^\dagger + G_{14}a_4^\dagger a_1^\dagger) + H.c. \quad (2.70)$$

$$H_{5-8} = i\hbar\kappa(G_{56}a_5^\dagger a_6^\dagger + G_{67}a_6^\dagger a_7^\dagger + G_{78}a_7^\dagger a_8^\dagger + G_{58}a_8^\dagger a_5^\dagger) + H.c. \quad (2.71)$$

$$H_{1-8} = H_{1-4} + H_{5-8}, \quad (2.72)$$

where $G_{ij} = \pm 1, 0$. We also decide, still in accord with Fig. 2.7, on the specific choice of Qmode pairings such that the spins are made up of Qmode pairs (15), (26), (37), and (48), only. We now derive the spin nullifiers that pertain to this definition of spins.

Two constants of the motion can be deduced intuitively from inspection of the two-photon emission processes in Eq. (2.70), where we can easily see that when this Hamiltonian acts on the vacuum, pairs of photons are emitted or annihilated that involve the Qmode pairs (12), (23), (34), and (41). From this we predict that

$$(N_1 + N_3) - (N_2 + N_4) = 0, \quad (2.73)$$

which can be proven easily:

$$\begin{aligned} [N_1 + N_3 - N_2 - N_4, H] &= [N_1 + N_3, H] - [N_2 + N_4, H] \\ &= H - H = 0, \end{aligned} \quad (2.74)$$

hence the operator $N_1 + N_3 - N_2 - N_4$ is a constant of the motion. Since this operator is a nullifier of initial (vacuum) state, it also nullifies the final state. The same holds for Eq. (2.71), with

$$(N_5 + N_7) - (N_6 + N_8) = 0. \quad (2.75)$$

Considering now the total Hamiltonian of Eq. (2.72), we deduce the following two nullifiers

$$\begin{aligned} & (N_1 + N_3 - N_2 - N_4) + (N_5 + N_7 - N_6 - N_8) \\ & = (J_{015} + J_{037}) - (J_{026} + J_{048}) = 0 \end{aligned} \quad (2.76)$$

$$\begin{aligned} & (N_1 + N_3 - N_2 - N_4) - (N_5 + N_7 - N_6 - N_8) \\ & = (J_{z15} + J_{z37}) - (J_{z26} + J_{z48}) = 0, \end{aligned} \quad (2.77)$$

which can also be derived from products of squeezed and antisqueezed linear operators.

It is reasonable to take all the H-graphs paired to make spin graphs in Fig. 2.7 identical, as is implicit in Figs. 2.1 and 2.7. From this we can find the following two nullifiers

$$(J_{x15} + J_{x37}) - (J_{x26} + J_{x48}) = 0 \quad (2.78)$$

$$(J_{y15} + J_{y37}) + (J_{y26} + J_{y48}) = 0. \quad (2.79)$$

This again can be easily verified, e.g., for the former,

$$\begin{aligned} & [J_{x15} + J_{x37} - J_{x26} - J_{x48}, H_{1-8}] \\ & = i\hbar\kappa[G_{12}a_5^\dagger a_2^\dagger + G_{34}a_7^\dagger a_4^\dagger + G_{23}a_7^\dagger a_2^\dagger + G_{14}a_5^\dagger a_4^\dagger \\ & \quad - G_{12}a_1^\dagger a_6^\dagger - G_{34}a_3^\dagger a_8^\dagger - G_{23}a_3^\dagger a_6^\dagger - G_{14}a_1^\dagger a_8^\dagger \\ & \quad - (G_{56}a_5^\dagger a_2^\dagger + G_{78}a_7^\dagger a_4^\dagger + G_{67}a_7^\dagger a_2^\dagger + G_{58}a_5^\dagger a_4^\dagger \\ & \quad - G_{56}a_1^\dagger a_6^\dagger - G_{78}a_3^\dagger a_8^\dagger - G_{67}a_3^\dagger a_6^\dagger - G_{58}a_1^\dagger a_8^\dagger)] \end{aligned} \quad (2.80)$$

which is zero iff $G_{12} = G_{56}$, $G_{23} = G_{67}$, $G_{34} = G_{78}$, and $G_{14} = G_{58}$, i.e., iff the 1-4 H-graph is identical to the 5-8 H-graph. The commutation of $J_{y15} + J_{y37} + J_{y26} + J_{y48}$ with H follows similarly.

Note that no constraint has yet been placed on the relative interactions strengths within a square, and these 4 nullifiers are therefore valid for all three Hamiltonians we discussed earlier. These nullifiers are also similar to the highly symmetric ones we had for the two spins case. Finally, we have also shown, using the exhaustive approach outlined in section 2.2 and section 2.3 (finding squeezed and antisqueezed operators and combining them to form operators that are invariant

under the Hamiltonian), that there are no other nullifiers to be found pertaining to these particular spin definitions, even though one can find 6 other SU(2) nullifiers pertaining to different spin pairings.

We can make the 4 nullifiers more symmetric by inessential adjustments, namely by exchanging the Qmodes in spins 26 and 48, which become 62 and 84 respectively, and by optically phase-shifting Qmodes 6 and 8 by π , which yields the following 4 nullifiers

$$J_0 = J_{015} + J_{037} - J_{062} - J_{084} = 0, \quad (2.81)$$

$$J_z = J_{z15} + J_{z37} + J_{z62} + J_{z84} = 0, \quad (2.82)$$

$$J_x = J_{x15} + J_{x37} + J_{x62} + J_{x84} = 0, \quad (2.83)$$

$$J_y = J_{y15} + J_{y37} + J_{y62} + J_{y84} = 0. \quad (2.84)$$

It is remarkable, and worth repeating here, that these nullifiers hold irrespective of the relative signs of the interaction terms in the Hamiltonian of Eq. (2.72).

Moreover, Equations (2.82-2.84) define the components of a “total spin” $\vec{J} = \vec{J}_{15} + \vec{J}_{37} + \vec{J}_{62} + \vec{J}_{84}$. Indeed, we can show that

$$(i) [J_0, J_i] = 0, \quad \forall i = x, y, z.$$

$$(ii) [J_k, J_l] = \epsilon_{klm} i J_m, \quad \forall k, l, m = x, y, z.$$

A few important points: because of (i), we can measure J_0 simultaneously to any component, as was already the case in Fig. 1.7. This means that not only are J_z, J_x, J_y nullifiers of the state, they must also be nullifiers of any state that is post-selected by a measurement of J_0 . Also, it is clear from Eqs. (2.82-2.84) that for each value of J_0 , the state we seek must have zero total spin: $|0, 0\rangle$. These are useful findings as we embark on finding the corresponding quantum spin state in the next section. We first take a brief look at the four mode GHZ state.

2.3.2.2 Four-Qmode GHZ state

Before turning to the explicit expression of the spin states, we consider the same GHZ construction as in section 2.3.1.2, illustrated in Fig. 2.8.

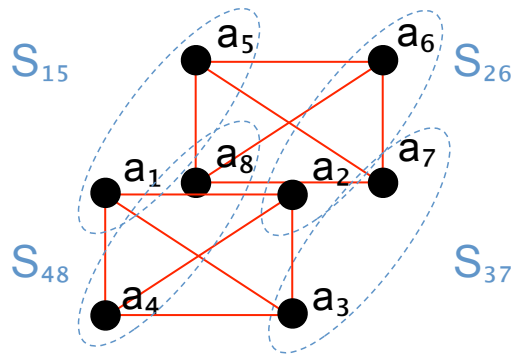


FIGURE 2.8: Two 4-Qmode GHZ states, 1-4 and 5-8, paired as 4 Schwinger spins (blue ellipses).

As mentioned earlier, the Hamiltonian is that of a complete H-graph

$$H^{(3)} = i\hbar\kappa \left(\sum_{i < j \in [1,4]} a_i^\dagger a_j^\dagger + \sum_{i < j \in [5,8]} a_i^\dagger a_j^\dagger \right) + H.c. \quad (2.85)$$

Following again the same procedure to find the nullifiers, we found, exactly as in the 3-spin case in section 2.3.1.2, that there are no nullifiers that pertain the specific 4-spin definitions of Fig. 2.8. All the spin constants of motion that we derived mix pairings of Qmodes and therefore we cannot choose any definition of spins for which any of these operators will be applicable.

2.4 Multipartite spin entanglement

We now turn to using the nullifiers that we have derived in the previous sections to derive the analytic expression of the corresponding spin state, in order to attempt to identify if these spin states are multipartite entangled and, if so, to attempt to determine the nature of the entanglement.

2.4.1 Derivation of the spin state for Qbits

Writing the full state for all photon numbers, i.e., for all values of the spin magnitudes, is an arduous and tedious task that we will not present here (see Appendix A). Here we will make use instead of the post-selection property mentioned at

the end of section 2.3.2.1: indeed, we have shown that measuring the total photon number of each Qmode, i.e. the Casimir operator, or magnitude, of each spin (j_{15} , j_{62} , j_{37} , j_{84}) is doable simultaneously with any other measurement of the spin components. We therefore select the simplest interesting case of 4 Qbits, i.e., $j_{15} = j_{37} = j_{62} = j_{84} = 1/2$, which satisfies Eq. (2.81). Using this post-selected substate we will prove simply that a multipartite entangled spin state is created by the Hamiltonian of Eq. (2.69).

We can generate this state in the lab by decreasing the interaction strength such that we can approximate the state as the truncated expansion of the propagator on the vacuum. We do this for the Hamiltonian of Eq. (2.72) to get

$$\begin{aligned}
|\psi_f\rangle &= e^{-\frac{i}{\hbar}Ht} |\psi_i\rangle \\
&= \exp[r\{(G_{12}a_1^\dagger a_2^\dagger + G_{23}a_2^\dagger a_3^\dagger + G_{34}a_3^\dagger a_4^\dagger + G_{14}a_4^\dagger a_1^\dagger) - H.c. \\
&\quad + (G_{12}a_5^\dagger a_6^\dagger + G_{23}a_6^\dagger a_7^\dagger + G_{34}a_7^\dagger a_8^\dagger + G_{14}a_8^\dagger a_5^\dagger) - H.c.\}] |0\rangle \\
&= 1 + r(\dots) \\
&\quad + r^2(G_{12}G_{34}(a_1^\dagger a_2^\dagger a_3^\dagger a_4^\dagger + a_1^\dagger a_2^\dagger a_7^\dagger a_8^\dagger + a_5^\dagger a_6^\dagger a_3^\dagger a_4^\dagger + a_5^\dagger a_6^\dagger a_7^\dagger a_8^\dagger) \\
&\quad + G_{23}G_{14}(a_1^\dagger a_2^\dagger a_3^\dagger a_4^\dagger + a_1^\dagger a_6^\dagger a_7^\dagger a_4^\dagger + a_5^\dagger a_2^\dagger a_3^\dagger a_8^\dagger + a_5^\dagger a_6^\dagger a_7^\dagger a_8^\dagger) \\
&\quad + \mathcal{O}(r^3)] |0\rangle \tag{2.86}
\end{aligned}$$

We can then post-select, by measuring all 4 individual Casimir operators (Fig. 1.7) and keeping only the terms that create 4 Qbits, i.e., create *exactly one photon, either in 1 or in 5*, and the same for (26), (37), and (48). This yields

$$\begin{aligned}
|\psi_f\rangle &= [G_{12}G_{34}(a_1^\dagger a_2^\dagger a_3^\dagger a_4^\dagger + a_1^\dagger a_2^\dagger a_7^\dagger a_8^\dagger + a_5^\dagger a_6^\dagger a_3^\dagger a_4^\dagger + a_5^\dagger a_6^\dagger a_7^\dagger a_8^\dagger) \\
&\quad + G_{23}G_{14}(a_1^\dagger a_2^\dagger a_3^\dagger a_4^\dagger + a_1^\dagger a_6^\dagger a_7^\dagger a_4^\dagger + a_5^\dagger a_2^\dagger a_3^\dagger a_8^\dagger + a_5^\dagger a_6^\dagger a_7^\dagger a_8^\dagger)] |0\rangle \\
&= a \left(|\uparrow\rangle_{15} |\uparrow\rangle_{26} |\downarrow\rangle_{37} |\downarrow\rangle_{48} + |\downarrow\rangle_{15} |\downarrow\rangle_{26} |\uparrow\rangle_{37} |\uparrow\rangle_{48} \right) \\
&\quad + b \left(|\uparrow\rangle_{15} |\downarrow\rangle_{26} |\downarrow\rangle_{37} |\uparrow\rangle_{48} + |\downarrow\rangle_{15} |\uparrow\rangle_{26} |\uparrow\rangle_{37} |\downarrow\rangle_{48} \right) \\
&\quad + (a + b) \left(|\uparrow\rangle_{15} |\uparrow\rangle_{26} |\uparrow\rangle_{37} |\uparrow\rangle_{48} + |\downarrow\rangle_{15} |\downarrow\rangle_{26} |\downarrow\rangle_{37} |\downarrow\rangle_{48} \right) \tag{2.87}
\end{aligned}$$

where $G_{12}G_{34} = a$ and $G_{23}G_{14} = b$. We now make the same single-mode unitary operations as mentioned in the last section, considering spins 62 and 84 instead of 26 and 48 and phase-shifting Qmodes 6 and 8 by π , and get

$$\begin{aligned}
|\psi_f\rangle = & a \left(|\uparrow\rangle_{15} |\downarrow\rangle_{26} |\downarrow\rangle_{37} |\uparrow\rangle_{48} + |\downarrow\rangle_{15} |\uparrow\rangle_{26} |\uparrow\rangle_{37} |\downarrow\rangle_{48} \right) \\
& + b \left(|\uparrow\rangle_{15} |\uparrow\rangle_{26} |\downarrow\rangle_{37} |\downarrow\rangle_{48} + |\downarrow\rangle_{15} |\downarrow\rangle_{26} |\uparrow\rangle_{37} |\uparrow\rangle_{48} \right) \\
& - (a + b) \left(|\uparrow\rangle_{15} |\downarrow\rangle_{26} |\uparrow\rangle_{37} |\downarrow\rangle_{48} + |\downarrow\rangle_{15} |\uparrow\rangle_{26} |\downarrow\rangle_{37} |\uparrow\rangle_{48} \right). \quad (2.88)
\end{aligned}$$

We can check that this state satisfies all 4 nullifiers Eqs. (2.81-2.84) and is therefore a total spin zero state. We can of course apply an overall normalization constraint satisfying $2|a|^2 + 2|b|^2 + 2|a + b|^2 = 1$. For different instances of G , we will get completely different states which may or may not be entangled spins.

2.4.2 Entanglement characterization

There is no commonly agreed metric of multipartite entanglement even for Qbits although many candidates exist. Average von Neumann entropy, partial positive trace method, Schmidt decomposition are a few of the possible entanglement metrics. There have been several attempts to compare the various entanglement metrics and to characterize and find maximally entangled states [58]. We will not attempt to compare the degree of entanglement of the states considered and will simply observe whether they are factorisable or not.

It is interesting to explore the influence of the different flavors of Eq. (2.72) on the created spin state.

To begin with, in the square cluster Hamiltonian $H^{(1)}$ of Eq. (2.64), we have $-G_{14} = G_{12} = G_{23} = G_{34}$, which implies $a = -b$ and the state becomes

$$\begin{aligned}
|\psi_f^{(1)}\rangle = & \left(|\uparrow\rangle_{15} |\downarrow\rangle_{37} - |\downarrow\rangle_{15} |\uparrow\rangle_{37} \right) \\
& \otimes \left(|\uparrow\rangle_{26} |\downarrow\rangle_{48} - |\downarrow\rangle_{26} |\uparrow\rangle_{48} \right), \quad (2.89)
\end{aligned}$$

which is a product state of two spin-0 Bell pairs of Qbits. This state is pairwise entangled but not quadripartite entangled. Remember $H^{(1)}$ makes a quadripartite entangled CV cluster state. Therefore Schwinger-pairing 2 quadripartite entangled Qmode square cluster states does not necessarily give us a quadripartite spin entangled state.

However, the situation changes when we consider Hamiltonian $H^{(2)}$ of Eq. (2.69), which does not itself make a CV cluster state. There we have $G_{14} = G_{12} = G_{23} = G_{34}$, which implies $a = b$, and

$$\begin{aligned}
|\psi_f^{(2)}\rangle = \frac{1}{2\sqrt{3}} & \left[|\uparrow\rangle_{15} |\uparrow\rangle_{26} |\downarrow\rangle_{37} |\downarrow\rangle_{48} + |\downarrow\rangle_{15} |\downarrow\rangle_{26} |\uparrow\rangle_{37} |\uparrow\rangle_{48} \right. \\
& + |\uparrow\rangle_{15} |\downarrow\rangle_{26} |\uparrow\rangle_{37} |\downarrow\rangle_{48} + |\downarrow\rangle_{15} |\uparrow\rangle_{26} |\downarrow\rangle_{37} |\uparrow\rangle_{48} \\
& \left. - 2 \left(|\uparrow\rangle_{15} |\downarrow\rangle_{26} |\downarrow\rangle_{37} |\uparrow\rangle_{48} + |\downarrow\rangle_{15} |\uparrow\rangle_{26} |\uparrow\rangle_{37} |\downarrow\rangle_{48} \right) \right], \quad (2.90)
\end{aligned}$$

which is a genuinely quadripartite entangled state. We notice that this state closely resembles the well-known Dicke state [59]

$$\begin{aligned}
|D\rangle = \frac{1}{\sqrt{6}} & \left(|\uparrow\rangle_{15} |\uparrow\rangle_{26} |\downarrow\rangle_{37} |\downarrow\rangle_{48} + |\downarrow\rangle_{15} |\downarrow\rangle_{26} |\uparrow\rangle_{37} |\uparrow\rangle_{48} \right. \\
& + |\uparrow\rangle_{15} |\downarrow\rangle_{26} |\uparrow\rangle_{37} |\downarrow\rangle_{48} + |\downarrow\rangle_{15} |\uparrow\rangle_{26} |\downarrow\rangle_{37} |\uparrow\rangle_{48} \\
& \left. + |\uparrow\rangle_{15} |\downarrow\rangle_{26} |\downarrow\rangle_{37} |\uparrow\rangle_{48} + |\downarrow\rangle_{15} |\uparrow\rangle_{26} |\uparrow\rangle_{37} |\downarrow\rangle_{48} \right) \quad (2.91)
\end{aligned}$$

and shares many of its properties. Indeed, while the Dicke state is $|j = 2, m = 0\rangle$ for the total spin, this state is $|j = 0, m = 0\rangle$. Moreover, projecting one spin in the J_z basis, gives us an entangled state, similar to Dicke states. Projecting then another spin results in a bipartite entangled state with the probability $2/3$. Therefore $|\psi_f^{(2)}\rangle$ can be used as a open destination teleportation resource and is robust under single Qbit decoherence since it retains some entanglement between the remaining Qbits under such projections.

2.5 Effect of Non-Ideal Experimental Conditions

The analysis thus far only considers ideal experimental conditions and it would be instructive to consider the robustness of the proposal under loss and imperfect matching of squeezing parameters. Photon loss is extremely detrimental to photon number correlations. Detailed quantitative analysis of the effects of loss quickly becomes intractable with increasing number of modes. A complete analysis of 4 optical modes, generating two entangled spins has been treated in by Ruffin Evans and Olivier Pfister [41]. An interesting case to consider is the effect of mismatched

squeezing interactions strengths i.e the required conditions on G_{ij} are not satisfied. We can immediately see that neither the relative squeezing strengths of the interaction terms within the square or across square change the photon number constants of motion, $N_1 + N_3 - N_2 - N_4$ and $N_5 + N_7 - N_6 - N_8$. Therefore the first two nullifiers J_0 and J_z will still hold, for all values of squeezing interactions. J_x and J_y nullifier relations however crucially depend on the interaction strengths. We make the following observations.

- If the two squares are identical, the 4 nullifiers will always hold for all values of the relative strengths of the intra-square interactions.
- If the two squares are not identical, then the constraint for 4 nullifiers to hold is -

$$\frac{G_{12}G_{34}}{G_{23}G_{14}} = \frac{G_{56}G_{78}}{G_{67}G_{58}} \quad (2.92)$$

In this case the 4 nullifiers will be -

$$J_0 = J_0, J_3 = J_z, \quad (2.93)$$

$$J_1 = J_{x15} - \frac{G_{56}}{G_{12}} J_{x26} + \frac{G_{12}G_{67}}{G_{23}G_{56}} J_{x37} - \frac{G_{58}}{G_{14}} J_{x48}$$

$$J_2 = J_{y15} + \frac{G_{56}}{G_{12}} J_{y26} + \frac{G_{12}G_{67}}{G_{23}G_{56}} J_{y37} + \frac{G_{58}}{G_{14}} J_{y48} \quad (2.94)$$

Therefore when the squares are not identical, the nullifiers are no longer the total spin operators. So the resultant state cannot be written as a total spin zero state.

- If this condition is not satisfied, then we can no longer have 4 nullifiers. J_0 and J_z are the only two nullifiers which makes the state and eigenstate of total J_z .

2.6 Conclusion

The close connection of twin two-Qmode Gaussian entanglement to maximal bipartite spin entanglement, Eqs. (1.70-1.71), initially suggested that the simulation of entangled spins using optical Qmodes might be possible. Such a correspondence of Gaussian and non-Gaussian Wigner functions, coupled to the availability of photon-number-resolving detection methods, is a fascinating prospect, not to mention its possible implications for quantum simulation. Another application of this work can be for atomic ensemble spin squeezing. Multipartite singlet states and spin squeezed states are highly desirable states for use in decoherence resistant

entanglement memories. Such states are created by using squeezed optical modes to excite atom ensembles.

We attempted to explore this correspondence by recasting different families of H-graph states as spins, by way of the Schwinger representation. While we found that this correspondence is not straightforward for multipartite systems—and even seems to fail systematically in the case of paired CVGHZ states—we have nonetheless obtained nontrivial results, including a genuine multipartite entangled spin-1/2 state generated by a multimode squeezed, albeit not multipartite entangled CV state. Moreover, closely related Qmode Hamiltonians, which make significantly different states, can still have the same spin nullifiers, which hints at a possible degeneracy of the nullifier picture in this case.

We are grateful to Natasha Gabay and Nicolas Menicucci at the University of Sydney for nonlocal stimulating discussions and free-flowing exchange of ideas. This work was supported by the U.S. National Science Foundation grants No. PHY-1206029, No. PHY-0960047, and No. PHY-0855632.

Chapter 3

Tomography using photon-number-resolving detection

Here we detail our work done on the quantum tomography of optical states using photon-number-resolving detectors. This work was published in Journal of Optical Society of America B in October 2014 [60].

In section 1.3, we explained the theoretical foundation of measurement of Wigner function using photon number resolving measurement and displacement. In section 3.1, we describe the TES detector and the acquisition and processing of PNR signals. In section 3.2, we describe the quantum tomography experimental setup starting from the experimental implementation of the displacement operator. We then present the measurement results of the experiment in section 3.3. We discuss experimental limitations (losses), and then we conclude.

3.1 Photon-number-resolving detection setup

Our TES system contains 8 fiber-coupled thin-film tungsten devices fabricated at NIST, optimized for detection at 1064 nm [3]. The TES devices are cooled by a cryogen-free adiabatic demagnetization refrigerator and temperature stabilized at 100 mK. The TES detector is voltage-biased [61], and self-heats into the superconducting transition illustrated in Fig. 3.1. When a photon is absorbed, the

energy of the photon is thermalized in the electrons of the TES and there is a small temperature rise that causes a small measurable increase in the resistance of the TES. The change in resistance causes a change in current flowing through the device which is measured using a SQUID amplifier system.

Two-photon absorption causes a larger temperature change and therefore a larger signal than single-photon absorption, and this results in photon-number resolution.

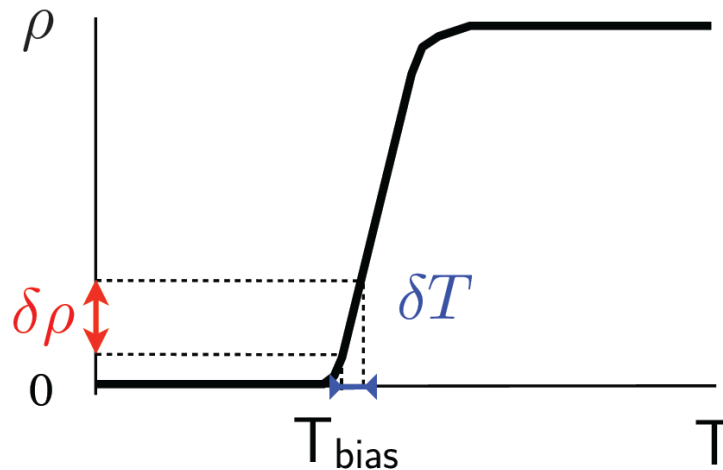


FIGURE 3.1: Principle of operation of the TES. When the TES is temperature-biased at the edge of the superconducting transition T_{bias} — or on the steep transition slope — any temperature variation δT due to photon absorption is translated into a measurable resistance change δR .

The maximum measurable photon number is ultimately determined by the amplitude of the steep transition slope (Fig. 3.1): upon reaching its top, the TES will saturate if additional photons are absorbed. There exist, however, methods to cope with such undesirable conditions as TES saturation: on the one hand, the cooling time would still provide information about the photon number in such an optical pulse, if no more photons were impinging until cooling was complete [62]. Moreover, the saturation does not completely erase all photon-number information (unlike the schematic plot of Fig. 3.1, the resistance does retain a weaker dependence on temperature in the normal conducting regime) and a recent, more sophisticated analysis [63] can also yield higher photon number statistics into the saturation regime. In this experiment however, we truncated our photon number analysis to fall within the transition slope.

Note that the single-TES restriction of the maximum number of measurable photons (here 5 photons at 1064 nm) entails a restriction of the Hilbert space to the Fock-state basis $\{|0\rangle, |1\rangle, |2\rangle, |3\rangle, |4\rangle, |5\rangle\}$. As noted in Ref. [16], when the

average detected photon number approaches the cutoff limit of the detector, statistical errors increase drastically. Therefore this quantum tomography method requires states with negligible probabilities of measuring photon numbers higher than 5. However, in principle, with 8 independent TES channels, our system could achieve PNR detection up to 40 photons, and sophisticated data processing methods, mentioned in the next section, allow to push that limit further.

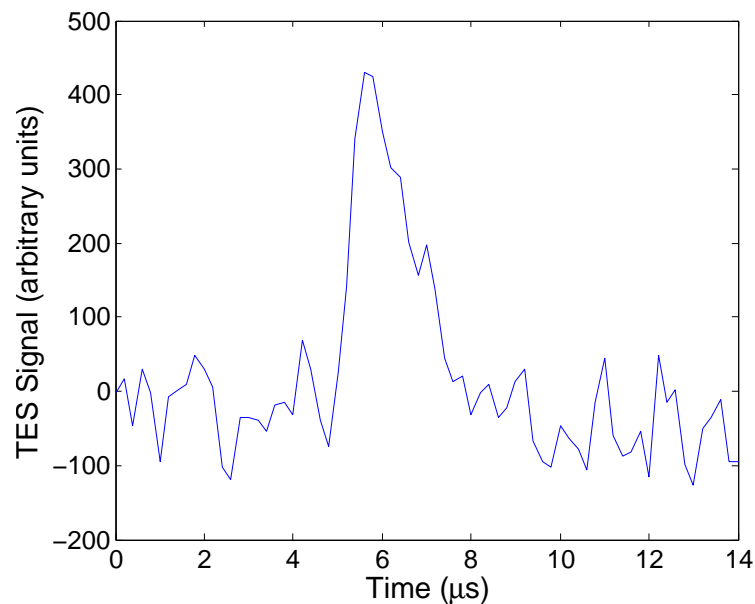


FIGURE 3.2: An example of raw TES data showing a single photon detection event. The detection peak can be clearly distinguished from the noise.

3.1.1 Signal acquisition

The TES signal is relayed directly from the output channels using BNC cables to a 4 channel 125Mbit Alazar data acquisition PCIe card. The device drivers of the Alazar card are compatible with MATLAB on Windows. The MATLAB drivers were written at NIST, Boulder CO by the group of Thomas Gerrits.

The Alazar card can sample data at many different sampling rates. However the characteristic TES response time to a photon detection is fixed. A typical detection event comprised a rising edge of about 700 ns, corresponding to the response time of the TES detection chain, followed by a cooling decay tail of a couple μ s. Figure 3.2 displays a typical example. All photon detection events, from 1 to 5 photon events have the same characteristic shape only with different

peak heights. Note that the detector is still active during the cooling tail and that there is no dead time as long as the TES is on the transition slope.

We tried different sampling rates and decided to use 5 Ms/s. This gives us a data sample every 200 ns and at least 3 data samples in the rising edge for characterization of photon events. Each sample was saved on the computer as a 16-bit integer, but only 14-bits were useful from the digitizer. Data is collected in batches of continuous detection after which the packet is transferred to the computer and the digitizer rearmed for receiving the next batch of data. The size of the batch is decided by the memory restrictions of the Alazar card which is 8 MBytes per batch, or 2^{22} points per batch. Therefore each batch of data corresponded to 0.84 s of uninterrupted data. This process could be repeated if necessary to join multiple batches data. However, in this experiment, all Wigner function measurement data was exactly 1-batch long and thus contained no dead time.

3.1.2 Signal processing and photon “pileups”

The signal processing and analysis subroutines were written by me. The basic principle of these routines was built collaboratively by Reihaneh Shahrokhshahi and I based on prior routines written by our collaborator Aaron Miller.

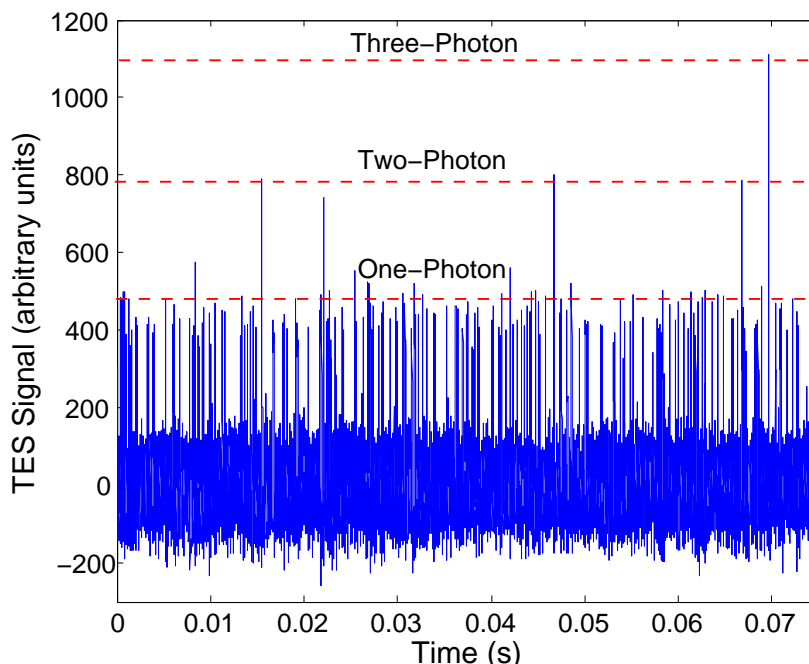


FIGURE 3.3: Raw TES data for a CW beam showing distinct one-, two-, and three-photon peaks. The signal levels are indicated by the red dashed lines.

Figure 3.3 displays an example of PNR detection with the TES, over a longer time range than Fig. 3.2.

In this experiment, continuous-wave (CW) optical fields were measured and all TES signals were derived from continuous photon streams. Therefore photon arrivals are completely independent and random events. Therefore the primary step in the analysis is locating photon events. Once the photon events are identified they have to then be classified as 0,1,2... photon events. This step is complicated by the variation and fluctuations in the detection peak heights as we can see in Fig. 3.3, due to noise in the readout electronics. 0 photon events are smaller than the characteristic photons of the signal. They originate either from electronic noise or external light and therefore are counted as part of the noise.

Finally we have to consider the case of 'photon pileup'. In a photon pileup event, another photon impinges on the TES very soon after a first photon, while the signal is still on the decaying tail. An example of pileup is the rightmost (double) peak in Fig. 3.4(a). In the experiment, the photon flux was kept low enough that most detection peaks were separated by more than the TES cooling time.

In order to achieve accurate photon counting, including in the presence of pileups, we adopted the following procedure, whose steps are illustrated in Fig. 3.4.

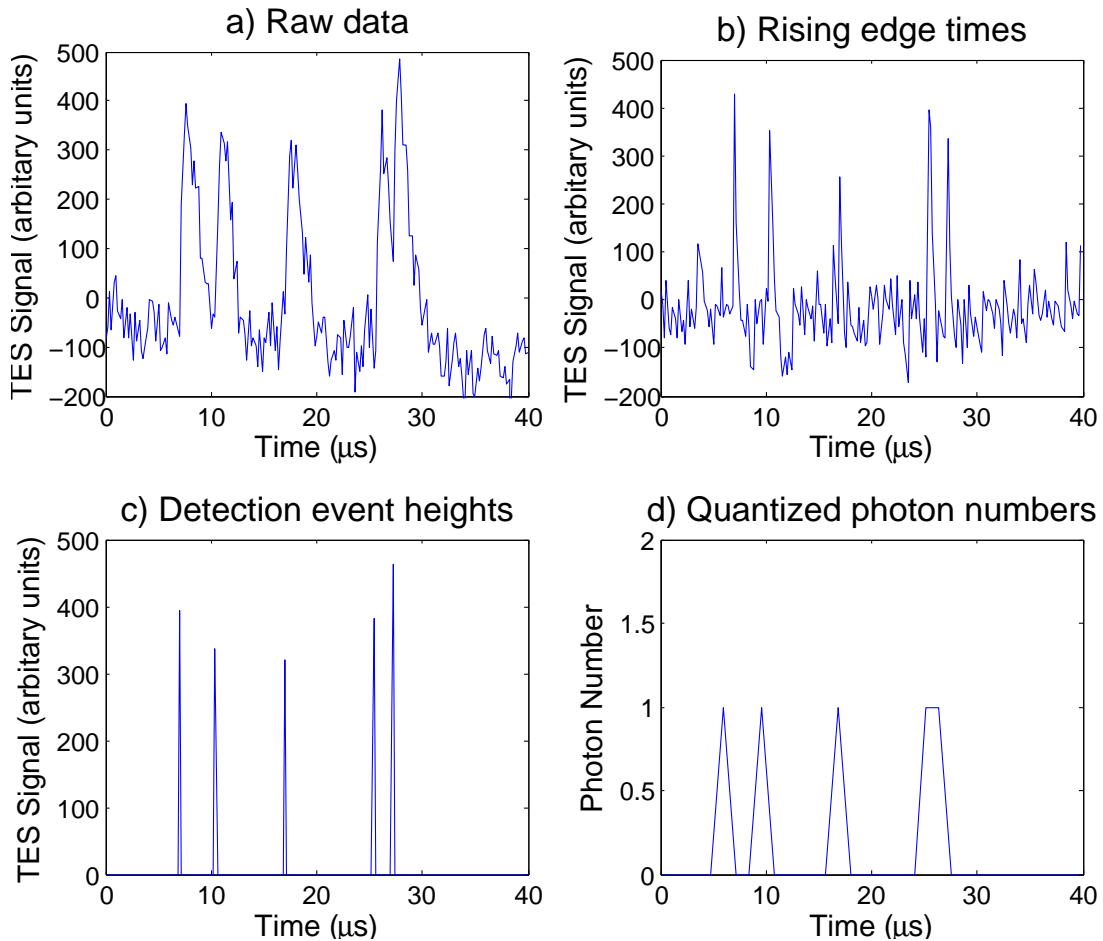


FIGURE 3.4: Steps in the processing of raw analog data into quantized photon-count data. (a), a small sample of the raw data. shows 3 single peaks and 1 “piled up” double peak, where the last photon was detected before the detector was cooled back the nominal bias temperature. (b), rising edge detection results. The procedure correctly detected 5 rising edges. (c), encoded signals, made of the photon detection times along with the value of the maximum peak height within $1.2 \mu\text{s}$ of each event. (d), final quantized photon-counts determined using the thresholds defined in the histogram of peak heights in Fig. 3.5.

First, we identified each detection event by finding rising edges in the signal. A rising edge is defined as a detection event if it rises at least 40% of the average height of the single photon above the mean noise level. This threshold is set manually during the calibration process. For example, in Fig. 3.2, the threshold would typically be at 200 arb. units. The starting time of each detection event is recorded. Figure 3.4(b) displays the event times corresponding to the signal in Fig. 3.4(a). The algorithm then stores the maximum signal in the $1.2 \mu\text{s}$ following each starting time and this maximum is stored as well, see Fig. 3.4(c). The analysis thus assumes a response time of $1.2 \mu\text{s}$. Hence, if two photons were absorbed with $1.2 \mu\text{s}$ of each other, they would be counted as one two-photon event, not as two

one-photon events; this is determined in the final, quantization stage. First, we form the histogram of recorded signal heights, displayed in Fig. 3.5, where we can

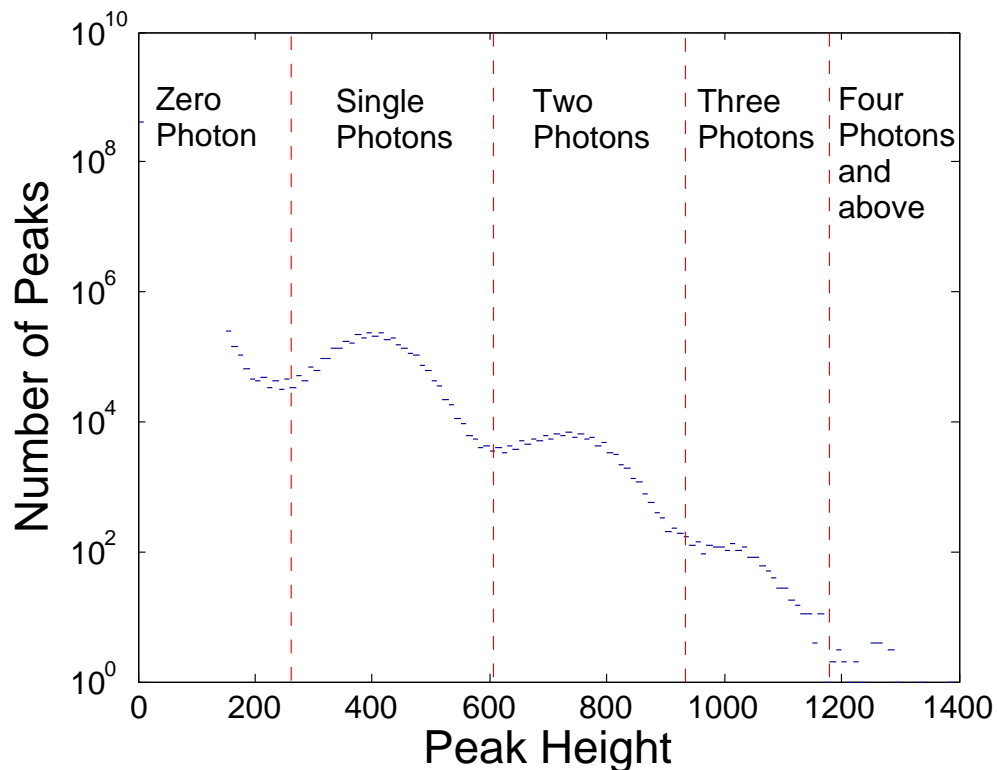


FIGURE 3.5: Histogram of peak heights from the sample of Fig. 3.4(a). The histogram bins define the photon-number quantization thresholds.

clearly see three well-separated peaks (the “zero-photon” area is likely due to noise, external light and blackbody radiation). From this histogram, we can now define the photon-number quantization thresholds. Using these thresholds, the quantized photon-number signals can be obtained and are displayed in Fig. 3.4(d). Note that the rightmost pileup peak is resolved here and accounted for as two one-photon events.

3.1.3 Detection efficiency

The detector efficiency is an important factor in accurate state reconstruction. Losses not only introduce noise in the statistics but can also change the very state being measured. Detailed analysis of the effect of loss can be found in Refs. [15, 16] and references therein.

In this work, we restricted ourselves to coherent states. Our preliminary characterization of the overall system determined the detection efficiency of our fiber-aligned TES setup to be between 70% - 90%. The reason for this large margin of error is because the TES operates in regime where it cannot be verified by any other detector in the lab. The TES can accurately measure power only at the femto-Watts level, but no other detector can even detect pico-Watts of light. Therefore, the TES can only be calibrated in one of 3 ways, 1. using another already calibrated TES, 2. using extremely precise and calibrated attenuators, and 3. using a highly correlated photon source and measuring the maximum attainable correlation detected by the TES. The first one is a circular, unhelpful solution. The second solution requires sophisticated calibration equipment that is not available to us. The TES was calibrated at NIST by this method and certified to be 95 % efficient before it was installed in our lab. We know that we have additional 10 % loss at the free-space-to-fiber coupler, putting our maximum efficiency at 85 %. Finally the third method is known to be an extremely difficult experiment and being actively pursued by groups around the world. We hope to be able to attempt that experiment in the future.

Highly non-classical states are very strongly affected by loss and quickly lose their characteristics. However, we limited our experiment to coherent states. Coherent states are known to be immune to losses. A detailed treatment [16] shows that loss only decreases the observed peak of the coherent state Wigner function, but preserves its Gaussian nature. As we shall see in section 3.3, for coherent states even the precise value of the efficiency is not required for validation of the state reconstruction.

3.2 Experimental Setup

3.2.1 Displacement

As described in section 1.2, we need to implement a displacement operator on the state we want to measure. Recall that we can reduce the action of the displacement operator on the Wigner function of a general state as a translation along q by $Re(\alpha)$ and along p by $Im(\alpha)$. Therefore measurement of $W(0, 0)$ on a state displaced by α effectively a measurement of $W(-Re(\alpha), -Im(\alpha))$ of the original state.

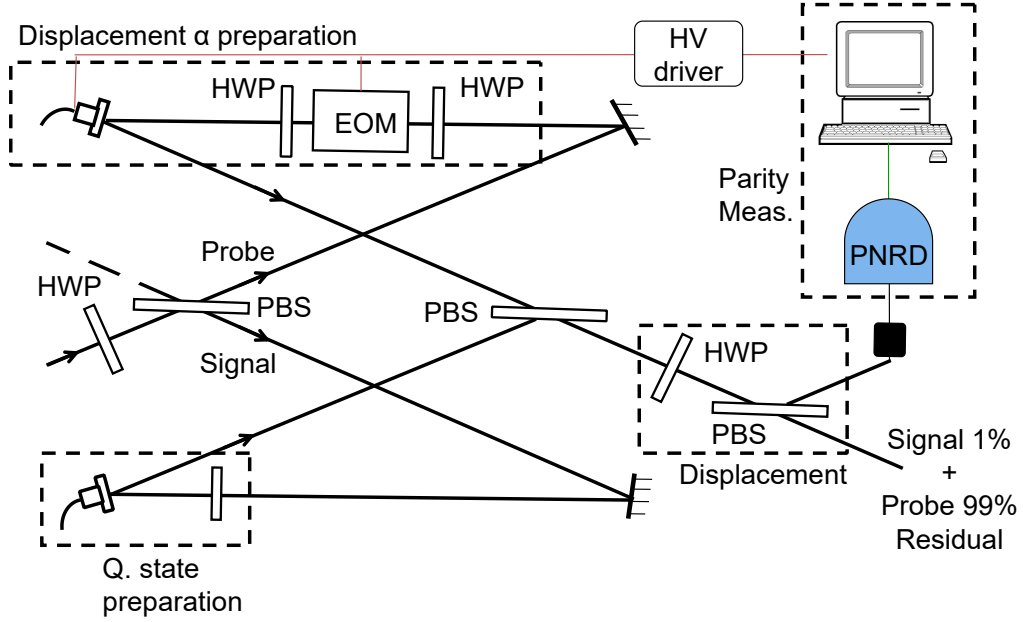


FIGURE 3.6: Experimental setup for the quantum tomography of a coherent state using a coherent field input and photon number measurements. The signal optical path is that of the quantum state to be measured. The probe optical path is that of the “local oscillator” whose field generates the phase-space displacement. PBS: polarizing beam splitter; EOM: electro-optic modulator; HWP: halfwaveplate; ND: neutral density; HV = high voltage.

In practice, the displacement operator can be achieved by combining the quantum signal with the coherent state $|\alpha\rangle$ at a BS. First we can look at the effect of the displacement operator in Heisenberg picture, using the Baker-Campbell-Hausdorff formula

$$\begin{aligned}
 D^\dagger(\alpha) a D(\alpha) &= e^{\alpha^* a - a a^\dagger} a e^{\alpha a^\dagger - \alpha^* a} \\
 &= a + [\alpha^* a - \alpha a^\dagger, a] \\
 &= a + \alpha
 \end{aligned} \tag{3.1}$$

Now we recall from Eq. (1.16) that the action of the BS on mode 1 is given by

$$U_{BS}^\dagger a_1 U_{BS} = \tau a_1 + \rho a_2$$

Here τ and ρ are the field transmission and reflection coefficients respectively ($r^2 + t^2 = 1$). Now if the quantum mode to be displaced is mode 1, mode 2 is a coherent state $|\alpha\rangle$, and the BS has $\rho \ll 1$, $\tau \simeq 1$ then we can approximate the

above as

$$U_{BS}^\dagger a_1 U_{BS} \simeq a_1 + \rho\alpha \quad (3.2)$$

This is exactly the operation of the displacement operator. Therefore in the approximation $\tau \simeq 1$, the action of the BS is to displace the mode a_1 by $\rho\alpha$.

However, it is important to remember that the displacement operator thus implemented is an approximation. A more complete analysis for the exact can be found in [64]. Using this implementation, by displacing the state by $\alpha = (q + ip)/\sqrt{2}$ the Wigner function measured by PNR statistics at the beam splitter's output will be [15]

$$W_{\text{out}}(0, 0) = \frac{1}{T} W\left(\frac{rq}{t}, \frac{rp}{t}; -\frac{r}{t}\right), \quad (3.3)$$

where the function $W(q, p; s)$ on the right-hand side is the standard s -ordered quasi-probability distribution [10], which coincides with the Wigner function for order parameter $s = 0$. Hence, by choosing $\rho \simeq 0$ and by scanning $\alpha = (q + ip)/\sqrt{2}$ in the (q, p) phase space, we can measure the complete Wigner function.

3.2.2 Setup

The experimental setup schematic is depicted in Fig. 3.6. The whole experiment was set up on a 24 inch-thick floating optical table and all optical paths were protected from air drafts by acrylic plastic enclosures. All light was emitted at 1064 nm by a monolithic Nd:YAG laser, of high intrinsic stability (1 kHz FWHM linewidth). The optical mode was coupled to single-mode fibers for 1550 nm light, anti-reflection (AR) coated at 1064 nm, by way of aspheric lenses, also AR-coated, and a 5-axis fiber aligner. These fibers entered the cryostat via throughputs and were then directly coupled to the superconducting detectors by silicon micro-machined self-alignment [65]. As mentioned above, measuring the Wigner function requires, besides PNR detection, quantum state displacement over the whole region of interest of the phase space. The displacement operator was implemented by interfering the signal field with a local oscillator (LO) coherent field at a nearly fully transmitting beam splitter. The interference visibility of the signal and LO fields was $v = 98\%$. The amplitude $|\alpha|$ and phase $\arg(\alpha)$ of the transmitted coherent field were respectively varied using an amplitude electro-optic modulator

(EOM) and a piezotransducer-actuated mirror. The EOM we used was a home-made device built out of an X -cut, 20 mm-long RbTiOAsO₄ (RTA) crystal, which was temperature controlled to about a mK by a commercial temperature controller. The EOM has a phase range of around 450° using a voltage range of 0-300 V. The voltages applied to EOM and piezo mirrors were generated by low-noise, high-voltage drivers controlled by the analog output ports of a lock-in amplifier. The lock-in amplifier was computer-controlled to output desired voltages through its auxiliary A/D outputs, which have 1 mV resolution, ± 10 V range, and under 100 μ s settling time. However, the fastest switching time we observed was 10 ms, which is likely a remaining limitation of the interface rather than the limit of the lock-in amplifier itself.

3.2.3 Procedure

Prior to the experimental run, a calibration run was required to get the scanning voltages and expected values of the experiment.

In the calibration run, first both signal and probe were blocked and the background was recorded. The background for the TES should be very small ($< 1\%$) compared to the signal. If this was not the case then it indicated an external source of light contaminating the signal. In this case we traced all possible sources of light in the room, excluded them one-by-one and blocked any light that is found to be reaching the detector from external sources. Sometime the external source could be electronic devices such as cellphones. There no way to block broad sources such as room light or sunlight and hence all lights must be off and doors closed during the experiment.

Next the signal beam was measured alone, without the probe, and its mean intensity recorded. This is the value used as the expected value of $|\alpha_0|$ in the Wigner function measurement.

Next the signal was blocked and the displacement probe beam is characterized. The voltage on the EOM was scanned through its entire range and the intensity of the probe recorded at every step. This calibrates the EOM voltage to intensity relationship. Here two important details needed to be considered. First the displacement field intensity must span the entire phase space where the Wigner function of the signal is expected to lie. If that was not the case then the intensity

of the signal has to be adjusted until it lay well within the scanning region. Secondly, the granularity of scan had to be decided to give the best results. Using the voltage-intensity calibration appropriate values of the voltage had to be chosen such that all the features of the Wigner function are given equal importance and there are no regions with too few or too many data points. Therefore a voltage list was constructed which consisted of manually chosen voltages which spanned the intensity as evenly as possible. This concludes the calibration run.

The main experimental run was completely automated. The run was controlled by the MATLAB routine which changes the lock-in amplifier output voltage and then runs the Alazar data acquisition, repeating this process for the entire voltage range required to scan the phase space.

The amplitude $|\alpha|$ of the displacement field was varied in 40 steps while its phase $\arg(\alpha)$ went through 60 steps from 0 to 2π . At each point $(|\alpha|, \arg(\alpha))$ of the polar scan the TES signals were processed to yield photon-counting statistics, hence photon-count probabilities and also parity measurements. Phase space scans consisted of sampling a sequence of circles with increasing radius, since changing the voltage applied to the EOM tuning $|\alpha|$ required a settling time of the order of 2 s, whereas $\arg(\alpha)$ could be scanned much faster, as the phase modulator driver had much higher, 10 kHz bandwidth. For each point in phase space, the TES output was digitized and processed to obtain the photon statistics in real-time. The parity measurement was subsequently calculated from the statistics and saved.

We experimented with a variety of scan parameters both in amplitude and phase. The number of points to be scanned is a compromise between runtime of the experiment and granularity of the measurement. Longer runtimes do degrade the results due to drifts in experimental conditions and after a point do not result in any added accuracy.

3.3 Results and analysis

3.3.1 Reconstruction

In Fig. 3.7, we plot the measured Wigner functions of the vacuum, of a weak coherent state, and of a phase-diffused statistical mixture of coherent states. The

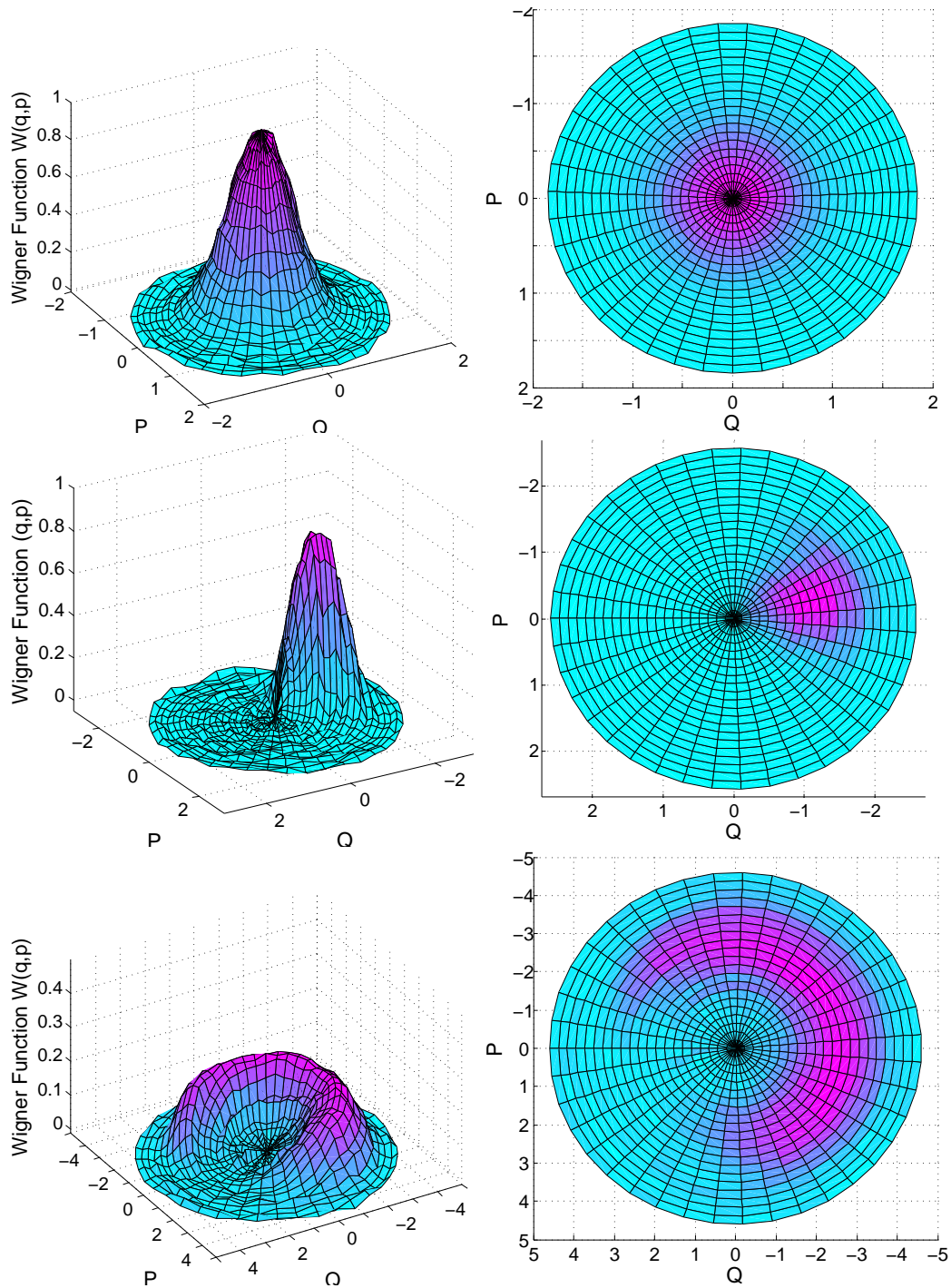


FIGURE 3.7: The measured Wigner functions and contours of, top, vacuum; center, a coherent state; bottom, a phase-diffused coherent state. All plots are interpolated for 22 amplitude points and 40 phase points.

phase diffusion was obtained by applying a 100 Hz sine waveform to the piezo mirror. The radial coordinate was obtained from the average number of photons detected for the blocked signal path. Thus the graphs were parametrized with the complex variable $\beta = \sqrt{\eta}\alpha$, where α is the probe field reflected at the BS and η is

the detection efficiency.

Each 0.84 s data packet (see above) was divided into bins of size $\tau = 0.1$ ms long, which amounted to about 8400 bins per point in phase space. The bin duration defined the temporal envelope of the measured mode. Like in Banaszek et al.'s original experiment, this was shorter than the laser's coherence time (here, 1 ms).

Using a detector temporal envelope which is different from laser coherence can be an issue when trying to characterize quantum states. For example if the quantum state generated is a Fock state $n=2$ with a temporal window 1ms, then using a 0.1ms window might give us a lot of $n=1$ and $n=0$ state components. This is because, in general, temporal basis vectors are not orthogonal, hence there is a non-zero, but incomplete, overlap of the signal temporal envelope with the detector envelope. However this mismatch is of no consequence in the case of coherent states. Temporal mismatch in case of coherent states only affects the value of α_0 and does not change the nature of the quantum state. Therefore when characterizing and comparing coherent states it suffices to keep a uniform detector temporal bin size across all measurements, which is what we did in this work.

3.3.2 Verification

We investigated the weak coherent state case to verify the accuracy of our state reconstruction. Here and henceforth, we discard the normalization constant from the Wigner function, so that the maximum of the function is 1. Therefore the theoretical Wigner function of a coherent state $|\alpha_0\rangle$ becomes

$$W(\alpha) = e^{-2|\alpha - \alpha_0|^2}. \quad (3.4)$$

Notice the extra factor of 2 in the Gaussian term. The reason the two appears is because when we go write $W(\alpha)$, we are implying that the integrating variable is α instead of q, p . Here $\alpha = (q + ip)/\sqrt{2}$ therefore the extra factor 2 is required to compensate for the $\sqrt{2}$.

This value does not consider the effects of losses and displacement approximation from section 3.2.1. A more realistic analysis [15, 16] takes into account sub-unity detector efficiency, losses on the quantum signal and the non-ideal visibility of the signal-probe interference at the displacement beamsplitter BS2. The measured

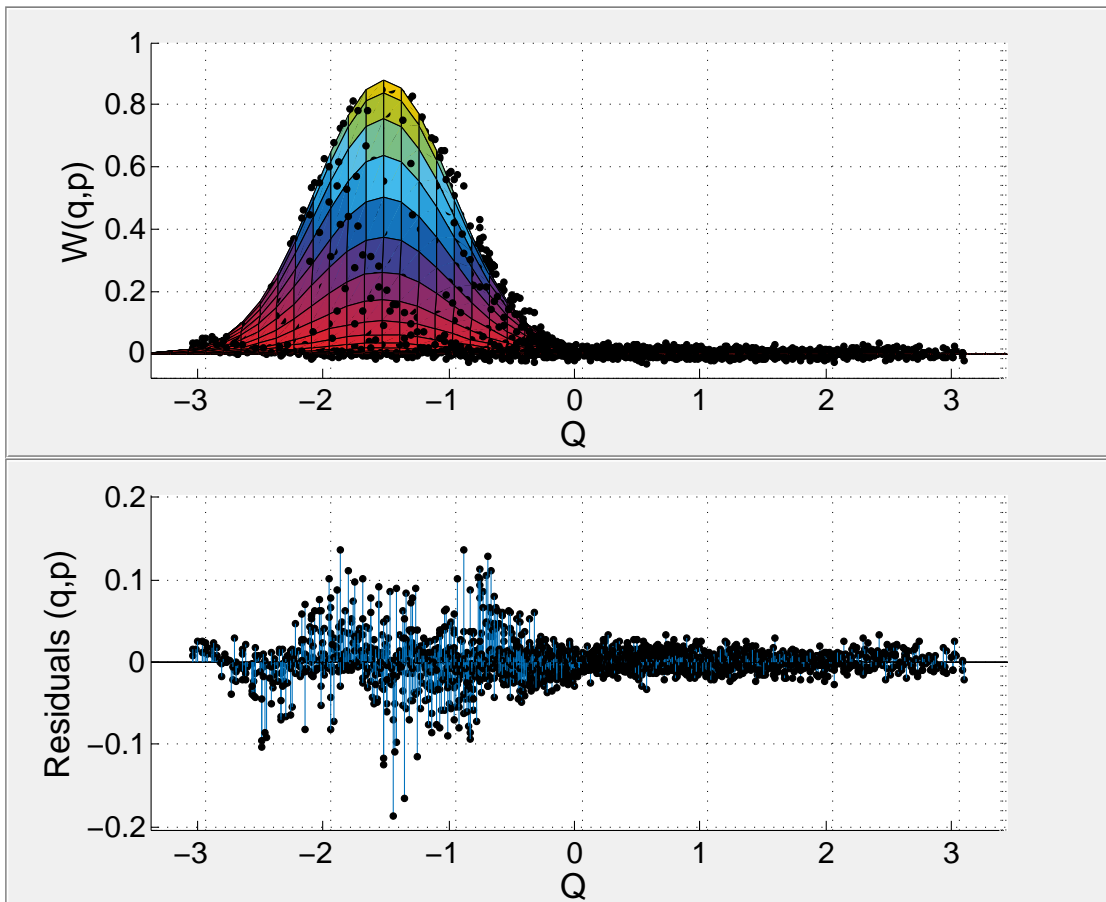


FIGURE 3.8: Gaussian fit (top) and residuals (bottom) of the coherent-state tomographic data. The fit function was $W_{\text{fit}}(q, p) = a + b \exp[-m|(q - q_0)^2 + (p - p_0)^2|]$. The correlation coefficient was $R^2 = 0.966$.

Wigner function is given by

$$W(\beta) = e^{-2|\beta - \sqrt{V}\eta t\alpha_0|^2 - 2(1-V)\eta t^2|\alpha_0|^2}, \quad (3.5)$$

where

$$V = \frac{v}{2 - v} \quad (3.6)$$

is a measure of the overlap of signal and probe, η is the effective efficiency of the detector, t is the displacement BS transmissivity and v is the visibility of the interference of signal and probe.

In this experiment, we had $v = 0.98$, $t^2 = 0.99$, yielding $V = 0.97$. We recall that the measured probe field in Fig. 3.7 is already β . Further, the measured signal at the time of calibration already takes into account the effect of loss and mode mismatch, hence the measured signal is $|\beta_0|^2 = \eta|\alpha|^2 = 2.553$, therefore

TABLE 3.1: Fit results for model function
 $W_{\text{fit}}(q, p) = a + b \exp[-m|(q - q_0)^2 + (p - p_0)^2]$.

Coefficients	Fit	Theory (3.7)
a	0.000(2)	0
b	0.877(10)	0.867
m	1.72(3)	2
p_0	0.248(6)	
q_0	1.532(6)	
$\sqrt{q_0^2 + p_0^2}$	1.552(6)	1.567

$|\beta_0|=1.567$. Thus, our theoretical Wigner function was

$$W_{\text{th}}(\beta) = 0.867 e^{-2|\beta-1.567|^2}, \quad (3.7)$$

which we compared to a fit of the observed data in Fig. 3.7. The fit is plotted in Fig. 3.8 and the results are presented in Table 3.1. Note that the actual phase angle of the coherent state $[\arctan(p_0/q_0)]$ is not relevant here, even though we did fit it, only the amplitude $\beta_0 = \sqrt{q_0^2 + p_0^2}$ is. Although the correlation coefficient of the fit was high ($R^2 = 0.966$), an inspection of Table 3.1 and of the residuals in Fig. 3.8 show that the agreement is only qualitative.

There are many possible sources of error to consider here. Some lend themselves to be compensated or corrected, others can only be reduced but not eliminated. We believe that a large source of errors and noise lies in the phase stability. The data acquisition lasts for over 4000 s for the complete data and we assume that the signal phase remains stable during this process. While our experimental setup is intrinsically very stable, phase and temperature drifts are unavoidable over such a duration. One way to mitigate these effects would be to lock the optical phases and path differences to a reference. Another source of error is the effect of power on any optical element. Any testing and calibration has to be done at powers close to milliWatts, while the experiment is conducted at femtoWatts. The 12 orders of magnitude difference might induce some differences in phase and loss in elements like fibers and EOM's. This can be mitigated by calibrating all elements relative to each other rather than in absolute terms. Of course absolute calibrations at low power is impossible without a method of accurately measuring the detector efficiency, which itself is another source of error.

3.4 Conclusion

In conclusion, we experimentally demonstrated, for the first time, quantum tomography with PNR measurements of more than one photon. We limited this initial investigation to the loss immune coherent state and coherent-state mixture with phase noise and got reasonable agreement with expected values on key parameters. Since the detector's non-ideal efficiency cannot be compensated in this method of measuring the Wigner function [15], it is only possible due to the recent development of high efficiency PNR detectors.

This work was supported by the U.S. National Science Foundation, under grants No. PHY-0960047 and PHY-1206029, and by the University of Virginia.

Chapter 4

Conclusion

Quantum physics has been tested in thousands of experiments over the years and it has stood the test of time. Yet as technological advances open up new areas of research, exploring the fundamental physical nature in these new frontiers is of critical importance. The Wigner quasi-probability distribution is an elegant and essential tool for characterizing quantum states. Direct detection of the Wigner function makes their measurement straightforward, without the need for complex mathematical post-processing. As Antoine Royer put it, "the method makes the Wigner function more meaningful and natural" rather than an esoteric mathematical description [13].

Our experiment demonstrates the experimental viability of this method with photon number resolving detectors. The logical next project is to measure the Wigner function of highly non-classical states such as Fock states. To achieve that a much better calibration of the losses and phase stability of the system is required. As suggested by Banaszek et al. [16], this method also generalizes very naturally to multimode tomographic reconstruction, which is a promising direction of research.

Characterization of non-classical states have important applications in quantum information and quantum computing. Recent proposals have highlighted the requirement for generating highly non-classical ancilla states which are necessary to circumvent the no-go theorems for all Gaussian quantum computing [8]. Here, we present a step towards an alternate approach, that of using photon number measurements coupled with CV entangled states to simulate spin entanglement. We discovered that quadripartite spin states which are entangled to make total spin zero states can be achieved using quadripartite Gaussian entanglement. Moreover,

we discovered that the number of entangled spins and the strength of their entanglement is *independent* of the strength of the non-linear squeezing interaction, in the absence of losses.

These results are intriguing and we believe that a possible avenue to better understand the underlying theory might be a general group theoretical approach involving the connections between $\text{Sp}(4, \mathbb{R})$ and $\text{SU}(2)$. Although well known in quantum optics [66, 39], this interplay between the $\text{SU}(1,1)$ and $\text{SU}(2)$ groups is compelling and its consequences for entanglement have not yet been elucidated, to the best of our knowledge. A more general description, such as that involving the symplectic group $\text{Sp}(4, \mathbb{R})$ [67], might be useful here as it already has been for the study of Gaussian entanglement [68], but these theoretical directions are beyond the scope of this thesis.

We anticipate that this will be a powerful way to generate and simulate not just Qbit but multipartite high-spin entanglement. Recent theoretical and experimental demonstrations [69, 70, 71] of scalable generation of large multimode squeezed states makes this a very promising avenue of research.

Appendix A

Derivation of the 4 spin entangled state

The derivation of the post-selected substate for 4-Qbit given in Eq. (2.87) can be done more rigorously (and considerably less elegantly) -

We know that $N_1 + N_3 = N_2 + N_4$ and $N_5 + N_6 = N_7 + N_8$. Therefore we can write a general ket of the state as

$$\begin{aligned}
 |\psi\rangle &= \sum_{s=0}^{\infty} \sum_{n=-s}^s \sum_{i,k}^{s-n} \sum_{j,l}^{s+n} c_{ijklns} |\psi\rangle_{ijklns} \\
 &= \sum_{s=0}^{\infty} \sum_{n=-s}^s \sum_{i,k}^{s-n} \sum_{j,l}^{s+n} c_{ijklns} |s-n-i\rangle_1 |s-n-k\rangle_2 |i\rangle_3 |k\rangle_4 \\
 &\quad \otimes |s+n-j\rangle_5 |s+n-l\rangle_6 |j\rangle_7 |l\rangle_8
 \end{aligned} \tag{A.1}$$

We can see trivially that -

$$J_0|\psi\rangle = 0; \Delta J_0|\psi\rangle = 0; \tag{A.2}$$

$$J_z|\psi\rangle = 0; \Delta J_z|\psi\rangle = 0, \tag{A.3}$$

since we used these relations to form the state. Now we need to find the conditions on the coefficients c_{ijklns} such that the other 2 nullifiers are satisfied as well. So

lets focus on J_x first. Now,

$$\begin{aligned}
J_x &= J_{x15} + J_{x37} - J_{x26} - J_{x48} \\
&= J_{+15} + J_{+37} - J_{+26} - J_{+48} + J_{-15} + J_{-37} - J_{-26} - J_{-48} \\
\implies \langle J_x \rangle &= 0
\end{aligned} \tag{A.4}$$

The above result is easy to see since either pair production or pair annihilation within a square is required for $|\psi\rangle_{ijklns}$ to become $|\psi\rangle_{i'j'k'l'n's'}$, neither of which is present in J_x . They are present, however in $(J_x)^2$. So lets see what are the non zero terms in $\langle (J_x)^2 \rangle$. We can simply calculate what this expectation value will be for the state we initially supposed in terms of the coefficients c_{ijkln} . We also know that this expectation value should be 0 from our earlier proof. Just by inspection we can see the terms that only half the terms will survive -

$$\begin{aligned}
\langle (J_x)^2 \rangle &= \langle (J_{+15} + J_{+37} - J_{-26} - J_{-48})(J_{+15} + J_{+37} - J_{-26} - J_{-48}) \rangle \\
&+ \langle (J_{+15} + J_{+37} - J_{-26} - J_{-48})(J_{-15} + J_{-37} - J_{+26} - J_{+48}) \rangle \\
&+ \langle (J_{-15} + J_{-37} - J_{+26} - J_{+48})(J_{+15} + J_{+37} - J_{-26} - J_{-48}) \rangle \\
&+ \langle (J_{-15} + J_{-37} - J_{+26} - J_{+48})(J_{-15} + J_{-37} - J_{+26} - J_{+48}) \rangle \\
\langle (J_x)^2 \rangle &= \langle (J_{+15} + J_{+37} - J_{-26} - J_{-48})(J_{-15} + J_{-37} - J_{+26} - J_{+48}) \rangle \\
&+ \langle (J_{-15} + J_{-37} - J_{+26} - J_{+48})(J_{+15} + J_{+37} - J_{-26} - J_{-48}) \rangle
\end{aligned} \tag{A.5}$$

Both of the terms of the above sum resemble the expression $\langle AA^\dagger \rangle$. Such terms can only be real and positive. Therefore both of them must be individually 0 for

their sum to be 0.

$$\begin{aligned}
& (J_{+15} + J_{+37} - J_{-26} - J_{-48})|\psi\rangle \\
&= (\sqrt{(s-n-i+1)(s+n-j)}c_{ijklns}|s-n-i+1\rangle_1|s-n-k\rangle_2 \\
&\quad |i\rangle_3|k\rangle_4|s+n-j-1\rangle_5|s+n-l\rangle_6|j\rangle_7|l\rangle_8 \\
&\quad + (\sqrt{(i+1)(j)}c_{ijklns}|s-n-i\rangle_1|s-n-k\rangle_2|i+1\rangle_3|k\rangle_4 \\
&\quad |s+n-j\rangle_5|s+n-l\rangle_6|j-1\rangle_7|l\rangle_8 \\
&\quad - (\sqrt{(s-n-k)(s+n-l+1)}c_{ijklns}|s-n-i\rangle_1|s-n-k-1\rangle_2 \\
&\quad |i\rangle_3|k\rangle_4|s+n-j\rangle_5|s+n-l+1\rangle_6|j\rangle_7|l\rangle_8 \\
&\quad - (\sqrt{(k)(l+1)}c_{ijklns}|s-n-i\rangle_1|s-n-k\rangle_2|i\rangle_3|k-1\rangle_4 \\
&\quad |s+n-j\rangle_5|s+n-l\rangle_6|j\rangle_7|l+1\rangle_8 \\
&= (\sqrt{(s-n-i+1)(s+n-j)}c_{ijklns} + \sqrt{(i)(j+1)}c_{i-1j+1klns} \\
&\quad - \sqrt{(s-n-k+1)(s+n-l)}c_{ijkln-1s} - \sqrt{(k+1)(l)}c_{ijk+1l-1n-1s}) \\
&\quad |s-n-i+1\rangle_1|s-n-k\rangle_2|i\rangle_3|k\rangle_4 \\
&\quad |s+n-j-1\rangle_5|s+n-l\rangle_6|j\rangle_7|l\rangle_8
\end{aligned}$$

$$\begin{aligned}
& \langle (J_{-15} + J_{-37} - J_{+26} - J_{+48})(J_{+15} + J_{+37} - J_{-26} - J_{-48}) \rangle = 0 \\
& \implies |\sqrt{(s-n-i+1)(s+n-j)}c_{ijklns} + \sqrt{(i)(j+1)}c_{i-1j+1klns} \\
&\quad - \sqrt{(s-n-k+1)(s+n-l)}c_{ijkln-1s} - \sqrt{(k+1)(l)}c_{ijk+1l-1n-1s}|^2 = 0 \\
& \langle (J_{+15} + J_{+37} - J_{-26} - J_{-48})(J_{-15} + J_{-37} - J_{+26} - J_{+48}) \rangle = 0 \\
& \implies |\sqrt{(s-n-i)(s+n-j+1)}c_{ijklns} + \sqrt{(i+1)(j)}c_{i+1j-1klns} \\
&\quad - \sqrt{(s-n-k)(s+n-l+1)}c_{ijkln+1s} - \sqrt{(k)(l+1)}c_{ijk-1l+1n+1s}|^2 = 0
\end{aligned}$$

Therefore we have 2 conditions -

$$\begin{aligned}
& |\sqrt{(s-n-i)(s+n-j+1)}c_{ijklns} + \sqrt{(i+1)(j)}c_{i+1j-1klns} \\
&\quad - \sqrt{(s-n-k)(s+n-l+1)}c_{ijkln+1s} - \sqrt{(k)(l+1)}c_{ijk-1l+1n+1s}|^2 = 0
\end{aligned} \tag{A.6}$$

$$\begin{aligned}
& |\sqrt{(s-n-i+1)(s+n-j)}c_{ijklns} + \sqrt{(i)(j+1)}c_{i-1j+1klns} \\
&\quad - \sqrt{(s-n-k+1)(s+n-l)}c_{ijkln-1s} - \sqrt{(k+1)(l)}c_{ijk+1l-1n-1s}|^2 = 0
\end{aligned} \tag{A.7}$$

Now that is final recurrence relation that can be derived and together with the definition of ψ and c_{ijklns} , defines the state uniquely. Notice that in both the

conditions, $s, i+j$ and $k+l$ stay constant in all the coefficients in the expression. We can see that the 4 total spins are $s_{15} = s - \frac{i+j}{2}$, $s_{26} = s - \frac{k+l}{2}$, $s_{37} = \frac{i+k}{2}$, $s_{48} = \frac{k+l}{2}$. Therefore both conditions give us a way to relate the various coefficients of a fixed set of 4 spins. This relates to the idea that J_0 commutes with J_x . If we consider J_y , we can easily check that the expansion will get the same two relations. That relates to the fact that J_x and J_y do not commute and are not independent relations. Thus we can now derive the 4 Qbit state i.e $i+j=1, k+l=1, s=1$. There are 12 possible choices for the set of parameters $\{i, j, k, l, n, s\}$ constrained by $\{i + j = 1, k + l = 1, n = [-s, s], s = 1\}$. But only the following 6 terms correspond to physical states.

$$c_{101001}, c_{011001}, c_{100101}, c_{010101}, c_{010111}, c_{1010-11}$$

The other 6 coefficients belong to unphysical (negative photon number) states and our relations hopefully will not include them.

$$c_{101011}, c_{011011}, c_{100111}, c_{0110-11}, c_{1001-11}, c_{0101-11} \quad (\text{A.8})$$

The other 10 possibilities of arranging 4 Qbits cannot be created in the pairwise generation scheme outlined above. Then applying the two conditions we can deduce the relations between these 12 coefficients.

$$\begin{aligned} c_{100111} &= 0; & c_{100111} &= 0; & c_{101011} &= 0; & c_{011001} + c_{101001} - c_{010111} &= 0; \\ c_{101011} &= 0; & c_{100111} &= 0; & c_{100111} &= 0; & c_{010101} + c_{100101} - c_{010111} &= 0; \\ c_{1001-11} &= 0; & c_{1001-11} &= 0; & c_{0110-11} &= 0; & c_{1010-11} - c_{011001} - c_{010101} &= 0; \\ c_{0110-11} &= 0; & c_{011011} &= 0; & c_{011011} &= 0; & c_{1010-11} - c_{101001} - c_{100101} &= 0; \\ c_{100101} + c_{010101} - c_{1010-11} &= 0; & c_{101001} + c_{011001} - c_{1010-11} &= 0; \\ c_{010111} - c_{100101} - c_{101001} &= 0; & c_{010111} - c_{011001} - c_{010101} &= 0; \\ c_{0110-11} &= 0; & c_{0110-11} &= 0; & c_{0101-11} &= 0; & c_{0101-11} &= 0. \end{aligned}$$

Therefore all the non-physical coefficients are zero and the 6 'good' coefficients are related by -

$$\begin{aligned}
c_{010111} - c_{100101} - c_{101001} &= 0; & c_{010111} - c_{011001} - c_{010101} &= 0; \\
c_{100101} + c_{010101} - c_{1010-11} &= 0; & c_{101001} + c_{011001} - c_{1010-11} &= 0; \\
c_{1010-11} - c_{101001} - c_{100101} &= 0; & c_{010101} + c_{100101} - c_{010111} &= 0; \\
c_{1010-11} - c_{011001} - c_{010101} &= 0; & c_{011001} + c_{101001} - c_{010111} &= 0; \\
\implies c_{100101} = c_{011001} = x & & & \text{(A.9)}
\end{aligned}$$

$$c_{101001} = c_{010101} = y \quad \text{(A.10)}$$

$$c_{1010-11} = c_{010111} = x + y \quad \text{(A.11)}$$

Now that we have some relations between the various coefficients, we can write down the state we have obtained in the photon number basis as -

$$\begin{aligned}
|\psi\rangle(s=1, i+j=1, k+l=1) &= a(|0\rangle_1|1\rangle_2|1\rangle_3|0\rangle_4|1\rangle_5|0\rangle_6|0\rangle_7|1\rangle_8 \\
&\quad + |1\rangle_1|0\rangle_2|0\rangle_3|1\rangle_4|0\rangle_5|1\rangle_6|1\rangle_7|0\rangle_8) \\
&\quad + b(|0\rangle_1|0\rangle_2|1\rangle_3|1\rangle_4|1\rangle_5|1\rangle_6|0\rangle_7|0\rangle_8 \\
&\quad + |1\rangle_1|1\rangle_2|0\rangle_3|0\rangle_4|0\rangle_5|0\rangle_6|1\rangle_7|1\rangle_8) \\
&\quad + (a+b)(|1\rangle_1|1\rangle_2|1\rangle_3|1\rangle_4|0\rangle_5|0\rangle_6|0\rangle_7|0\rangle_8 \\
&\quad + |0\rangle_1|0\rangle_2|0\rangle_3|0\rangle_4|1\rangle_5|1\rangle_6|1\rangle_7|1\rangle_8) \quad \text{(A.12)}
\end{aligned}$$

Applying a phase shift on mode 6 and 8 as prescribed above, we get -

$$\begin{aligned}
|\psi\rangle(s=1, i+j=1, k+l=1) &= a(|0\rangle_1|1\rangle_2|1\rangle_3|0\rangle_4|1\rangle_5|0\rangle_6|0\rangle_7|1\rangle_8 \\
&\quad + |1\rangle_1|0\rangle_2|0\rangle_3|1\rangle_4|0\rangle_5|1\rangle_6|1\rangle_7|0\rangle_8) \\
&\quad + b(|0\rangle_1|0\rangle_2|1\rangle_3|1\rangle_4|1\rangle_5|1\rangle_6|0\rangle_7|0\rangle_8 \\
&\quad + |1\rangle_1|1\rangle_2|0\rangle_3|0\rangle_4|0\rangle_5|0\rangle_6|1\rangle_7|1\rangle_8) \\
&\quad - (a+b)(|1\rangle_1|1\rangle_2|1\rangle_3|1\rangle_4|0\rangle_5|0\rangle_6|0\rangle_7|0\rangle_8 \\
&\quad + |0\rangle_1|0\rangle_2|0\rangle_3|0\rangle_4|1\rangle_5|1\rangle_6|1\rangle_7|1\rangle_8) \quad \text{(A.13)}
\end{aligned}$$

Rewriting the above state as 4 spins rather than 8 optical modes, where $|0\rangle|1\rangle \implies |\uparrow\rangle$, and $|1\rangle|0\rangle \implies |\downarrow\rangle$ we get -

$$\begin{aligned}
|\psi\rangle &= a(|\uparrow\rangle_{15}|\downarrow\rangle_{26}|\downarrow\rangle_{37}|\uparrow\rangle_{48} + |\downarrow\rangle_{15}|\uparrow\rangle_{26}|\uparrow\rangle_{37}|\downarrow\rangle_{48}) \\
&\quad + b(|\uparrow\rangle_{15}|\uparrow\rangle_{26}|\downarrow\rangle_{37}|\downarrow\rangle_{48} + |\downarrow\rangle_{15}|\downarrow\rangle_{26}|\uparrow\rangle_{37}|\uparrow\rangle_{48}) \\
&\quad - (a+b)(|\downarrow\rangle_{15}|\downarrow\rangle_{26}|\downarrow\rangle_{37}|\downarrow\rangle_{48} + |\uparrow\rangle_{15}|\uparrow\rangle_{26}|\uparrow\rangle_{37}|\uparrow\rangle_{48})
\end{aligned} \tag{A.14}$$

Now flipping 2 spins by considering spins 62 and 84, we get -

$$\begin{aligned}
|\psi\rangle &= a(|\uparrow\rangle_{15}|\uparrow\rangle_{62}|\downarrow\rangle_{37}|\downarrow\rangle_{84} + |\downarrow\rangle_{15}|\downarrow\rangle_{62}|\uparrow\rangle_{37}|\uparrow\rangle_{84}) \\
&\quad + b(|\uparrow\rangle_{15}|\downarrow\rangle_{62}|\downarrow\rangle_{37}|\uparrow\rangle_{84} + |\downarrow\rangle_{15}|\uparrow\rangle_{62}|\uparrow\rangle_{37}|\downarrow\rangle_{84}) \\
&\quad - (a+b)(|\uparrow\rangle_{15}|\downarrow\rangle_{62}|\uparrow\rangle_{37}|\downarrow\rangle_{84} + |\downarrow\rangle_{15}|\uparrow\rangle_{62}|\downarrow\rangle_{37}|\uparrow\rangle_{84})
\end{aligned} \tag{A.15}$$

Finally compare this to the general zero spin state derived through intuition -

$$\begin{aligned}
|\psi\rangle &= \frac{y-x}{2}(|\uparrow\rangle_1|\downarrow\rangle_2|\uparrow\rangle_3|\downarrow\rangle_4 + |\downarrow\rangle_1|\uparrow\rangle_2|\downarrow\rangle_3|\uparrow\rangle_4) \\
&\quad + x(|\uparrow\rangle_1|\uparrow\rangle_2|\downarrow\rangle_3|\downarrow\rangle_4 + |\downarrow\rangle_1|\downarrow\rangle_2|\uparrow\rangle_3|\uparrow\rangle_4) \\
&\quad - \frac{y+x}{2}(|\uparrow\rangle_1|\downarrow\rangle_2|\downarrow\rangle_3|\uparrow\rangle_4 + |\downarrow\rangle_1|\uparrow\rangle_2|\uparrow\rangle_3|\downarrow\rangle_4) \\
\implies x &= a; \frac{y-x}{2} = -(a+b); -\frac{y+x}{2} = b \\
\implies x &= a; y = -a - 2b
\end{aligned} \tag{A.16}$$

is a valid solution. Since both x and y are completely arbitrary coefficients and this state violates bell inequality for all non zero x and y, the above results are valid for any state i.e any values of a and b. Therefore, our elegant derivation was infact correct and a rigorous derivation yields the same state. This is also the most general singlet state with 4 Qbits. It contains within its locus all possible pairings of spins and also all possible ways ($|0,0\rangle \otimes |0,0\rangle$ and $\sum |1,m\rangle|1,-m\rangle$) of making a total spin-0 state with 4 Qbits.

Appendix B

Quantum Computing with Schwinger Spins

Our attempts to write multimode squeezed states yielded some interesting results. On the one hand, there is multipartite spin entanglement to be found in such states. On the other hand, it seems to be hard to make other states besides total spin zero states, for example cluster states which may be useful for measurement based quantum computing [50, 72, 52].

To go towards quantum computing with such an architecture, we need to explore two aspects,

- A general framework is needed to describe optics-spins correspondence for arbitrary initial states, arbitrary Hamiltonians and measurements.
- A theory and experimental proposal for quantum computing and quantum error correction using arbitrary spins rather than spin 1/2.

B.1 General optics-spins framework

We did not attempt to formulate such a framework. In our analysis, we only consider initial vacuum states, a few multimode squeezing Hamiltonians and photon number measurements with beamsplitters. Our collaborator Nick Menicucci and his student Natasha Gabay also extended it [73] to one large multimode squeezed

state that was experimentally demonstrated in the lab recently by our group [71]. However we have a couple of educated guesses on future directions for research in this field. Spin operators belong to the $SU(2)$ group, where the operators preserve the norm of the vector. For spins this means that $SU(2)$ operations preserve the total spin, which as we have seen means preserving total photon number for Schwinger spins. However the multimode squeezing transformations we use to create photon number correlations does not preserve photon number. They instead preserve photon number difference putting them in the $SU(1,1)$ group. Therefore we expect that a general framework to describe the behaviour of spin operators under squeezing transformations would make use of the $Sp(4)$ group which contains both $SU(2)$ and $SU(1,1)$ groups. Considerable theoretical work has been done on the symplectic group and its application on optics [66, 74, 67, 47] making this a promising direction of research.

The goal of this analysis would be to extract a recipe for creating any arbitrary multipartite spin state using optical systems and optical operations. Using group theoretical methods perhaps a small set of optical states and operations could be identified as constituting a "universal" set, i.e. a set of states and operations that can generate any arbitrary spin state. If such a "universal" set is not possible, then it would be useful to find the set of all multipartite spin states that can be simulated using optical systems.

B.2 Quantum Computing with Spins

While it is clear that multimode squeezed states can be used to simulate some spin systems, it is not clear if this is useful for quantum computing.

Qbits have long been the architecture of choice for quantum computing research, both theoretical and experimental. A major breakthrough in Qbit quantum computing is the development of stabilizer formalism [50]. For Qbits it can be demonstrated that universal quantum computing can be performed using just the Pauli operators X and Z and the two Qbit gate $C-X$ and the stabilizer formalism can be used to do all this in fault-tolerant manner. Experimental demonstrations of quantum computing and error correction with Qbits is an area of active research.

Many alternate architectures for quantum computing have been suggested. Continuous variables, Qdits, spins are some of them. As mentioned before, continuous

variable quantum computing using optical multimode squeezed states has the advantage of being easy to generate in large scale. However this architecture suffers from not being easy to error-correct, despite the recent result showing that error correction is possible below a certain error threshold [8].

Quantum computing with spins larger than Qbits is an interesting conundrum. One would expect that the elegance of Qbit quantum computing with spin-1/2 would carry over to larger spins. The good news is that Qdits do lend themselves to the stabilizer formalism allowing for error correction. However the bad news is that the Qdit Pauli operators X and Z can not be defined using spin x and spin z operator like in the Qbit case. We found many publications that attempt to define the Qdit Pauli operators using spins as Qdits, the results can be summarized thus

- The d-dimensional Pauli group requires that two operators X and Z and a basis $|s\rangle$ where $s \in \{0, d\}$ to behave such that -
 - $|s\rangle$ is an eigenstate of Z with unique eigenvalues $(-1)^{s/d}$.
 - X is a flip operator, so that $X|s\rangle = |s+1 \bmod d\rangle$.
 - Using the above we get

$$XZ = \omega ZX, \tag{B.1}$$

where $\omega = (-1)^{\frac{1}{d}}$.

- X and Z are unitary and Hermitian. $|\uparrow\rangle, |\downarrow\rangle$ are eigenstates of Z with eigenvalue 1,-1 respectively and $|+\rangle = |\uparrow\rangle + |\downarrow\rangle, |-\rangle = |\uparrow\rangle - |\downarrow\rangle$ are eigenstates of X with eigenvalue 1,-1 respectively.
- For $d > 1/2$, X and Z are unitary, but not Hermitian operation. This means that X and Z are not directly measurable quantities. $|s\rangle$ is the eigenstate of Z with eigenvalue ω^s and $|v\rangle = \sum_{s=0}^d \omega^{vs} |s\rangle$ is the eigenstate of X with eigenvalue ω^v where $s, v \in \{0, d-1\}$.

With just this much information we can construct the operators and states for any system that we want to use as Qdits. So lets take spins.

Clearly, for spin-1/2 Qbits, the Pauli operators X and Z correspond to the exponentiated spin operators σ_x and σ_z . Now we can do all Pauli things (thus all stabilizer things) etc with just spin operations and states so all is well.

To use spin $j = (d - 1)/2$ states as Qdits, we now take states $|s\rangle = |j, s - j\rangle$. These are eigenstates of J_z and Z . Hence even though Z is not Hermitian, J_z is and can be substituted for Z . However the X eigenstate is $|v\rangle = \sum_{s=0}^d \omega^{vs} |j, s - j\rangle$. This is not an eigenstate of J_x for $d > 1/2$. Therefore X operations for $d > 1/2$ cannot be done using spin operations.

Q. If not spin operators then what?

A. The state $|v\rangle$ is actually the spin phase state described by A.Vourdas in [74].

Vourdas defines a set of operators $\theta_x, \theta_y, \theta_z, \theta_0$ representing a "dual" representation [74] for spins than the normal J_x, J_y, J_z, J_0 representation.

$$\theta_z |j, t_z\rangle = v_z |j, v_z\rangle \quad (\text{B.2})$$

$$\theta_+ |j, t_z\rangle = \sqrt{j(j+1) - n(n+1)} |j, v_z + 1\rangle \quad (\text{B.3})$$

$$\theta_- |j, t_z\rangle = \sqrt{j(j+1) - n(n-1)} |j, v_z - 1\rangle \quad (\text{B.4})$$

$$\theta_0 |j, t_z\rangle = j |j, v_z\rangle \quad (\text{B.5})$$

The two representations can be related by -

$$|v\rangle = |j, v_z\rangle = \sum_{m=-j}^m e^{\frac{2\pi i}{j+1} m_z v_z} |j, m_z\rangle. \quad (\text{B.6})$$

Relating these states to the Qdit eigenstates we get,

$$|j, v_z\rangle = \sum_{s=0}^{d-1} (-1)^{\frac{(s-j)v}{d}} |s\rangle, \quad (\text{B.7})$$

$$= (-1)^{-jv/d} \sum_{s=0}^{d-1} (-1)^{\frac{sv}{d}} |s\rangle = (-1)^{-jv/d} |v\rangle. \quad (\text{B.8})$$

This we recognize is exactly the Qdit X eigenstate upto a global phase state. Therefore the X measurements can be replaced by θ_z measurements as they have a one-to-one correspondence for states in their eigenbasis.

Unfortunately while this, in theory, seems like a good idea, in practice the θ operators are beyond the scope of what is currently possible in the lab. No method of measuring them on actual spins has been demonstrated.

Q. What about our optical spins? A. So measuring spin phase is not known for actual spins, what about our simulated spins? Might optical spins allow us to

measure the spin phase states.

As it turns out the spin phase operators can be written as optical relative phase eigenstate measurements. These can also be defined mathematically but are hard to measure.

Writing the spin phase eigenstate in terms of optical states (for simplicity we take $v_z = 0$), we get -

$$|j, v_z = 0\rangle = \sum_{m_z=-j}^j |j, m_z\rangle \quad (\text{B.9})$$

$$= \sum_{n_1=0}^{2j} |n_1\rangle |n_2 = 2j - n_1\rangle \quad (\text{B.10})$$

Now say we evolve this state under a phase shift on both mode a and b.

$$U |j, 0\rangle = \sum_{n_1=0}^{2j} e^{in_1\theta_1} e^{in_2\theta_2} |n_1\rangle |n_2 = 2j - n_1\rangle \quad (\text{B.11})$$

$$= e^{i(n_1+n_2)(\theta_1+\theta_2)} \sum_{n_1=0}^{2j} e^{i(n_1-n_2)(\theta_1-\theta_2)} |n_1\rangle |n_2 = 2j - n_1\rangle \quad (\text{B.12})$$

$$= e^{2ij(\theta_1+\theta_2)} \sum_{m_z=-j}^j e^{2im_z(\theta_1-\theta_2)} |j, m_z\rangle \quad (\text{B.13})$$

$$= e^{2ij(\theta_1+\theta_2)} |j, v_z = \theta_1 - \theta_2\rangle \quad (\text{B.14})$$

That is a very interesting result. This means that if we wanted to implement an X operation, all we have to do is implement a relative phase shift $\theta_1 - \theta_2 = \pi/(d+1)$. This actually is, in principle, not that difficult. Especially if the two modes are chosen with different frequencies, then simply free evolution for a specific time can implement X. Of course, in practice, the required precision of control of optical elements and distance is hard, but that is an engineering problem.

However, creating an X eigenstate or making an X measurement (which can be considered equivalent problems) is more difficult even in principle. To measure X, we have to measure the relative phase between the two modes. However this is not the (classical) phase between two fields. Instead we are talking of the quantized phase of the Fock state. The quantized phase measurement has been the subject of much theoretical and experimental research [75, 76, 77, 78, 79]. To the best of

my knowledge no method exists that can reliably make a single shot, deterministic measurement of the relative phase operator.

As such, the feasibility of this measurement is a major obstacle for quantum computing with spins larger than $1/2$.

B.3 Error Correction with Spin operators

So we know that Pauli operators for Qdits correspond to phase measurements and phase eigenstates, which are extremely hard to perform/create. So the natural question to ask is if these Pauli operators are required at all. There are two important reasons why we use the Pauli group - 1. It can be shown that the Pauli group is a universal gate set for single Qbits. With the addition of a two mode entangling gate such as Ctrl-X, we get a universal gate set for any number of Qbits. 2. The stabilizer formalism and its use in error correction has been elucidated using Pauli group operations.

In principle there could be ways of achieving both the above conditions using, say, spin operations and measurements. However no such protocol is currently known.

Appendix C

Programming and Data Analysis

C.1 ON/OFF script

```
JumpTTL = 5.0;
ShutterTTL = 5.0;
v1=ShutterTTL;
v2=JumpTTL;

%4 aux channels being used
%Channel 1 -> shutter in front of laser, that lets \\  
seed/lockingbeam thru
%Ch 2 -> Locking TTL for the vescent modules
%Ch3 -> shutter in front of the tes heralding beam
%ch4 -> trigger signal sent directly to alazar.
i=1;
pause(5);
reps=100;
timers=zeros(3,reps);
tic
while i<10000
    %timers(1,i+1)=toc; %zero clocks here

    %Trigger off, not taking data
    v4 = 1*mod(i+1,2);
```

```
str=sprintf('AUXV %d, %d',4,v4);
fprintf(srlia,str);

%Close TES Shutter
v3 = 5*mod(i+1,2);
str=sprintf('AUXV %d, %d',3,v3);
fprintf(srlia,str);

%Open Locking Shutter
v1 = 5*mod(i,2);
str=sprintf('AUXV %d, %d',1,v1);
fprintf(srlia,str);

%timers(2,i+1)=toc; %takes roughly 3-4 msec from zero
%Lock on
JumpTTL=5*mod(i+1,2);
v2=JumpTTL;
str=sprintf('AUXV %d, %d',2,v2);
fprintf(srlia,str);

%timers(3,i+1)=toc; %takes 6-7 msec from zero
%Hold lock for 0.25 sec
i=i+1;
pause(0.20)

%timers(2,i+1)=toc;
%Lock off
JumpTTL=5*mod(i+1,2);
v2=JumpTTL;
str=sprintf('AUXV %d, %d',2,v2);
fprintf(srlia,str);

%timers(1,i+1)=toc;
%Close Locking Shutter and pause for 100 msec for
%tes to come back to life
ShutterTTL = 5*mod(i,2);
```

```
v1 = ShutterTTL;
str=sprintf('AUXV %d, %d',1,v1);
fprintf(srlia,str);
pause(0.1)

%Open TES Shutter and take data
v3 = 5*mod(i+1,2);
str=sprintf('AUXV %d, %d',3,v3);
fprintf(srlia,str);

%Trigger on, taking data
v4 = 1*mod(i+1,2);
str=sprintf('AUXV %d, %d',4,v4);
fprintf(srlia,str);

%The following loop is just used because somehow the
%triggering was not removing some of the cases when
%the trigger was zero throughtout the length of buffer
%file. By forcing the trigger to turn on and off every
%0.2 seconds, every file will have a trigger event.
%It wastes some small amount of data, and should be
%removed if possible to solve the problem.
%But it is not a big deal since this is only for the
%dso, to get a visual approximation of the correlation,
%final measurement will use raw data.
    i=i+1;
    for j=1:5
        pause(.3)
        %Trigger off, nottaking data
        v4 = 1*mod(i+1,2);
        str=sprintf('AUXV %d, %d',4,v4);
        fprintf(srlia,str);
        %Trigger on, taking data
        v4 = 1*mod(i,2);
        str=sprintf('AUXV %d, %d',4,v4);
        fprintf(srlia,str);
```

```

    end

end

toc
ShutterTTL = 5;
v = ShutterTTL;
str=sprintf('AUXV %d, %d',1,v); %locking beam shutter open
fprintf(srlia,str);
str=sprintf('AUXV %d, %d',3,v); %tes shutter open
fprintf(srlia,str);
JumpTTL=0.0;
v=JumpTTL;
str=sprintf('AUXV %d, %d',2,v); %vescent locking on
fprintf(srlia,str);
str=sprintf('AUXV %d, %d',4,v); %trigger off
fprintf(srlia,str);

```

C.2 Tomography

Tomography in AnalyzeRealttime

```

if tomography
    chname = 'ABCD';
    if S.FIFO
        data3D = double(reshape(typecast(uint8(
            data.Value(1:numpts)), 'uint16'), S.numchannels2record,
            S.RecordLength, S.RecsPerChannelPerBuffer))-2^15;
    else
        data3D = double(reshape(typecast(uint8(
            data.Value(1:numpts)), 'uint16'), S.RecordLength,
            S.numchannels2record, S.RecsPerChannelPerBuffer))-2^15;
    end
    global Wigner Nsum

    numchan = 1;

```

```

data = data3D(1,:);
%%%%%%%%%%%%%%%%%%%%%%%%%%%%%%%%%%%%%%%%%%%%%%%%%%%%%%%%%%%%%%%%%%%%%%%%
load('photon_limits');
maxnumber=size(PB,2)-2;      %largest photon we calibrated upto.
Any larger photon will be counted as the maxnumber size
thresh = PB(1,:);
%   thresh(1)=400;           %threshold for single photons
%   thresh(2)=900;           %threshold for 2 photon peak
%   thresh(3)=1300;          %threshold for 3 photon peak
%   thresh(4)=1800;          %threshold for 3 photon peak
%%%%%%%%%%%%%%%%%%%%%%%%%%%%%%%%%%%%%%%%%%%%%%%%%%%%%%%%%%%%%%%%%%%%%%%%
numtosum=6.;                 %choose s.t highest point lies
%inside num2sum pts after first pt, but next photon lies outside
mat=(0:numtosum-1)';
L=length(data);
TimeBin = 6;                 %Time Bin
%%%%%%%%%%%%%%%%%%%%%%%%%%%%%%%%%%%%%%%%%%%%%%%%%%%%%%%%%%%%%%%%%%%%%%%%
%to set the mean of the noise to zero, kill all photons above
thresh then recenter plot.
noisethresh=-50;            %threshold for noise mean to be 0...
datai=data>noisethresh;
data=data-sum(data.*not(datai))/length(data.*not(datai));
%raise level to set avareage noise =0
%   data=data.*datai;        %only the photons peaks and high noise peaks
%remain in plot.
%%%%%%%%%%%%%%%%%%%%%%%%%%%%%%%%%%%%%%%%%%%%%%%%%%%%%%%%%%%%%%%%%%%%%%%%
%A NEW WAY OF CALCULATING PHoTON PEAKS, ONE THAT ALLOWS TIME BINS
%%%%%%%%%%%%%%%%%%%%%%%%%%%%%%%%%%%%%%%%%%%%%%%%%%%%%%%%%%%%%%%%%%%%%%%%
diffthresh=150;              %threshold to count a rising edge.
%%%%%%%%%%%%%%%%%%%%%%%%%%%%%%%%%%%%%%%%%%%%%%%%%%%%%%%%%%%%%%%%%%%%%%%%
%Trying out new algo for rising edge detection
%%%%%%%%%%%%%%%%%%%%%%%%%%%%%%%%%%%%%%%%%%%%%%%%%%%%%%%%%%%%%%%%%%%%%%%%
numdiff=ceil(S.SampleRate/1250000); %How many points constitute
%rising edge. counting 3 for 2e6 and 5 for 5e6
d=zeros(numdiff+1,length(data)-1);
d(1,:)=diff(data);

```



```

%make sure total number of points is divisible by time bin size
%%%%%%%%%%%%%%%%%%%%%%%%%%%%%%%%%%%%%%%%%%%%%%%%%%%%%%%%%%%%%%%%%%%%%%%%
if mod(length(DataFinal),TimeBin)~=0
    more = TimeBin-mod(length(DataFinal),TimeBin);
    DataFinal(end+(1:more))=zeros([1,more]);
end
%%%%%%%%%%%%%%%%%%%%%%%%%%%%%%%%%%%%%%%%%%%%%%%%%%%%%%%%%%%%%%%%%%%%%%%%
phxx=sum(reshape(DataFinal,TimeBin,[]),1);
%collapse total time into units of time bin size
size(phxx);
sum(phxx);
N=zeros(1,100);
for l=1:100
    N(l)=sum(phxx==(l-1));
end
Wig=-sum(diff(reshape(N,2,[])))/length(phxx);
% Parity operator from Banaszek paper
Nsum = Nsum + N;
sum(Nsum.*(0:99));
%sum(Nsum);
Wigner=[Wigner Wig];
end

MainTomo

Vin = 0.00; %starting voltage for the steps
Vfin = 4.000; %final voltage after all the steps

%varray = [0 0.01 0.04 0.09 0.16 0.25 0.36 0.49 0.64 0.81 1];
varray = 3*([0:0.05:1].^2);
points1 = 40.0; % number of steps in the scan between Vin and Vfin
points2 = 60.0; % number of steps in the amplitude scan with hwp
global Wigner;
Wfun=zeros(points1,points2);
volts = [[0;0] [0;1] [0;4] [0.4;7] [0.8;12.5] [1.2;21] [1.5;30]
[1.9;43] [2.3;57] [2.6;70] [3;86]];

```

```
varray = 0.075:0.075:3;
step1 = 1.0;
step2 = 1.0;
%volts=fliplr(volts);
%varray=fliplr(varray);
while step1 <= 1%points1
    %v1 = volts(1,step1);
    %v1=(3*(step1-8.5))/points1;
    v1=varray(step1);
    setvolt(srlia,1,v1);
    pause(2);
    while step2 < 2*points2
        v2 = Vfin - abs((Vfin-Vin)*((points2-step2)/points2));
        setvolt(srlia,2,v2);
        filename = strcat('C:\Users\pfister\Documents
        \Alazar_Data\Tom\Tomography29\Data\ ',
        num2str(step1),'-',num2str(step2),'.daq');
        filename = strcat('C:\Users\pfister\Documents
        \Alazar_Data\Tom\Tomography29\Data\0-',
        num2str(step2),'.daq');
        %pause(.05);
        if step2<=points2
            TomoMainAlazar();
            %pause(2)
            %Wfun(step1,step2)=Wigner;
            %pause(.01);
        else
            pause(.05);
        end
        step2 = step2 + 1;
    end
    pause(2)
    step1 = step1 + 1;
    step2 = 1;
end
```

Appendix D

Quantum optics in the time domain

D.1 Introduction

In this section, we consider the quantum theory of optical temporal phase and instantaneous frequency for slowly varying signals in the continuous time limit. The frequency domain field operators satisfy the bosonic commutation relation:

$$[\hat{a}_\nu, \hat{a}_{\nu'}^\dagger] = \delta(\nu - \nu') \quad (\text{D.1})$$

Time domain field operators can be defined as -

$$\hat{A}(t) = \int_{-B/2}^{B/2} d\nu \hat{a}_\nu \exp(-2\pi i \nu t) \quad (\text{D.2})$$

Here, ν, ν' represent the frequencies $\nu_0 + \nu, \nu_0 + \nu'$. The transform has been shifted gives us a range of frequencies centered at zero such that $|\nu| < B/2$ and B is the bandwidth of the optical mode in question. This is only a valid procedure when assuming a slowly varying envelope approximation, i.e. $B/2 \ll \nu_0$. This is not a bad assumption since most frequencies in lab are in 100 THz range while the bandwidth in the experiments is usually in the 100 GHz range.

Then we can say,

$$\begin{aligned}
[\hat{A}_t, \hat{A}_{t'}^\dagger] &= \int_{B/2}^{B/2} \int_{B/2}^{B/2} d\nu d\nu' \hat{a}_\nu \hat{a}_{\nu'}^\dagger \exp(2\pi i(\nu t - \nu' t')) \\
&\quad - \int_{B/2}^{B/2} \int_{B/2}^{B/2} d\nu d\nu' \hat{a}_{\nu'}^\dagger \hat{a}_\nu \exp(2\pi i(\nu t - \nu' t')) \\
&= \int_{B/2}^{B/2} \int_{B/2}^{B/2} d\nu d\nu' \delta(\nu - \nu') \exp(2\pi i(\nu t - \nu' t')) \\
&\quad + \int_{B/2}^{B/2} \int_{B/2}^{B/2} d\nu d\nu' \hat{a}_{\nu'}^\dagger \hat{a}_\nu (\exp(2\pi i(\nu t - \nu' t')) - \exp(2\pi i(\nu t - \nu' t'))) \\
&= B \text{sinc}(\pi B(t - t'))
\end{aligned} \tag{D.3}$$

Therefore the annihilation and creation operators at two arbitrary different times are not orthogonal to each other in general. If we now discretize time into packets separated by $\delta t = 1/B$, so that $t_j = t_0 + j\delta t$ then,

$$[\hat{A}_{t_j}, \hat{A}_{t'_k}^\dagger] = B\delta_{jk} \tag{D.4}$$

Renormalizing with \sqrt{B} , we get the complete description of a temporal mode operator as a superposition of all time samples

$$\begin{aligned}
\hat{A}_t &= \sqrt{B} \sum_{j=-\infty}^{\infty} \hat{a}_j \text{sinc}(\pi B(t - t_j)) = \sum_{j=-\infty}^{\infty} \hat{A}_{t_j} \text{sinc}(\pi B(t - t_j)) \\
\hat{a}_\nu &= \frac{1}{\sqrt{B}} \sum_{j=-\infty}^{\infty} \hat{a}_j \exp(2\pi i\nu t_j) \quad \text{for } \nu < B/2
\end{aligned}$$

\hat{A}_t can be considered the annihilation operator at time t in the time domain.

As is clear from the above expansion, when $B \rightarrow 0$, or the light is monochromatic, A_t becomes a equi-probable summation over all time packets and the width of the packets δt also tends to infinity. So there is effectively only 1 time packet from $-\infty$ to ∞ .

As B becomes non-zero, A_t is a superposition of individual time packet operators a_j distributed in a sinc envelope. Therefore a measurement at time t , could have collapsed into one of the orthogonal packets t_j with a probability governed by the sinc envelope centered at that t_j . Conversely it means that if we measure light of bandwidth B at time t , then the orthogonal time state to that is at time $t + n\delta t$ for all non-zero integers n . So, in principle, to measure a state perfectly in the time domain we should measure time packets at every δt time for all time. In practice,

of course, the temporal envelope of a mode will be finite.

A fundamental point to recognize here is that the *sinc* function is the fourier transform of a square function and hence a square bandwidth gives us *sinc* temporal pulse shapes. We can substitute arbitrary bandwidth shapes and get the corresponding fourier transform as the shape of the time envelope. In general all pulse shapes have to be able to approximated as delta function in the limit of small bandwidth so many of the results below can be general guidelines for any waveform. We chose the square bandwidth because it was the choice in the reference [80]. A Gaussian bandwidth would have been the better choice, both in relation to our experiment and ease of calculation since the Fourier transform of a Gaussian is another Gaussian.

D.1.1 Coherent states in time

To describe a coherent state in the time domain, we have -

$$\begin{aligned}
\hat{A}_t|\alpha_t\rangle &= \alpha_t|\alpha_t\rangle \\
&= \sqrt{B} \sum_{j=-\infty}^{\infty} \hat{a}_j \text{sinc}(\pi B(t - t_j))|\alpha_t\rangle \\
\implies |\alpha_t\rangle &= \bigotimes_j |\alpha_j\rangle, \quad \alpha_t = \sqrt{B} \sum_{j=-\infty}^{\infty} \alpha_j \text{sinc}(\pi B(t - t_j)) \quad (\text{D.5}) \\
\implies |\alpha_t\rangle &= \prod_j \exp[\alpha_j \hat{a}_j^\dagger - \alpha_j^* \hat{a}_j]|0\rangle \\
&= \exp\left[\sum_j \left(-\frac{1}{2}|\alpha_j|^2 + \alpha_j \hat{a}_j^\dagger\right)\right]|0\rangle
\end{aligned}$$

When describing a coherent state of finite bandwidth, such as in a pulsed laser, we can speak of a coherent state in time. A coherent state at time t, is a tensor product of coherent states at each of the orthogonal time packets, where the displacement of each packet state is governed by the *sinc* distribution of the packet from the time t.

Therefore the time domain displacement operator is -

$$|\alpha_t\rangle = \exp\left[-\frac{1}{2} \int_{-\infty}^{\infty} dt |\alpha_t|^2 + \int_{-\infty}^{\infty} dt \alpha_t \hat{A}_t^\dagger\right]|0\rangle, \quad \langle N \rangle = \int_{-\infty}^{\infty} dt |\alpha_t|^2 \quad (\text{D.6})$$

Reader Note:

Up until this point all the information presented has been directly from the reference [80]. The calculations from here on are mine. These are unpublished and as such were only used not as results themselves but to gain an understanding of our experiments.

Also the notation used here can be seen to be slightly different from the reference. Tsang, Shapiro use $A(t)$ and we use A_t primarily to avoid confusion with the $a(t)$ that we use common to denote time evolution of frequency domain annihilation operators.

D.2 Time evolution in the time domain

We have to find what time evolution does to the mode operator.

$$\begin{aligned}\hat{A}_t &= \int_{-B/2}^{B/2} d\nu \hat{a}_\nu \exp(-2\pi i\nu t), \quad \text{and} \\ \hat{A}_{t+t'} &= \int_{-B/2}^{B/2} d\nu \hat{a}_\nu \exp(-2\pi i\nu(t+t'))\end{aligned}\tag{D.7}$$

Therefore when time states evolve they don't get additional phase terms multiplied. The time signature is the phase signature.

D.3 Interesting states in the time domain

D.3.1 Spontaneous Parametric Down-Conversion (SPDC)

In the down-conversion process, we expect two photons to be created simultaneously, i.e at the same t_j , while their frequencies are only bounded by the bandwidth and energy conservation. Therefore B is defined as the bandwidth, in our case is 300GHz. A single SPDC generation hamiltonian can be described as,

$$H_\nu = i\chi\beta(\hat{a}_{1,\nu}^\dagger \hat{a}_{2,-\nu}^\dagger - c.c)\tag{D.8}$$

Summed over all such possible frequency pairs we get -

$$\begin{aligned}
H_{spdc} &= \int d\nu H_\nu = -i\chi\beta \int_{-B/2}^{B/2} d\nu (\hat{a}_{1,\nu} \cdot \hat{a}_{2,-\nu} - c.c) \\
H_{spdc} &= -i\chi\beta \left(\int_{-B/2}^{B/2} \frac{d\nu}{B} \sum_{i,j=-\infty}^{\infty} \hat{a}_{1i}\hat{a}_{2j} \exp(2\pi i\nu(t_i - t_j)) - c.c \right) \\
H_{spdc} &= -i\chi\beta \left(\sum_{i,j=-\infty}^{\infty} \hat{a}_{1i}\hat{a}_{2j} \text{sinc}(\pi B(t_i - t_j)) - c.c \right)
\end{aligned}$$

The difference t_i and t_j , is t_k and $\text{sinc}(t_k)$ will also be zero for all $k \neq 0$. Therefore $\hat{a}_{1\nu} \cdot \hat{a}_{2,-\nu} = \sum \hat{a}_{1j}\hat{a}_{2j}$; they are produced together or not at all.

$$\begin{aligned}
H_{spdc} &= \frac{-i\chi\beta}{B} \left(\sum_{j=-\infty}^{\infty} \hat{a}_{1j}\hat{a}_{2j} - c.c \right) = \sum_j H_j \\
\implies H_{spdc} &= -i\chi\beta \left(\int_{-\infty}^{\infty} dt (\hat{A}_{1,t}\hat{A}_{2,t} - c.c) \right) \tag{D.9}
\end{aligned}$$

All the above calculation is valid only if we assume the pump is a high power monochromatic continuous wave, meaning $b_j^\dagger = \beta$ for all j . Then the state after the Hamiltonian can be given by the propagator on vacuum-

$$\begin{aligned}
|\psi\rangle &= \exp(iH_{spdc}t_{int})|0\rangle \\
&= \bigotimes |\psi_j\rangle \tag{D.10}
\end{aligned}$$

where r is a familiar squeezing parameter, $r = \chi\beta t_{int}$ and j is the time quantum number.

I have used here that the t appearing in propagator e^{iHt} is time of interaction t_{int} denoting how long the Hamiltonian is turned on for, which in this case happens to be the time it takes for the pump to traverse the crystal. For the purpose of this calculation t_{int} has no relation and no bearing on the time variable or the time eigenstates in any way, and is just a constant affecting the squeezing parameter. One way t_{int} can affect the time domain calculation is if we take into account dispersion of the crystal and say that refractive index and hence t_{int} varies with ν . This is but neglected for now as the pump is assumed to be perfectly monochromatic. Incorporating this requires including a frequency dependent factor in χ and integrating over the pump bandwidth.

Another important consideration is whether t_{int} has an effect on the time domain

analysis due to the energy uncertainty relation and that changes the Hamiltonian to include the effects of the finite crystal. However most SPDC and down-conversion references ignore this effect, hence we will as well.

Therefore an SPDC output with a finite bandwidth can actually be considered as a train of SPDC pulses. Even though the emission could be random, we will get the complete information if our detection resolution is δt since we can decompose any arbitrary output into a basis of time pulses with separation δt where B is the bandwidth. In the SPDC case e.g $B = 300$ GHz, meaning the pulse separation is 3.33 picoseconds. If we make the bandwidth 1 GHz, then the separation is 1 nanosecond.

D.3.2 SPDC with a filter cavity

Now in this case the Hamiltonian is the same as in the SPDC case as derived above.

$$H_{spdc} = -i\chi\beta\left(\int_{-\infty}^{\infty} dt(\hat{A}_{1,t}\hat{A}_{2,t} - c.c)\right)$$

Now this state encounters the cavity, so first let us look at the effect of a filter cavity on a mode.

D.3.2.1 Effect of cavity on modes in time domain

The cavity can be treated as a double BS apparatus. Let the mode input to the cavity be $A_{t,in}$, the mode reflected back be $A_{t,r}$, the mode in the cavity be $A_{t,m1}, A_{t,m2}$ travelling along at the first mirror and against the input at the second mirror, respectively, and the mode outside be $A_{t,out}$. $B_{t,out}$ can be the vacuum mode outside the cavity and let the length of the cavity be L . As will be derived below, at a BS the operator in the time domain splits similar to the operator in the frequency domain, $\hat{A}_{1,t} \rightarrow \hat{A}_{1,t} + \hat{A}_{2,t}$. Therefore here, $\hat{A}_{t,m1} = \tau_1\hat{A}_{t,in} + \rho_1\hat{A}_{t-t_c,m2}e^{i\omega t_c}$, $\hat{A}_{t,r} = \rho_1\hat{A}_{t,in} - \tau_1\hat{A}_{t-t_c,m2}$. Again at the second BS, $\hat{A}_{t,out} = \tau_2\hat{A}_{t-t_c,m1} - \rho_2\hat{B}_{t,out}$, $\hat{A}_{t,m2} = \rho_2\hat{A}_{t-t_c,m1} + \tau_2\hat{B}_{t,out}$. Here $t_c = L/c$, L being the length of the cavity. Now we must find $\hat{A}_{t,m1}$ and $\hat{A}_{t,m2}$ which would allow us to solve for $\hat{A}_{t,out}$.
 $\hat{A}_{t,m2} = \rho_2\hat{A}_{t-t_c,m1} + \tau_2\hat{B}_{t,out}$.
 $\implies \hat{A}_{t,m1} = \tau_1\hat{A}_{t,in} + \rho_1\rho_2\hat{A}_{t-2t_c,m1} + \rho_1\tau_2\hat{B}_{t-t_c,out}$

$$\implies \hat{A}_{t,m1} = \sum_{n=0}^N (\rho_1 \rho_2)^n (\tau_1 \hat{A}_{t-2nt_c, in} + \rho_1 \tau_2 \hat{B}_{t-(2n+1)t_c, out}) + (\rho_1 \rho_2)^N \hat{A}_{t-2Nt_c, m1}$$

Now in the above expression if N gets very large, then asymptotically, the expression converges to be, $\hat{A}_{t,m1} = \sum_{n=0}^N (\rho_1 \rho_2)^n (\tau_1 \hat{A}_{t-2nt_c, in} + \rho_1 \tau_2 \hat{B}_{t-(2n+1)t_c, out})$. Now, $\hat{A}_{t, out} = \tau_2 \hat{A}_{t-t_c, m1} - \rho_2 \hat{B}_{t, out}$

$$\implies \hat{A}_{t, out} = \sum_{n=0}^N (\rho_1 \rho_2)^n (\tau_1 \tau_2 \hat{A}_{t-(2n+1)t_c, in} + \rho_1 \tau_2^2 \hat{B}_{t-(2n+2)t_c, out}) - \rho_2 \hat{B}_{t, out} \quad (\text{D.11})$$

We have thus derived A_{out} in terms of A_{in} and vacuum modes B .

Now all that is left is to decide the final shape of the output mode. For an intuitive idea, we can consider $A_{t, out}$ without the vacuum modes. We know that $A_t = \sum_j \alpha_j \text{sinc}(\pi B(t - t_j))$. Therefore

$$\begin{aligned} \hat{A}_{t, out} &= \tau_1 \tau_2 \sum_{n=0}^N (\rho_1 \rho_2)^n \sum_j \hat{\alpha}_{j, in} \text{sinc}(\pi B(t - 2nt_c - t_j)) \\ &= \tau_1 \tau_2 \sum_j \hat{\alpha}_{j, in} \sum_{n=0}^N (\rho_1 \rho_2)^n \text{sinc}(\pi B(t - t_j - 2nt_c)) \end{aligned}$$

Understandably, its a little hard to discern the output in an intuitive way from the above expression. The expression does not have a good simplification for $N \rightarrow \infty$. Fortunately its easy to see the behaviour of the expression as a function of the various parameters numerically. Firstly N does go to infinity, but the $\rho_1 \rho_2$ term which is always less than 1 ensures that larger N terms are less significant. The more interesting variables are the cavity reflectivity ρ , B and t_c . For $\rho = 1$, the expression is an infinite sum of equal sinc. If the round trip time $2t_c$ is short enough with respect to the width of the sinc bandwidth B , the sum would convert to a constant line. A constant line in t would be similar to a sinc with vanishing bandwidth, i.e a monochromatic beam. This is the effect we commonly think of a cavity having, i.e it selects a single frequency out of the input and allows it through. But for a long enough round trip time or short enough B , we would not have a constant line. In fact in the other extreme we will have a train of sinc pulses. This is the important insight that will come back later. For now we note that the cavity is not a single frequency filter. Its frequency spectrum is a comb, and hence its time spectrum is a train of pulses. The input frequency bandwidth and the cavity spectral linewidth and FSR together decide whether the output can

be treated as nearly monochromatic/temporally-constant light or a comb in both frequency and time.

For $\rho \rightarrow 0$, A_{out} is just the original A_{in} . For all ρ in between the two extremes we can numerically see that the sum turns from a symmetric sinc to a one sided pulse with maximum at $t = t_j$ and an elongated tail towards $t > t_j$. The greater the reflectivity, and thus the finesse of the cavity, the longer the length of the output pulse. Conversely we could say that higher the finesse, longer the time bin width, and hence smaller the bandwidth or the linewidth of the cavity.

Now we come back to look at what happens when we put SPDC into the cavity filter. Simply replace the mode with the new mode that we have derived.

$$\begin{aligned}\hat{A}_{t,out} &= \sum_{n=0}^N (\rho_1 \rho_2)^n (\tau_1 \tau_2 \hat{A}_{t-(2n+1)t_c, in} + \rho_1 \tau_2^2 \hat{B}_{t-(2n+2)t_c, out}) - \rho_2 \hat{B}_{t, out} \\ &= \sum_{m=0}^N c_m \hat{A}'_{t-mt_c}\end{aligned}\tag{D.12}$$

where $c_m = -\rho_2$ for $m = 0$, $(\rho_1 \rho_2)^{m/2} \tau_1 \tau_2$ for odd m and $(\rho_1 \rho_2)^{\frac{m-1}{2}} \rho_1 \tau_2^2$ for even m and $A = A$ for odd m and $A = B$ for even m .

$$\begin{aligned}H_{spdc} &= -i\chi\beta \left(\int_{-\infty}^{\infty} dt (\hat{A}_{1,t} \hat{A}_{2,t} - c.c) \right) \\ &= -i\chi\beta \left(\int_{-\infty}^{\infty} dt \left(\sum_{n=0}^N c_n \hat{A}'_{1,t-nt_c} \right) \left(\sum_{m=0}^N c_m \hat{A}'_{2,t-mt_c} \right) - c.c \right) \\ &= -i\chi\beta \sum_{n,m=0}^N c_n c_m \int_{-\infty}^{\infty} dt (\hat{A}_{1,t-mt_c} \hat{A}_{2,t-nt_c} - c.c) \\ &= -i\chi\beta \sum_{n,m=0}^N \frac{c_n c_m}{B} \int_{-\infty}^{\infty} dt \left(\sum_{i,j=0}^{\infty} \hat{\alpha}_{1,i} \hat{\alpha}_{2,j} \right. \\ &\quad \left. \text{sinc}(\pi B(t - mt_c - t_i)) \text{sinc}(\pi B(t - nt_c - t_j)) - c.c \right) \\ &= -i\chi\beta \sum_{n,m=0}^N c_n c_m \sum_{i,j=0}^{\infty} \left(\hat{\alpha}_{1,i} \hat{\alpha}_{2,j} \text{sinc}(\pi(j - i + (n - m) \frac{B}{2FSR})) \right) - c.c\end{aligned}$$

For the sake of convenience, we can assume that FSR is small enough that B/FSR is a large integer. Having it be large also brings sinc to look more and more like a delta function and the secondary peaks can be ignored and we can only look at

the central maxima of each sinc, i.e $i = j + (n - 2m)B/2FSR$. Therefore,

$$H_{filtered\,spdc} = -i\chi\beta \sum_{n,m=0}^N c_n c_m \sum_{j=0}^{\infty} (\hat{\alpha}_{1,j+(n-m)\frac{B}{2FSR}} \hat{\alpha}_{2,j} - c.c)$$

Its a complicated sum, perhaps we can get more insight when we do HOM and detection on it.

D.3.3 Hong-Ou-Mandel interference

Now to see what would happen if we interfere the two down-converted modes and analyze in the time domain. In the frequency domain, the BS would simply enact $\hat{a}_\nu \rightarrow \hat{a}_\nu + \hat{a}_\nu, \hat{a}_{-\nu} \rightarrow \hat{a}_{-\nu} - \hat{a}_{-\nu}$.

$$\begin{aligned} H_{HOM1} &= \frac{-i\chi\beta}{2} \left(\int_{-B/2}^{B/2} d\nu (\hat{a}_{1,\nu} + \hat{a}_{2,\nu})(\hat{a}_{1,-\nu} - \hat{a}_{2,-\nu}) dt - c.c \right) \\ H_{HOM1} &= \frac{-i\chi\beta}{2B} \left(\sum_j (\hat{a}_{1,j}\hat{a}_{1,j} + \hat{a}_{2,j}\hat{a}_{1,j} - \hat{a}_{1,j}\hat{a}_{2,j} - \hat{a}_{2,j}\hat{a}_{2,j}) - c.c \right) \\ &= \frac{-i\chi\beta}{2B} \left(\int_{-\infty}^{\infty} dt (\hat{A}_{1,t}\hat{A}_{1,t} - \hat{A}_{2,t}\hat{A}_{2,t} + \hat{A}_{1,t}\hat{A}_{2,t} - \hat{A}_{1,t}\hat{A}_{2,t} - c.c) \right) \\ H_{HOM1} &= \frac{-i\chi\beta}{2B} \left(\sum_j (\hat{a}_{1,j}\hat{a}_{1,j} - \hat{a}_{2,j}\hat{a}_{2,j}) - c.c \right) \\ &= \frac{-i\chi\beta}{2} \left(\int_{-\infty}^{\infty} dt (\hat{A}_{1t}\hat{A}_{1t} - \hat{A}_{2t}\hat{A}_{2t} - c.c) \right) \end{aligned} \quad (D.13)$$

Therefore, $\hat{A}_{1,t} \rightarrow \hat{A}_{1,t} + \hat{A}_{2,t}$ and $\hat{A}_{2,t} \rightarrow \hat{A}_{1,t} - \hat{A}_{2,t}$ and it seems fairly obvious that HOM is happening and there will be no coincidences. But the above simplification would require the paths to meet such that $\hat{A}_{1,t}$ interferes with $\hat{A}_{2,t}$. What if this is not true? So now consider the arbitrary time Hamiltonian where $\hat{a}_{1,\nu}$ and $\hat{a}_{2,-\nu}$ are interfered at a BS but in such a way that mode 2 has travelled an extra relative

time $t' = t + \Delta t$. Therefore now,

$$\begin{aligned}
H_{HOM2} &= \frac{-i\chi\beta}{2} \left(\int_{-B/2}^{B/2} d\nu (\hat{a}_{1,\nu} + \hat{a}_{2,\nu}) (\hat{a}_{1,-\nu} - \hat{a}_{2,-\nu}) \exp 2\pi i \nu \Delta t - c.c \right) \\
H_{HOM2} &= \frac{-i\chi\beta}{2B} \left(\sum_{i,j} (\hat{a}_{1,i} \hat{a}_{1,j} - \hat{a}_{2,i} \hat{a}_{2,j}) \text{sinc} \pi B (t_i - t_j + \Delta t) + c.c \right. \\
&\quad \left. + \int_{-B/2}^{B/2} d\nu (\hat{a}_{2,j} \hat{a}_{1,i} e^{2\pi i \nu (-t_i + t_j + \Delta t)} - \hat{a}_{1,i} \hat{a}_{2,j} e^{2\pi i \nu (t_i - t_j + \Delta t)}) - c.c \right) \\
H_{HOM2} &= \frac{-i\chi\beta}{2B} \sum_{i,j} \left((\hat{a}_{1,i} \hat{a}_{1,j} - \hat{a}_{2,i} \hat{a}_{2,j}) \text{sinc} \pi B (t_i - t_j + \Delta t) \right. \\
&\quad \left. + \hat{a}_{1,i} \hat{a}_{2,j} (\text{sinc} \pi B (-t_i + t_j + \Delta t) - \text{sinc} \pi B (t_i - t_j + \Delta t)) - c.c \right) \\
H_{HOM2} &= \frac{-i\chi\beta}{2} \int_{-\infty}^{\infty} dt (\hat{A}_{1,t'} \hat{A}_{1,t} - \hat{A}_{2,t'} \hat{A}_{2,t} + \hat{A}_{1,t} \hat{A}_{2,t'} - \hat{A}_{1,t'} \hat{A}_{2,t} - c.c) \quad (D.14)
\end{aligned}$$

Therefore, now $\hat{A}_{1,t'} \rightarrow \hat{A}_{1,t'} + \hat{A}_{2,t'}$ and $\hat{A}_{2,t} \rightarrow \hat{A}_{1,t} - \hat{A}_{2,t}$. From the above expression we can clearly see that if $\Delta t \neq 0$ for some k then we will have essentially all terms of the summation in the output, so we will have to find the matrix elements to see the time dependence and correlation. Finally we see what happens if we try HOM with a filtered SPDC.

$$H_{filtered\text{spdc}} = \frac{-i\chi\beta}{2} \sum_{n,m=0}^N c_n c_m \int_{-\infty}^{\infty} dt (\hat{A}_{1,t-mt_c} + \hat{A}_{2,t-mt_c}) (\hat{A}_{1,t-nt_c} - \hat{A}_{2,t-nt_c}) - c.c$$

This is even less obvious a result and we have to learn detection in the time domain now before we go any further.

D.4 Detection

Let us think what happens when we make a measurement. So far we have considered described states in the form $U|0\rangle$ and describing the propagator $U = \exp iHt_{int}$ describes the state completely. Measurements are essentially the operator matrix acting on these states. The operators that we can measure in the lab are the number operator, $\hat{a}^\dagger\hat{a}$ and \hat{P} and \hat{Q} . Therefore, measurement of operator O is equivalent to the finding the matrix element $\langle 0|U^\dagger\hat{O}U|0\rangle$. So to find the measurement result it suffices to find the evolution of the operator under the propagator.

An important point to note here is that when we measure P and Q using homodyne detection, we are picking a very sharp frequency line determined by the frequency of the local oscillator. So in principle we can assume the local oscillator is a monochromatic continuous wave and we are measuring \hat{P}_ν and \hat{Q}_ν . (We could also design our local oscillator to have a non-monochromatic bandwidth). However when we measure with the TES, we have bandwidth of measurement, and consequently the measurement has a finite time width given by the time resolution of the detector. Therefore the measurement is actually $\hat{D}_t^\dagger\hat{D}_t$, where I denote the time domain creation and annihilation operators of the detector by \hat{D}_t^\dagger and \hat{D}_t . However since the bandwidth B_d of detection is different from the bandwidth of creation, while we can still decompose D_t into time bin operators d_j , the duration of these time bins is distinct from the mode creation operator decomposition. Therefore it has to be carefully understood what the operator is.

So now we want to find matrix elements of the operator, i.e. calculate $U^\dagger\hat{O}U$. To do that we have find the relation between D_t and A_t . If we expand D_t in its time domain basis, we can get a decomposition into time bins just as before. However the bandwidth and hence the time bins are different now. To see their commutation relation we can fourier transform back to their frequency components which is more familiar territory.

$$a_\nu = \int_{-\infty}^{\infty} dt \hat{A}_t \exp 2\pi i \nu t$$

$$d_\nu = \int_{-\infty}^{\infty} dt \hat{D}_t \exp 2\pi i \nu t$$

Now in the frequency domain we know the relation is simply, $[\hat{d}_\nu, \hat{a}_{\nu'}^\dagger] = \delta(\nu - \nu')$ i.e for monochromatic light the detection measures exactly the optical mode.

Therefore we can find,

$$\begin{aligned}
[\hat{A}_t, \hat{D}_{t'}^\dagger] &= \int_{B_s/2}^{B_s/2} \int_{B_d/2}^{B_d/2} d\nu d\nu' \hat{a}_\nu \hat{d}_{\nu'}^\dagger \exp(2\pi i(\nu t - \nu' t')) \\
&\quad - \int_{B_s/2}^{B_s/2} \int_{B_d/2}^{B_d/2} d\nu d\nu' \hat{d}_{\nu'}^\dagger \hat{a}_\nu \exp(2\pi i(\nu t - \nu' t')) \\
&= \int_{B_s/2}^{B_s/2} \int_{B_d/2}^{B_d/2} d\nu d\nu' \delta(\nu - \nu') \exp(2\pi i(\nu t - \nu' t')) \\
&\quad + \int_{B_s/2}^{B_s/2} \int_{B_d/2}^{B_d/2} d\nu d\nu' \hat{d}_{\nu'}^\dagger \hat{a}_\nu (\exp(2\pi i(\nu t - \nu' t')) - \exp(2\pi i(\nu t - \nu' t'))) \\
&= B \text{sinc}(\pi B(t - t')) \tag{D.15}
\end{aligned}$$

where B is the $\min\{B_s, B_d\}$.

However $B_d \gg B_s$ is almost always true. That would mean that most detectors have vanishingly small δt time bins and hence very high time resolution. However that is also not true, the TES has terrible time resolution, $\sim 1\mu s$. The reason is that detectors, despite having large bandwidth and tiny theoretical time resolution, have their speed determined by the response time. The response time of a detector depends on machinery of the detector output, which will usually set the resolution of the detector a value much larger than the minimum theoretical time resolution set by the bandwidth. The resolution time ends up integrating the operator it measures over the response time of the detector, since all detection within this time are considered as one measurement. In the case of the TES, it is the response time that is 100 ns. Fortunately the TES has no dead time to take into consideration if we assume the input flux is low enough to not saturate the detector.

Therefore, finally we can write the number operator of a PNR detector as $N_t = D_t^\dagger D_t = \int_t^{t+T_d} dt A_t^\dagger A_t$, where T_d is the response time of the detector. Also the time bins are now decided by the shorter bandwidth which is simply B_s , and therefore the theoretical time bins will be simply $\delta t = 1/B_s$. However the actual measurement output will be in time bins of $\delta t = T_d$.

So now we are back to the finding the matrix elements, i.e. calculate $U^\dagger \hat{O} U$, where $U = \exp iHt_{int}$. From the Hadamard lemma we can see simply that -

$$\begin{aligned} & \exp(iHt_{int}) \hat{O} \exp(-iHt_{int}) \\ &= O + [iHt, O] + \frac{1}{2!} [iHt, [iHt, O]] + \frac{1}{3!} [iHt, [iHt, [iHt, O]]].. \end{aligned} \quad (D.16)$$

For a PNR detector, we have $\hat{O} = \int_t^{t+T_d} dt A_t^\dagger A_t$. Now to see how this detector model fares against various states.

D.4.1 Coherent State

Lets do it first for coherent state, where U is simply the displacement operator, $|\alpha_t\rangle = \exp[\int_{-\infty}^{\infty} dt(\alpha_t \hat{A}_t^\dagger - \alpha_t^* \hat{A}_t)]|0\rangle$.

$$\begin{aligned} [iHt_{int}, O] &= \left[\int_{-\infty}^{\infty} dt(\alpha_t \hat{A}_t^\dagger - \alpha_t^* \hat{A}_t), \int_t^{t+T_d} dt A_t^\dagger A_t \right] \\ &= \int_{-\infty}^{\infty} \int_{t_m}^{t_m+T_d} dt' dt (\alpha_{t'} \hat{A}_t^\dagger [\hat{A}_{t'}^\dagger, \hat{A}_t] - \alpha_{t'}^* [\hat{A}_{t'}, \hat{A}_t^\dagger] \hat{A}_t) \\ &= - \int_{-\infty}^{\infty} \int_{t_m}^{t_m+T_d} dt' dt (\alpha_{t'} \hat{A}_t^\dagger B \text{sinc} \pi B(t' - t) + c.c) \\ &= - \sum_{i,j} \int_{-\infty}^{\infty} \int_{t_m}^{t_m+T_d} dt' dt B^2 (\alpha_i \hat{a}_j^\dagger \text{sinc} \pi B(t' - t) \\ &\quad \times \text{sinc} \pi B(t' - t_i) \text{sinc} \pi B(t - t_j) + c.c) \\ &= - \sum_{i,j} \int_{t_m}^{t_m+T_d} dt B (\alpha_i \hat{a}_j^\dagger \text{sinc} \pi B(t - t_j) \text{sinc} \pi B(t - t_i) + c.c) \\ &= - \int_{t_m}^{t_m+T_d} dt (\alpha_t \hat{A}_t^\dagger + \alpha_t^* \hat{A}_t) \end{aligned}$$

No further simplification is possible, we can simply go ahead and find the second term of the series [D.16](#). Note the + sign that comes in front of c.c in the above

simplification due to the fact that $[\hat{a}, \hat{a}^\dagger] = -[\hat{a}^\dagger, \hat{a}]$.

$$\begin{aligned} [iHt_{int}, [iHt_{int}, O]] &= \left[\int_{-\infty}^{\infty} dt (\alpha_t \hat{A}_t^\dagger - \alpha_t^* \hat{A}_t), - \int_{t_m}^{t_m+T_d} dt (\alpha_t \hat{A}_t^\dagger + \alpha_t^* \hat{A}_t) \right] \\ &= \int_{-\infty}^{\infty} dt \int_{t_m}^{t_m+T_d} dt' \alpha_t \alpha_{t'}^* + \alpha_t^* \alpha_{t'} \\ &= 2 \int_{t_m}^{t_m+T_d} dt' |\alpha_{t'}|^2 \end{aligned}$$

This term being a numerical term and not an operator, will commute with H, and hence all the remaining terms of the series will be zero. Now our measurement result will now simply be the matrix element of the new operator given by D.16 with the vacuum state. Therefore $N_{t_m} = \langle 0 | \int_{t_m}^{t_m+T_d} dt (\hat{A}_t^\dagger \hat{A}_t + \alpha_t \hat{A}_t^\dagger + \alpha_t^* \hat{A}_t + \frac{1}{2} (2 \int_{t_m}^{t_m+T_d} dt' |\alpha_{t'}|^2)) | 0 \rangle$. It is easy to see that all except the last term will give zero and therefore the measurement result is in fact

$$\langle N \rangle = \int_{t_m}^{t_m+T_d} dt' |\alpha_{t'}|^2. \quad (\text{D.17})$$

If we were integrating over all time, essentially using a super slow detector to make a continuous wave measurement, then we get back $\int_{-\infty}^{\infty} dt' |\alpha_{t'}|^2 = \langle N \rangle$. (t_m is an arbitrary time for start of measurement and can be assumed to be any time without loss of generality). Therefore a slow detector will be a quasi-cw measurement and give us the average photon number measurements over multiple time bins and time statistics would not be discernible.

From all the above calculation we can use a couple of simple notes which will make our calculations easier.

$$\int_{-\infty}^{\infty} \hat{A}_t B \text{sinc}(\pi B(t - t')) dt = \hat{A}_{t'} \quad (\text{D.18})$$

$$\int_{-\infty}^{\infty} B \text{sinc}(\pi B(t - t')) \text{sinc}(\pi B(t - t'')) dt = \text{sinc}(\pi B(t'' - t')) \quad (\text{D.19})$$

D.4.2 SPDC

Now on to the interesting case, two mode down-conversion. Lets say we are just trying to measure the correlation. Then the measurement is two separate measurements of photon numbers, while the Hamiltonian is simply H_{spdc} .

$$\begin{aligned} H_{spdc} &= -i\chi\beta\left(\int_{-\infty}^{\infty} dt(\hat{A}_{1,t}\hat{A}_{2,t} - c.c)\right) \\ \hat{O}_1 &= \int_t^{t+T_d} dt\hat{A}_{1,t}^\dagger\hat{A}_{1,t}, \quad \hat{O}_2 = \int_t^{t+T_d} dt\hat{A}_{2,t}^\dagger\hat{A}_{2,t} \end{aligned} \quad (\text{D.20})$$

In light of the previous calculation, it is not very difficult to see how this operator transformation will progress.

$$\begin{aligned} [iH_{spdc}t_{int}, \hat{O}_1] &= r\left(\int_{-\infty}^{\infty} dt \int_{t_m}^{t_m+T_d} dt'[(\hat{A}_{1,t}\hat{A}_{2,t} - c.c), \hat{A}_{1,t'}^\dagger\hat{A}_{1,t'}]\right) \\ &= r\left(\int_{-\infty}^{\infty} dt \int_{t_m}^{t_m+T_d} dt'(\hat{A}_{1,t'}\hat{A}_{2,t}B\text{sinc}(\pi B(t-t')) + c.c)\right) \\ &= r\left(\int_{t_m}^{t_m+T_d} dt(\hat{A}_{1,t}\hat{A}_{2,t} + c.c)\right) \end{aligned}$$

$$\begin{aligned} [iHt_{int}, [iHt_{int}, \hat{O}_1]] &= r^2\left(\int_{-\infty}^{\infty} dt \int_{t_m}^{t_m+T_d} dt'[(\hat{A}_{1,t}\hat{A}_{2,t} - c.c), (\hat{A}_{1,t'}\hat{A}_{2,t'} + c.c)]\right) \\ &= 2r^2\left(\int_{-\infty}^{\infty} dt \int_{t_m}^{t_m+T_d} dt'[\hat{A}_{1,t}\hat{A}_{2,t}, \hat{A}_{1,t'}^\dagger\hat{A}_{2,t'}^\dagger]\right) \\ &= 2r^2\left(\int_{-\infty}^{\infty} \int_{t_m}^{t_m+T_d} dt dt' \hat{A}_{1,t}^\dagger\hat{A}_{1,t'} + \hat{A}_{2,t}^\dagger\hat{A}_{2,t'}\right. \\ &\quad \left.+ [\hat{A}_{1,t}, \hat{A}_{1,t'}^\dagger][\hat{A}_{2,t}, \hat{A}_{2,t'}^\dagger]\right) \\ &= 2r^2\left(\int_{t_m}^{t_m+T_d} dt(\hat{A}_{1,t}^\dagger\hat{A}_{1,t} + \hat{A}_{2,t}^\dagger\hat{A}_{2,t} + B)\right) \end{aligned}$$

where, $r = \chi\beta t_{int}$.

We could go on to calculate the remaining terms in the series by brute force, or we could look at the above calculation and see that a great simplification is possible here. The matrix element with vacuum of the first term will obviously go to zero since it is not balanced in creation and annihilation. The final form of the second term of the series of the form $\hat{O}_1 + \hat{O}_2 + [A_t, A_t^\dagger]$. This is completely symmetric in mode 1,2 and we can check easily that \hat{O}_2 evolves the same way. Since the

commutator will be a c number it will commute in future terms. Using all these implications, and (D.3) we can draw some easily simplifications to figure out what the measurement will be equal to. All the even terms will go to 0 and odd terms will survive.

$$\begin{aligned}
\langle(O_1 + O_2)\rangle &= \langle 0|U^\dagger(O_1 + O_2)U|0\rangle \\
&= \langle 0|\int_{t_m}^{t_m+T_d} dt \left(\hat{A}_{1,t}^\dagger \hat{A}_{1,t} + \hat{A}_{2,t}^\dagger \hat{A}_{2,t} + B\left(\sum_{n=0}^{\infty} \frac{(2r)^{2n}}{(2n)!}\right) - B \right) |0\rangle \\
&= \langle 0|\int_{t_m}^{t_m+T_d} dt ((\cosh(2r) - 1)B) |0\rangle \\
&= 2 \sinh^2 r B T_d
\end{aligned} \tag{D.21}$$

This is a beautiful result. From frequency domain calculation we know that the average photon number of an SPDC state is $2 \sinh^2 r$. We saw earlier that a broadband SPDC state in the time domain is simply a tensor product of time binned SPDC states, all of which have the squeezing parameter r . Since the average photon number of each of these SPDC states is $2 \sinh^2 r$, the average across all time bins should also be the same. But that is only if the detector time resolution matches exactly the time bin decomposition of the source. If the detector is slower it will integrate over multiple Fock states, and will therefore posit an average photon number higher $2 \sinh^2 r$. Therefore if ever we were able to hook up the TES to bright beams, we should get a large average photon number even for small r given that T_d of the TES is huge.

As we saw earlier, $U^\dagger O_1 U = U^\dagger O_2 U$. Therefore the subtraction,

$$\langle 0|U^\dagger(\hat{O}_1 - \hat{O}_2)U|0\rangle = 0 \tag{D.22}$$

This is expected since all the photons are produced in pairs and photon number difference is conserved (it is 0 initially for vacuum state).

Now the obvious question is what happens if the 2 detectors are off in time, so now the O_1 and O_2 will be characterized by t' and t'' , respectively, where $|t' - t''| = \Delta t$.

$$[iHt, O_1 + O_2] = r \int_{t_m}^{t_m+T_d} dt' \hat{A}_{1,t'} \hat{A}_{2,t'} + c.c + \hat{A}_{1,t''} \hat{A}_{2,t''} + c.c$$

Therefore we will get

$$\begin{aligned}
\langle (O_1 + O_2) \rangle &= \langle 0 | U^\dagger (O_1 + O_2) U | 0 \rangle \\
&= \langle 0 | \int_{t_{m2}}^{t_{m2}+T_d} dt' \left[\hat{A}_{1,t'}^\dagger \hat{A}_{1,t'} + \hat{A}_{2,t''}^\dagger \hat{A}_{2,t''} + \left(\sum_{n=1}^{\infty} \frac{(2r)^{2n}}{(2n)!} \right) \times \right. \\
&\quad \left(\int_{-\infty}^{\infty} dt \frac{\hat{A}_{1,t'}^\dagger \hat{A}_{1,t} + \hat{A}_{2,t'}^\dagger \hat{A}_{2,t} + [\hat{A}_{1,t'}, \hat{A}_{1,t}][\hat{A}_{2,t'}, \hat{A}_{2,t}]}{2} \right. \\
&\quad \left. \left. + \int_{-\infty}^{\infty} dt \frac{\hat{A}_{1,t''}^\dagger \hat{A}_{1,t} + \hat{A}_{2,t''}^\dagger \hat{A}_{2,t} + [\hat{A}_{1,t''}, \hat{A}_{1,t}][\hat{A}_{2,t''}, \hat{A}_{2,t}]}{2} \right) \right] | 0 \rangle \\
&= \langle 0 | \int_{t_m}^{t_m+T_d} dt \left(\frac{1}{2} B(\cosh(2r) - 1) \right) + \int_{t_m}^{t_m+T_d} dt \left(\frac{1}{2} B(\cosh(2r) - 1) \right) | 0 \rangle \\
&= \langle 0 | ((\cosh(2r) - 1) B) T_d | 0 \rangle \\
&= 2 \sinh^2 r B T_d \tag{D.23}
\end{aligned}$$

This gives the same result as before, as will the difference. That is because the expectation value of the photon number of a channel is independent of the time of measurement. For a measure of the time correlation we need to calculate the variance of these operators $\langle \Delta(\hat{O}_1 - \hat{O}_2) \rangle$, $\langle \Delta(\hat{O}_1 + \hat{O}_2) \rangle \propto \langle \hat{O}_1 \hat{O}_2 \rangle$ which can be calculated easily from $\langle (\hat{O}_1 + \hat{O}_2)^2 \rangle$. Again using t' and t'' to denote the **constant** non-zero time delay between the two detectors. Also since t_m , the start of the measurement, is our choice, we can always set $t_{m1} = t_{m2}$, i.e the two detectors are on at the same time.

$$\begin{aligned}
(O_1 + O_2)^2 &= \left(\int_{t_{m1}}^{t_{m1}+T_d} dt' \hat{A}_{1,t'}^\dagger \hat{A}_{1,t'} + \int_{t_{m2}}^{t_{m2}+T_d} dt'' \hat{A}_{2,t''}^\dagger \hat{A}_{2,t''} \right)^2 \\
&= \left(\int_{t_m}^{t_m+T_d} dt' (\hat{A}_{1,t'}^\dagger \hat{A}_{1,t'} + \hat{A}_{2,t''}^\dagger \hat{A}_{2,t''}) \right)^2 \\
[iHt_{int}, (O_1 + O_2)^2] &= [iHt_{int}, (O_1 + O_2)](O_1 + O_2) + (O_1 + O_2)[iHt_{int}, (O_1 + O_2)] \\
&= r \int_{t_m}^{t_m+T_d} dt' ((\hat{A}_{1,t'} \hat{A}_{2,t'} + \hat{A}_{1,t''} \hat{A}_{2,t''} + c.c.) (\hat{A}_{1,t'}^\dagger \hat{A}_{1,t'} + \hat{A}_{2,t''}^\dagger \hat{A}_{2,t''}) \\
&\quad + (\hat{A}_{1,t'}^\dagger \hat{A}_{1,t'} + \hat{A}_{2,t''}^\dagger \hat{A}_{2,t''}) (\hat{A}_{1,t'} \hat{A}_{2,t'} + \hat{A}_{1,t''} \hat{A}_{2,t''} + c.c.))
\end{aligned}$$

$$\begin{aligned}
& [iHt_{int}, [iHt_{int}, (O_1 + O_2)^2]] = [iHt_{int}, [iHt_{int}, (O_1 + O_2)]](O_1 + O_2) \\
& \quad + (O_1 + O_2)[iHt_{int}, [iHt_{int}, (O_1 + O_2)]] \\
& \quad + 2[iHt_{int}, [iHt_{int}, (O_1 + O_2)]]^2 \\
U^\dagger(O_1 + O_2)^2U &= \sum_{n=0}^{\infty} \sum_{m=0}^n \frac{C_m^n}{n!} [(O_1 + O_2)]^{m \text{ times}} [(O_1 + O_2)]^{n-m \text{ times}} \\
&= \sum_{m=0}^{\infty} \sum_{n=m}^{\infty} \frac{C_m^n}{(n)!} [(O_1 + O_2)]^{m \text{ times}} [(O_1 + O_2)]^{(n-m) \text{ times}} \\
&= \sum_{m=0}^{\infty} \frac{[(O_1 + O_2)]^{m \text{ times}}}{(m)!} \sum_{n=m}^{\infty} \frac{[(O_1 + O_2)]^{(n-m) \text{ times}}}{((n-m)!)} \\
&= \left(\sum_{m=0}^{\infty} \frac{[(O_1 + O_2)]^{m \text{ times}}}{(m)!} \right)^2 \tag{D.24}
\end{aligned}$$

We have already calculated the results of the summation before, so omitting all the normal ordered terms which will go to zero, we get -

$$\begin{aligned}
\langle 0|U^\dagger(O_1 + O_2)^2U|0\rangle &= \langle 0| \left(\sum_{m=0}^{\infty} \frac{[(O_1 + O_2)]^{m \text{ times}}}{(m)!} \right)^2 |0\rangle \\
&= \langle 0| \left(\sum_{m=0}^{\infty} \frac{[(O_1 + O_2)]^{2m \text{ times}}}{(2m)!} \right) \left(\sum_{n=0}^{\infty} \frac{[(O_1 + O_2)]^{2n \text{ times}}}{(2n)!} \right) |0\rangle \\
& \quad + \langle 0| \left(\sum_{m=0}^{\infty} \frac{[(O_1 + O_2)]^{2m+1 \text{ times}}}{(2m+1)!} \right) \left(\sum_{n=0}^{\infty} \frac{[(O_1 + O_2)]^{2n+1 \text{ times}}}{(2n+1)!} \right) |0\rangle \\
&= \langle (O_1 + O_2)^2 \rangle + \int_{t_m}^{t_m+T_d} \int_{t_m}^{t_m+T_d} dt'_1 dt'_2 \langle 0| \left(\sum_{m=0}^{\infty} \sum_{n=0}^{\infty} \frac{(2r)^{2m+2n+2}}{4(2m+1)!(2n+1)!} \right. \\
& \quad \times (\hat{A}_{1,t'} \hat{A}_{2,t'} + \hat{A}_{1,t''} \hat{A}_{2,t''} + c.c.) (\hat{A}_{1,t'} \hat{A}_{2,t'} + \hat{A}_{1,t''} \hat{A}_{2,t''} + c.c.) \rangle |0\rangle \\
&= \langle (O_1 + O_2)^2 \rangle + \int_{t_m}^{t_m+T_d} \int_{t_m}^{t_m+T_d} dt'_1 dt'_2 \langle 0| \frac{\sinh^2(2r)}{4} \\
& \quad \times (\hat{A}_{1,t'_1} \hat{A}_{2,t'_1} + \hat{A}_{1,t''_1} \hat{A}_{2,t''_1}) (\hat{A}_{1,t'_2} \hat{A}_{2,t'_2} + \hat{A}_{1,t''_2} \hat{A}_{2,t''_2}) \rangle |0\rangle \\
&= \langle (O_1 + O_2)^2 \rangle + \frac{\sinh^2(2r)}{4} \int_{t_m}^{t_m+T_d} \int_{t_m}^{t_m+T_d} dt'_1 dt'_2 B^2 (\text{sinc}^2(\pi B(t'_1 - t'_2)) \\
& \quad + \text{sinc}^2(\pi B(t'_1 - t''_2)) + \text{sinc}^2(\pi B(t''_1 - t'_2)) + \text{sinc}^2(\pi B(t''_1 - t''_2))) \\
&= \langle (O_1 + O_2)^2 \rangle + \frac{\sinh^2(2r)}{2} B^2 \\
& \quad \times \int_0^{T_d} \int_0^{T_d} dt'_1 dt'_2 (\text{sinc}^2(\pi B(t'_1 - t'_2)) + \text{sinc}^2(\pi B(t'_1 - t'_2 + \Delta t))) \tag{D.25}
\end{aligned}$$

This, despite being the accurate result, is not quite as illuminating as it can be with a few more assumptions and simplifications. The final simplification is only applicable if we assume $T_d \gg B$ and $T_d \gg \Delta t$ so that we can set the measurement integral to be $\int_{-T_d/2}^{T_d/2} dt B \text{sinc}^2(\pi B t) \simeq 1$. This is a pretty good approximation, since $\frac{1}{T_d} \int_{-T_d/2}^{T_d/2} \int_{-T_d/2}^{T_d/2} dt_1 dt_2 \text{sinc}^2(\pi(t_1 - t_2))$ tends to 1 for large T_d .

$$\langle (O_1 + O_2)^2 \rangle = \langle (O_1 + O_2) \rangle^2 + \sinh^2(2r) B T_d$$

$$\implies \langle (O_1 + O_2)^2 \rangle - \langle O_1 + O_2 \rangle^2 = V^2(O_1) + V^2(O_2) + 2V(O_1, O_2) \quad (\text{D.26})$$

$$= \sinh^2(2r) B T_d \quad (\text{D.27})$$

So what is the correlation? A measure of correlation can be the number of photons that arrive together divided by the total number of photons. If N_1 and N_2 are the number of photons arriving at the two channels then $\frac{\langle N_1 N_2 \rangle - \langle N_1 \rangle \langle N_2 \rangle}{\langle N_1 \rangle}$ is ratio of photon pair detection events to the individual photon detection events. Then this is the correlation function, so I shall call it thus for lack of better, perhaps more correct name.

If we calculate $\langle O_1 - O_2 \rangle$ we will get a minus sign between two 'equal' sinc's at the end and the answer will simply be 0. This is good, $N_1 - N_2$ should be zero for small Δt . It also tells us that -

$$\begin{aligned} \langle (O_1 + O_2)^2 \rangle - \langle O_1 + O_2 \rangle^2 &= V^2(O_1) + V^2(O_2) + 2V(O_1, O_2) \\ &= \sinh^2(2r) B T_d \end{aligned} \quad (\text{D.28})$$

$$\begin{aligned} \langle (O_1 - O_2)^2 \rangle - \langle O_1 + O_2 \rangle^2 &= V^2(O_1) + V^2(O_2) - 2V(O_1, O_2) \\ &= 0 \end{aligned} \quad (\text{D.29})$$

$$\implies V^2(O_1) = V^2(O_2) = V(O_1, O_2) = (1/4) \sinh^2(2r) B T_d \quad (\text{D.30})$$

Therefore the correlation is given by -

$$\begin{aligned} \text{Correlation}(\Delta t) &= \frac{(\sinh^2(2r) B T_d)}{4 \sinh^2 r B T_d} \\ &= \cosh^2 r \end{aligned} \quad (\text{D.31})$$

This agrees with the calculation of $\Delta(N_1 + N_2)$ and the correlation in the frequency domain calculation i.e the correlation is independent of Δt if $T_d \gg \Delta t$.

If we calculate correlation as the ratio of number of pair 'events' to number of individual 'events', the correlation will go to 1 for perfect correlation. However

$\langle N_1 N_2 \rangle$ and $\langle N_1 \rangle$ are not counting detecting events rather photons, or in other words, detection events weighted by the photon number of the events. In this case obviously the max is not 1. We can prove easily that the maximum correlation is in fact as described above $\cosh^2 r$. A quick check is that single photon correlation is equivalent to event correlation because the weights of both $N_1 N_2$ and N_1 events are equal to 1 (also $V(N_1), V(N_2) \rightarrow 0$). Correspondingly at low squeezing when all we have is mostly single photon pairs we see that $\cosh^2 r \simeq 1$ for $r \rightarrow 0$ supporting the claim.

D.4.3 Hong-Ou-Mandel interference

Now that we have satisfactory analyses of direct correlation, we can look at the central result towards which we have been driving slowly but inexorably. We have already calculated the source Hamiltonian in the previous section. Now to see what we will see at the detector.

The detector operator is again the same, O_1 and O_2 , which is simply the number operator integrated over the detector time resolution. We have already seen that small time difference between 2 beams arriving at the 2 detectors is ignored and integrated over by the detector if $T_d \gg 1/B$ and $T_d \gg \Delta t$. For these assumptions to be violated for the TES, we would have to have $B \simeq 10\text{MHz}$ or path difference between the two beams $\Delta x = c \cdot 100\text{ns} = 30\text{m}$. Neither is a very likely event for the TES, so for now we can ignore the separation of the detectors in time. Even if we had a slightly faster detector, this is still of only minor academic interest since we can always shift one trace in time to get back the correlation. Thanks to that calculation now we know exactly what the quantification of this hand-waving reasoning is, how big the T_d has to be with respect to B and Δt , but we don't need to do that calculation in future analyses. Therefore the operator becomes

$$\begin{aligned} O_1 + O_2 &= \int_{t_m}^{t_m+T_d} dt (\hat{A}_{1,t}^\dagger \hat{A}_{1,t} + \hat{A}_{2,t}^\dagger \hat{A}_{2,t}) \\ &= \int_{t_m}^{t_m+T_d} dt (\hat{A}_{+,t}^\dagger \hat{A}_{+,t} + \hat{A}_{-,t}^\dagger \hat{A}_{-,t}) \end{aligned}$$

The general HOM hamiltonian can simply be H_{HOM2} as calculated in [D.14](#).

$$\begin{aligned} H_{HOM} &= \frac{-i\chi\beta}{2} \left(\int_{-\infty}^{\infty} dt' (\hat{A}_{1,t'} \hat{A}_{1,t''} + \hat{A}_{2,t'} \hat{A}_{1,t''} - \hat{A}_{1,t'} \hat{A}_{2,t''} - \hat{A}_{2,t'} \hat{A}_{2,t''} + c.c) \right) \\ &= -i\chi\beta \left(\int_{-\infty}^{\infty} dt' (\hat{A}_{+,t'} \hat{A}_{-,t''} + c.c) \right) \end{aligned} \quad (D.32)$$

where $t'' = t' + \Delta t$ and Δt is a constant time difference in the path lengths of the 2 beams A_1 and A_2 . This Δt , is not like the one in the previous paragraph. This is because this Δt is not just before the detector but before the BS and the action of the BS is not integrated and averaged over a large time like in the detector. In the $+/-$ compact notation, we see that its similar to the shifted two mode correlation. So here we go again -

$$\begin{aligned} [iHt_{int}, O_1 + O_2] &= r \int_{t_m}^{t_m+T_d} dt \int_{-\infty}^{\infty} dt' [(\hat{A}_{+,t'} \hat{A}_{-,t''} - c.c)(\hat{A}_{+,t}^\dagger \hat{A}_{+,t} + \hat{A}_{-,t}^\dagger \hat{A}_{-,t})] \\ &= 2r \int_{t_m}^{t_m+T_d} dt' (\hat{A}_{+,t'} \hat{A}_{-,t''} + c.c) \\ [iHt_{int}, [iHt_{int}, O_1 + O_2]] &= 2r^2 \int_{t_m}^{t_m+T_d} dt'' \int_{-\infty}^{\infty} dt [(\hat{A}_{+,t} \hat{A}_{-,t'} + c.c)(\hat{A}_{+,t''}^\dagger \hat{A}_{-,t''}^\dagger + c.c)] \\ &= 4r^2 \int_{t_m}^{t_m+T_d} dt (\hat{A}_{+,t}^\dagger \hat{A}_{+,t'} + \hat{A}_{-,t}^\dagger \hat{A}_{-,t'} + B) \\ \implies \langle O_1 + O_2 \rangle &= 2\sinh^2 r B T_d \end{aligned} \quad (D.33)$$

$$\begin{aligned} \langle (O_1 + O_2)^2 \rangle &= \langle O_1 + O_2 \rangle^2 + \sinh^2(2r) \int_{t_m}^{t_m+T_d} dt \int_{t_m}^{t_m+T_d} dt'' \langle 0 | \hat{A}_{+,t} \hat{A}_{-,t'} \hat{A}_{+,t''}^\dagger \hat{A}_{-,t''}^\dagger | 0 \rangle \\ &= \langle O_1 + O_2 \rangle^2 + \sinh^2(2r) B^2 \int_{t_m}^{t_m+T_d} dt \int_{t_m}^{t_m+T_d} dt'' \text{sinc}^2(\pi B(t - t'')) \end{aligned} \quad (D.34)$$

Therefore the variance of $O_1 + O_2$, $\Delta(O_1 + O_2) = \Delta O_1 + \Delta O_2 + 2V(O_1, O_2)$ scales with T_d . Before we decry all this work seeing the above result, lets calculate the

other operator $O_1 - O_2 = \hat{A}_{+,t}^\dagger \hat{A}_{-,t} + \hat{A}_{-,t}^\dagger \hat{A}_{+,t}$.

$$\begin{aligned} [iHt_{int}, O_1 - O_2] &= r \int_{t_m}^{t_m+T_d} dt \int_{-\infty}^{\infty} dt' [(\hat{A}_{+,t'} \hat{A}_{-,t''} - c.c.), \hat{A}_{+,t}^\dagger \hat{A}_{-,t} + \hat{A}_{-,t}^\dagger \hat{A}_{+,t}] \\ &= r \int_{t_m}^{t_m+T_d} dt' (\hat{A}_{+,t'} \hat{A}_{+,t''} + \hat{A}_{-,t'} \hat{A}_{-,t''} + c.c) \end{aligned}$$

$$\begin{aligned} [iHt_{int}, [iHt_{int}, O_1 - O_2]] &= 2r^2 \int_{t_m}^{t_m+T_d} dt' \hat{A}_{+,t''} \hat{A}_{-,t''}^\dagger + \hat{A}_{+,t'} \hat{A}_{-,t'+2\Delta t}^\dagger \\ &\quad + \hat{A}_{+,t'}^\dagger \hat{A}_{-,t'} + \hat{A}_{+,t'-\Delta t}^\dagger \hat{A}_{-,t''} \end{aligned}$$

$$[iHt_{int}, [iHt_{int}, [iHt_{int}, O_1 - O_2]]] = 4r^3 \int_{t_m}^{t_m+T_d} dt' (\hat{A}_{+,t'} \hat{A}_{+,t''} + \hat{A}_{-,t'} \hat{A}_{-,t''} + c.c)$$

$$\implies \langle O_1 - O_2 \rangle = 0 \quad (\text{D.35})$$

$$\begin{aligned} \langle (O_1 - O_2)^2 \rangle &= \sum_{n_1, n_2} \frac{\sinh^2(2r)B^2}{4} \int_{t_m}^{t_m+T_d} \int_{t_m}^{t_m+T_d} dt dt'' \langle 0 | \hat{A}_{+,t} \hat{A}_{+,t'} \hat{A}_{+,t''}^\dagger \hat{A}_{+,t'''}^\dagger \\ &\quad + \hat{A}_{-,t} \hat{A}_{-,t'} \hat{A}_{-,t''}^\dagger \hat{A}_{-,t'''}^\dagger | 0 \rangle \\ &= \frac{\sinh^2(2r)B^2}{4} \int_{t_m}^{t_m+T_d} dt \int_{t_m}^{t_m+T_d} dt'' (2\text{sinc}^2(\pi B(t-t'')) \\ &\quad + 2\text{sinc}(\pi B(t'-t''))\text{sinc}(\pi B(t-t'''))) \end{aligned} \quad (\text{D.36})$$

$$\simeq \frac{\sinh^2(2r)}{2} BT_d (1 + \text{sinc}(2\pi B\Delta t)) \quad (\text{D.37})$$

Therefore

$$\begin{aligned} \text{Correlation} &= \frac{\langle \Delta(O_1 + O_2) \rangle - \langle \Delta(O_1 - O_2)^2 \rangle}{\langle O_1 \rangle} \\ &= \frac{BT_d(2\sinh^2(2r) - \sinh^2(2r)(1 + \text{sinc}(2\pi B\Delta t)))}{8\sinh^2 r BT_d} \end{aligned} \quad (\text{D.38})$$

For small r ,

$$\text{correlation} \simeq \frac{1 - \text{sinc}(2\pi B\Delta t)}{2} \quad (\text{D.39})$$

This is an important result. First of all this means that when $\Delta t = 0$ there is zero correlation, which is exactly Hong-Ou-Mandel interference. Even more interesting however, is that for non zero Δt , the correlation varies as sinc of $B\Delta t$. Therefore as we increase Δt from zero, we will restore the zero dip in correlation for non zero Δt not once but repeatedly at $\Delta t = n/B$ for all $n \in I$. Also interesting is the fact that the maximum correlation is not 1 but $1/2$. This is caused by classical interference, since I have assumed there is perfect classical interference, only an additional time lag. The strict correlation without any approximations is -

$$\begin{aligned} \text{Correlation} = \frac{\cosh^2(r)}{2} \int_{t_m}^{t_m+T_d} dt \int_{t_m}^{t_m+T_d} dt'' \text{sinc}^2(\pi B(t-t'')) \\ - \text{sinc}(\pi B(t'-t'')) \text{sinc}(\pi B(t-t'')) \quad (\text{D.40}) \end{aligned}$$

However, remember that this is just the re-derivation of the simple HOM result. We get a sinc function because we chose a square bandwidth hence we get the repeated zero dips. Had we chosen a Gaussian bandwidth, we would get a Gaussian dip with no recurrence of dips. The non-trivial result is when we put the filter cavity in.

D.4.4 HOM after filter cavity

Now lets see what happens if we have a filter cavity as well in our HOM experiment with a Δt time lag introduced *inside* the cavity

$$\begin{aligned} A_{1,t} &= \sum_{n=0}^N c_n A_{1,t,n} \\ H_{\text{filteredspdc}} &= \frac{r}{2} \sum_{n,m=0}^N (c_n c_m) \int_{-\infty}^{\infty} dt ((\hat{A}_{1,t,m} + \hat{A}_{2,t,m})(\hat{A}_{1,t',n} - \hat{A}_{2,t',n}) - c.c) \\ O_1 + O_2 &= \int_{t_m}^{t_m+T_d} dt (\hat{A}_{1,t}^\dagger \hat{A}_{1,t} + \hat{A}_{2,t}^\dagger \hat{A}_{2,t}) \end{aligned}$$

This is an infinite series of the earlier state each with time signature n,m. Therefore we can treat this as-

$$H_{\text{filteredspdc}} = \sum_{n,m=0}^N c_n c_m H_{\text{HOM},t,n,t',m}$$

where $t, n = t - 2nt_c$, and $t', m = t + \delta t - 2mt_c = t + \Delta t$. Therefore we can extrapolate the results of the earlier calculation and we get,

$$\langle O_1 + O_2 \rangle = \sum_{n,m=0}^N c_n c_m \langle O_1 + O_2 \rangle = 2 \sinh^2 r B T_d \quad (\text{D.41})$$

$$\begin{aligned} \langle (O_1 + O_2)^2 \rangle &= \left(\sum_{n,m=0}^N c_n c_m \langle (O_1 + O_2) \rangle \right)^2 \\ &+ \sinh^2(2r) \langle \left(\sum_{n,n'=0}^N c_n c_{n'} \hat{A}_{+,t} \hat{A}_{-,t'} \right) \left(\sum_{n'',n'''=0}^N c_{n''} c'_{n''} \hat{A}_{+,t''}^\dagger \hat{A}_{-,t'''}^\dagger \right) \rangle \\ &= \langle (O_1 + O_2) \rangle^2 + \sinh^2(2r) \sum_{n,n',n'',n'''=0}^N c_n c_{n'} c_{n''} c_{n'''} \\ &\quad \times \int_{t_m}^{t_m+T_d} dt \int_{t_m}^{t_m+T_d} dt'' \text{sinc}(\pi B(t - t'')) \text{sinc}(\pi B(t' - t''')) \end{aligned} \quad (\text{D.42})$$

$$\langle (O_1 - O_2) \rangle = 0$$

$$\begin{aligned} \langle (O_1 - O_2)^2 \rangle &= \frac{\sinh^2(2r)}{4} \int_{t_m}^{t_m+T_d} dt_1 \int_{t_m}^{t_m+T_d} dt_2 \langle \left(\sum_{n,n'=0}^N c_n c_{n'} (\hat{A}_{+,t} \hat{A}_{+,t'} + \hat{A}_{-,t} \hat{A}_{-,t'}) \right) \\ &\quad \times \left(\sum_{n'',n'''=0}^N (c_{n''} c_{n'''} (\hat{A}_{+,t''}^\dagger \hat{A}_{+,t'''}^\dagger + \hat{A}_{-,t''}^\dagger \hat{A}_{-,t'''}^\dagger)) \right) \rangle \\ &= \frac{\sinh^2(2r)}{4} \sum_{n,n',n'',n'''=0}^N c_n c_{n'} c_{n''} c_{n'''} \int_{t_m}^{t_m+T_d} dt_1 \int_{t_m}^{t_m+T_d} dt_2 \\ &\quad \times (\hat{A}_{+,t} \hat{A}_{+,t'} \hat{A}_{+,t''}^\dagger \hat{A}_{+,t'''}^\dagger + \hat{A}_{-,t} \hat{A}_{-,t'} \hat{A}_{-,t''}^\dagger \hat{A}_{-,t'''}^\dagger) \\ &= \frac{\sinh^2(2r)}{4} \sum_{n,n',n'',n'''=0}^N c_n c_{n'} c_{n''} c_{n'''} \int_{t_m}^{t_m+T_d} dt_1 \int_{t_m}^{t_m+T_d} dt_2 \\ &\quad \times (2 \text{sinc}(\pi B(t - t'')) \text{sinc}(\pi B(t' - t''')) \\ &\quad + 2 \text{sinc}(\pi B(t - t''')) \text{sinc}(\pi B(t' - t''))) \end{aligned} \quad (\text{D.43})$$

$$\begin{aligned}
\text{Correlation} &= \frac{\langle \Delta(O_1 + O_2) \rangle - \langle \Delta(O_1 - O_2) \rangle}{\langle O_1 \rangle} \\
&= \frac{\sinh^2(2r)}{8 \sinh^2(r)} \sum_{n,n',n'',n'''}^N c_n c_{n'} c_{n''} c_{n'''} \int_{t_m}^{t_m+T_d} dt_1 \\
&\quad \times \left(\int_{t_m}^{t_m+T_d} dt_2 \text{sinc}(\pi B(t - t'')) \text{sinc}(\pi B(t' - t''')) \right. \\
&\quad \quad - (\text{sinc}(\pi B(t - t'')) \text{sinc}(\pi B(t' - t''')) \\
&\quad \quad \quad \left. + \text{sinc}(\pi B(t - t''')) \text{sinc}(\pi B(t' - t'')) \right) \\
&= \frac{\cosh^2 r}{2} \sum_{n,n',n'',n'''}^N c_n c_{n'} c_{n''} c_{n'''} \int_{t_m}^{t_m+T_d} dt_1 \int_{t_m}^{t_m+T_d} dt_2 \\
&\quad \times \left(\text{sinc}(\pi B(t - t'')) \text{sinc}(\pi B(t' - t''')) \right. \\
&\quad \quad \left. - \text{sinc}(\pi B(t - t''')) \text{sinc}(\pi B(t' - t'')) \right) \quad (\text{D.44})
\end{aligned}$$

Here $t = t_1 - 2nt_c$, $t' = t_1 + \Delta t - 2n't_c$, $t'' = t_2 - 2n''t_c$, $t''' = t_2 + \Delta t - 2n'''t_c$. Now for small r this reduces to,

$$\begin{aligned}
\text{Correlation} &= \sum_{n,n',n'',n'''=0}^N \frac{c_n c_{n'} c_{n''} c_{n'''}}{2} \int_{t_m}^{t_m+T_d} dt_1 \int_{t_m}^{t_m+T_d} dt_2 \\
&\quad \times \left(\text{sinc}(\pi B(t - t'')) \text{sinc}(\pi B(t' - t''')) \right. \\
&\quad \quad \left. - \text{sinc}(\pi B(t - t''')) \text{sinc}(\pi B(t' - t'')) \right) \quad (\text{D.45})
\end{aligned}$$

This is the central result of this analysis.

It is slightly complicated to understand, so lets try to analyse it. So the correlation goes to zero when the two sinc products are equal, which happens when $\Delta t = 0$. That's good.

Now the question is there any other way for the correlation to vanish even with non zero Δt ? There is none. The zero is attained only for $\Delta t = 0$. The math shows our intuition clearly that because there is an huge summation over all the round trips of the initial pulse, each time there is a "chirped" shift of one mode with respect to the other by an additional Δt . This proves that even if Δt is tiny but non-zero, (say picosecond delay in one polarization) compared to t_c (say nanosecond for a Ghz filter cavity), it causes major problems for HOM dip because it adds up on only one mode and spoils the indistinguishability. This is probably the reason why we cannot see HOM dip (at least not down to 0) in our experiment

even if all else worked perfectly. The cavity transforms the picosecond pulse into a train of picosecond pulses in a nanosecond envelope and the two trains have to still match exactly at the picosecond level.

However now when $\Delta t = 2kt_c$, where $k \in I$ we find that this sum can have small values. At these values all the terms where $n = n'$ or $n'' = n'''$ go to 0. Therefore even though the sum doesn't go to $1/2$, as Δt increases the correlation dips every time $\Delta t = 2kt_c$. This gives us a recurring dip at every multiple of the cavity round trip time. For small k , the contribution of small n, n', n'', n''' is greater which are more likely to cancel out and thus the dip is large. For large k , the greater contribution is from the large n which cancel out rarely and therefore the dip is much smaller. Therefore now we would see picosecond wide dips in a nanosecond envelope.

The final exercise is to imagine what would happen if we made t_c very small. In this case the dips would happen very often. In the limiting case, we would see no recurring dips but a single wide dip representing the sum of many narrow dips. Thus the dip is broadened to the width of the cavity linewidth, i.e nanosecond. This is exactly the effect we would want ideally when we use a cavity to filter the frequency, thus broaden the pulse length and hence broaden the HOM dip.

Thus we conclude that a picosecond time delay inside the cavity will cause the HOM dip to vanish even though we think that a picosecond is much smaller than the cavity linewidth of a nanosecond. Secondly if there is no delay inside the cavity, then we get a series of HOM dips instead of just one, where the dips are separated by the cavity round trip time. The central dip is the only one that goes to zero and each subsequent dip is smaller than the previous one. This was experimentally demonstrated recently [81]. Third it is definitely possible with a short cavity to actually broaden the dip to a nanosecond. This happens when the round trip time of the cavity is short enough compared to the pulse width of the input light that the recurrent dips cannot be distinguished. For that $2t_c$ has to be of the order of the pulse width δt . In our case the SPDC bandwidth is \sim THz, $\delta t = ps$ and the filter cavity was 1 mm or 3ps round trip. This does not quite satisfy our condition and therefore we would indeed see a large temporal envelopes with a train of SPDC pulses inside rather than just large temporal modes.

D.5 Future Work

The first thing is to translate all these calculations to a gaussian envelope. While the general inferences from this work can be applied to the gaussian case the actual values cannot. Therefore unless we plan to do experiments using top hat frequency filters, these calculations cannot be translated to experiments directly.

The second thing to extend these results for fast detectors. The goal of this work was to establish whether the TES could see HOM in our experiments and the effect of the filter cavity on this experiment. Therefore I have made the assumption that $T_d \gg \delta t, \Delta t$ which simplified the final answer in a lot of the calculations. However in the case of photon subtraction from a bright squeezed state or squeezing detection, or time domain CV entanglement, the exact opposite case needs to be investigated, where the input mode is nearly monochromatic but the detector temporal mode is short. This case has many exciting and interesting results, such as the splitting of the optical temporal modes into the detector temporal modes.

Appendix E

Fock state tomography

The experiment we completed and published in JOSA B demonstrated the feasibility of the direct measurement of Wigner function using photon number resolving measurement. In this paper we performed the tomography of the vacuum state, coherent state and a coherent state with phase noise. All of these states have Wigner functions that are positive everywhere. These states are can be described by classical and other physical theories besides quantum physics. The most telling aspect of the classicality of the coherent state is that its qualitative nature is unaffected by losses.

The main use of Wigner function measurement is for characterization of quantum states. Particularly in quantum information applications where loss is extremely destructive to information, characterizing states and ancilla is extremely important. Therefore we want to use this method of tomography to characterize novel, highly non-classical states, specifically those with negative Wigner functions. The simplest such state is the single photon Fock state.

E.1 Generation of single photon state

E.1.1 Theory

One method of generation of single photon is by using the TMSS. Using Type-II PPKTP crystal we can generate

$$|TMSS\rangle = \frac{1}{\cosh r} \sum_{n=0}^{\infty} \tanh^n r |n\rangle_1 |n\rangle_2$$

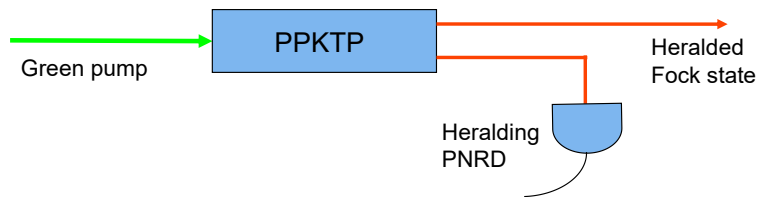


FIGURE E.1: Type-II PPKTP crystal down-converts green photons into infra-red photon pairs used to create heralded Fock states

Now if we use a photon number resolving detector to measure mode 2, and post select the state in mode 1 contingent on the measurement of say, $n = k$ on mode 1 then we get

$$\begin{aligned} |\psi\rangle_1 &= {}_2\langle k | \frac{1}{\cosh r} \sum_{n=0}^{\infty} \tanh^n r |n\rangle_1 |n\rangle_2 \\ &= \frac{\tanh^k r}{\cosh r} |k\rangle_1 \end{aligned} \quad (\text{E.1})$$

leaving mode 1 in a Fock state $|k\rangle$. This is known as the heralded Fock state.

E.1.2 Experiment

However the experimental implementation of heralded Fock state has to overcome several practical hurdles. To prevent the spontaneous parametric down-conversion (SPDC) emission from being extremely multimode and lossy, we use an optical parametric oscillator (OPO) and a filter cavity (FC). The details of our attempts leading up to this installation of these two cavities can be found in Reihaneh Shahrokhshahi's doctoral thesis.

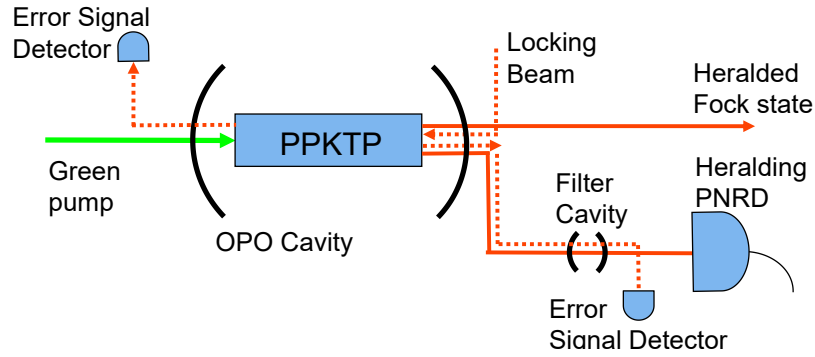


FIGURE E.2: Type-II PPKTP crystal downconverts green photons into infra-red photon pairs used to create heralded Fock states

However using these cavity adds additional requirements. First the filter cavity's resonant frequency has to be locked on to the resonant frequency of the OPO so that it allows the resonant mode through while filtering the other frequencies. Secondly using an OPO increases the PDC emission in the resonant frequency, but does not eliminate the spontaneous emission in the other modes. Therefore to maximize the emission into a specific frequency mode, we have to lock the OPO so that it is doubly resonant. It is not feasible to have two different frequencies resonant at both cavities. Therefore both cavities must be locked at the same frequency which is half the pump frequency.

Now, despite the need for active stabilization of both cavities, no locking beam can be used during the experiment. This is because the TES can detect very low (fW) of power and gets saturated at fairly low powers as well (pW). Therefore any locking beam would saturate the TES. The solution for this is to use ON/OFF locking. First a locking beam is used to lock the cavities and no data is taken during this time. Then the locking beam is turned off while the voltages on the locking electronics thus keeping the system as close to the locked state as possible but without any active stabilization. Without the locking beam the experimental data can be acquired now. After a short acquisition window, the data acquisition is stopped and the locking beam and stabilization reactivated. The process is repeated until all the required data has been acquired.

The locking beam was turned off and on using Thorlabs diaphragm shutter and controller SBH05T. The switching between active stabilization and passive voltage was done using the Jump option on the Vescent D2-125 laser servo. Both of these are controlled using a voltage signal generated by the SR830 lockin amplifier AUX outputs which are controlled by a computer using Instrument Control Toolbox in

MATLAB. Using this setup I found that it was possible to keep both the OPO and FC nearly locked for over an hour, while still being able to block the locking beam and acquire data for 2/3rd of that time.

Bibliography

- [1] O. Pfister, “Quantum optics and quantum information lecture notes,” QOQI8880 (2010).
- [2] D. F. Walls and G. J. Milburn, “Quantum optics,” Springer (1994).
- [3] A. E. Lita, A. J. Miller, and S. W. Nam, “Counting near-infrared single-photons with 95% efficiency,” *Opt. Expr.* **16**, 3032–3040 (2008).
- [4] E. Wigner, “On the quantum correction for thermodynamic equilibrium,” *Phys. Rev.* **40**, 749–759 (1932).
- [5] S. M. Barnett and P. M. Radmore, *Methods in Theoretical Quantum Optics* (Clarendon Press, Oxford, 1997).
- [6] A. Einstein, B. Podolsky, and N. Rosen, “Can quantum-mechanical description of physical reality be considered complete?” *Phys. Rev.* **47**, 777 (1935).
- [7] A. Aspect, P. Grangier, and G. Roger, “Experimental realization of Einstein-Podolsky-Rosen-Bohm gedankenexperiment: A new violation of Bell’s inequalities,” *Phys. Rev. Lett.* **49**, 91–94 (1982).
- [8] N. C. Menicucci, “Fault-tolerant measurement-based quantum computing with continuous-variable cluster states,” *Phys. Rev. Lett.* **112**, 120504 (2014).
- [9] D. T. Smithey, M. Beck, M. G. Raymer, and A. Faridani, “Measurement of the Wigner distribution and the density matrix of a light mode using optical homodyne tomography: Application to squeezed states and the vacuum,” *Phys. Rev. Lett.* **70**, 1244 (1993).
- [10] U. Leonhardt, *Measuring the Quantum State of Light* (Cambridge University Press, Cambridge, U.K., 1997).

-
- [11] A. I. Lvovsky and M. G. Raymer, “Continuous-variable optical quantum-state tomography,” *Rev. Mod. Phys.* **81**, 299 (2009).
- [12] R. Blume-Kohout, “Optimal, reliable estimation of quantum states,” *New J. Phys.* **12**, 043034 (2010).
- [13] A. Royer, “Wigner function as the expectation value of a parity operator,” *Phys. Rev. A* **15** (1976).
- [14] D. Leibfried, D. M. Meekhof, B. E. King, C. Monroe, W. M. Itano, and D. J. Wineland, “Experimental determination of the motional quantum state of a trapped atom,” *Phys. Rev. Lett.* **77** (1996).
- [15] K. Banaszek and K. Wódkiewicz, “Direct probing of quantum phase space by photon counting,” *Phys. Rev. Lett.* **76**, 4344 (1996).
- [16] K. Banaszek, C. Radzewicz, K. Wódkiewicz, and J. S. Krasieński, “Direct measurement of the Wigner function by photon counting,” *Phys. Rev. A* **60**, 674–677 (1999).
- [17] J. S. Bell, *Speakable and unspeakable in quantum mechanics* (Cambridge University Press, 1987), chap. 21, “*EPR correlations and EPW distributions*”, pp. 196–200.
- [18] N. D. Mermin, “From Cbits to Qbits: Teaching computer scientists quantum mechanics,” *American Journal of Physics* **71**, 23–30 (2003).
- [19] D. M. Greenberger, M. A. Horne, and A. Zeilinger, “Going beyond Bell’s theorem,” in “Bell’s Theorem, Quantum theory and Conceptions of the Universe,” M. Kafatos, ed. (Kluwer, Dordrecht, The Netherlands, 1989), p. 69.
- [20] C. Bennett, G. Brassard, C. Crépeau, R. Josza, A. Peres, and W. Wootters, “Teleporting an unknown quantum state via dual classical and einstein-podolsky-rosen channels,” *Phys. Rev. Lett.* **70**, 1895 (1993).
- [21] C. H. Bennett and S. J. Wiesner, “Communication via one- and two-particle operators on einstein-podolsky-rosen states,” *Phys. Rev. Lett.* **69**, 2881 (1992).
- [22] M. A. Nielsen, “Optical quantum computation using cluster states,” *Phys. Rev. Lett.* **93**, 040503 (2004).

- [23] R. P. Feynman, “Simulating physics with computers,” *Int. J. Theor. Phys.* **21**, 467–488 (1982).
- [24] O. Pfister, S. Feng, G. Jennings, R. Pooser, and D. Xie, “Multipartite continuous-variable entanglement from concurrent nonlinearities,” *Phys. Rev. A* **70**, 020302 (2004).
- [25] N. C. Menicucci, S. T. Flammia, and O. Pfister, “One-way quantum computing in the optical frequency comb,” *Phys. Rev. Lett.* **101**, 130501 (2008).
- [26] M. Pysher, Y. Miwa, R. Shahrokhshahi, R. Bloomer, and O. Pfister, “Parallel generation of quadripartite cluster entanglement in the optical frequency comb,” *Phys. Rev. Lett.* **107**, 030505 (2011).
- [27] S. Yokoyama, R. Ukai, S. C. Armstrong, C. Sornphiphatphong, T. Kaji, S. Suzuki, J. Yoshikawa, H. Yonezawa, N. C. Menicucci, and A. Furusawa, “Ultra-large-scale continuous-variable cluster states multiplexed in the time domain,” *Nat. Photon.* **7**, 982 (2013).
- [28] S. T. Flammia, N. C. Menicucci, and O. Pfister, “The optical frequency comb as a one-way quantum computer,” *J. Phys. B*, **42**, 114009 (2009).
- [29] J. Eisert, S. Scheel, and M. B. Plenio, “Distilling Gaussian states with Gaussian operations is impossible,” *Phys. Rev. Lett.* **89**, 137903 (2002).
- [30] J. Niset, J. Fiurášek, and N. J. Cerf, “No-go theorem for Gaussian quantum error correction,” *Phys. Rev. Lett.* **102**, 120501 (2009).
- [31] N. C. Menicucci, P. van Loock, M. Gu, C. Weedbrook, T. C. Ralph, and M. A. Nielsen, “Universal quantum computation with continuous-variable cluster states,” *Phys. Rev. Lett.* **97**, 110501 (2006).
- [32] D. Gottesman, A. Kitaev, and J. Preskill, “Encoding a qubit in an oscillator,” *Phys. Rev. A* **64**, 012310 (2001).
- [33] A. Ourjoumtsev, R. Tualle-Brouri, J. Laurat, and P. Grangier, “Generating optical Schrödinger kittens for quantum information processing,” *Science* **312**, 83–86 (2006).
- [34] H. M. Vasconcelos, L. Sanz, and S. Glancy, “All-optical generation of states for “Encoding a qubit in an oscillator”,” *Opt. Lett.* **35**, 3261–3263 (2010).

- [35] A. Ourjoumtsev, H. Jeong, R. Tualle-Brouri, and P. Grangier, “Generation of optical ‘Schrödinger cats’ from photon number states,” *Nature (London)* **448**, 784 (2007).
- [36] S. Bravyi and A. Kitaev, “Universal quantum computation with ideal clifford gates and noisy ancillas,” *Phys. Rev. A* **71**, 022316 (2005).
- [37] J. Schwinger, “On angular momentum,” U.S. Atomic Energy Commission Report. No. NYO-3071 (1952), reprinted in *Quantum Theory of Angular Momentum*, edited by L. C. Biedenharn and H. van Dam (Academic Press, New York, 1965), pp. 229–279 (1965).
- [38] R. L. Hudson, “When is the Wigner quasi-probability density non-negative?” *Rep. Math. Phys.* **6**, 249–252 (1974).
- [39] B. Yurke, S. McCall, and J. Klauder, “SU(2) and SU(1,1) interferometers,” *Phys. Rev. A* **33**, 4033 (1986).
- [40] T. Kim, O. Pfister, M. J. Holland, J. Noh, and J. L. Hall, “Influence of decorrelation on Heisenberg-limited interferometry using quantum correlated photons,” *Phys. Rev. A* **57**, 4004 (1998).
- [41] R. Evans and O. Pfister, “On the experimental violation of Mermin’s inequality with imperfect measurements,” *Quantum Information and Computation* **11**, 820 (2011).
- [42] W. Bowen, R. Schnabel, H. Bachor, and P. Lam, “Polarization squeezing of continuous variable Stokes parameters,” *Phys. Rev. Lett.* **88**, 093601 (2002).
- [43] C. C. Gerry and J. Albert, “Finite violations of a bell inequality for high spin: An optical realization,” *Phys. Rev. A* **72**, 043822 (2005).
- [44] P. D. Drummond, “Violations of Bell’s inequality in cooperative states,” *Phys. Rev. Lett.* **50**, 1407–1410 (1983).
- [45] M. D. Reid, W. J. Munro, and F. De Martini, “Violation of multiparticle bell inequalities for low- and high-flux parametric amplification using both vacuum and entangled input states,” *Phys. Rev. A* **66**, 033801 (2002).
- [46] N. D. Mermin, “Quantum mechanics vs local realism near the classical limit: A Bell inequality for spin s ,” *Phys. Rev. D* **22**, 356–361 (1980).

-
- [47] C. C. Gerry, “Remarks on the use of group theory in quantum optics,” *Opt. Express* **8**, 76–85 (2001).
- [48] N. Sridhar and O. Pfister, “Generation of multipartite spin entanglement from multimode squeezed states,” *Phys. Rev. A* **89**, 012310 (2014).
- [49] P. Hyllus and J. Eisert, “Optimal entanglement witnesses for continuous-variable systems,” *New J. Phys.* **8**, 51 (2006).
- [50] D. Gottesman, “Stabilizer codes and quantum error correction,” Ph.D. thesis, California Institute of Technology, Pasadena, CA (1997).
- [51] J. Zhang and S. L. Braunstein, “Continuous-variable Gaussian analog of cluster states,” *Phys. Rev. A* **73**, 032318 (2006).
- [52] R. Raussendorf, J. Harrington, and K. Goyal, “A fault-tolerant one-way quantum computer,” *Ann. Phys. (NY)* **321**, 2242–2270 (2006).
- [53] H. Zaidi, N. C. Menicucci, S. T. Flammia, R. Bloomer, M. Pysher, and O. Pfister, “Entangling the optical frequency comb: simultaneous generation of multiple 2x2 and 2x3 continuous-variable cluster states in a single optical parametric oscillator,” *Laser Phys.* **18**, 659 (2008). Revised version at <http://arxiv.org/pdf/0710.4980v3>.
- [54] N. C. Menicucci, “Continuous-variable cluster states in the optical frequency comb are robust to local errors in the Hamiltonian-connection graph used to make them,” in preparation (2013).
- [55] P. van Loock and S. L. Braunstein, *Quantum Information with Continuous Variables* (Kluwer Academic, 2003), chap. Multipartite entanglement for continuous variables.
- [56] N. C. Menicucci, S. T. Flammia, and P. van Loock, “Graphical calculus for Gaussian pure states with applications to continuous-variable cluster states,” *Phys. Rev. A* **83**, 042335 (2011).
- [57] N. C. Menicucci, “Temporal-mode continuous-variable cluster states using linear optics,” *Phys. Rev. A* **83**, 062314 (2011).
- [58] S. Brierley and A. Higuchi, “On maximal entanglement between two pairs in four-qubit pure states,” *J. Phys. A: Math. Theor.* **40**, 8455–8465 (2007).

- [59] R. Dicke, “Coherence in spontaneous radiation processes,” *Phys. Rev.* **93**, 99 (1954).
- [60] N. Sridhar, R. Shahrokhshahi, A. J. Miller, B. Calkins, T. Gerrits, A. Lita, S. W. Nam, and O. Pfister, “Direct measurement of the Wigner function by photon-number-resolving detection,” *J. Opt. Soc. Am. B* **31**, B34–B40 (2014).
- [61] K. D. Irwin, “An application of electrothermal feedback for high resolution cryogenic particle detection,” *Appl. Phys. Lett.* **66**, 1998–2000 (1995).
- [62] E. Figueroa-Feliciano, B. Cabrera, A. J. Miller, S. F. Powell, T. Saab, and A. B. C. Walker, “Optimal filter analysis of energy-dependent pulse shapes and its application to TES detectors,” *Nucl. Instr. Meth. Phys. Res. A* **444**, 453–456 (2000).
- [63] Z. H. Levine, T. Gerrits, A. L. Migdall, D. V. Samarov, B. Calkins, A. E. Lita, and S. W. Nam, “Algorithm for finding clusters with a known distribution and its application to photon-number resolution using a superconducting transition-edge sensor,” *J. Opt. Soc. Am. B* **29**, 2066–2073 (2012).
- [64] K. Banaszek and K. Wódkiewicz, “Testing quantum nonlocality in phase space,” *Phys. Rev. Lett.* **82**, 2009 (1999).
- [65] A. J. Miller, A. E. Lita, B. Calkins, I. Vayshenker, S. M. Gruber, and S. W. Nam, “Compact cryogenic self-aligning fiber-to-detector coupling with losses below one percent,” *Opt. Express* **19**, 9102–9110 (2011).
- [66] K. Wódkiewicz and J. Eberly, “Coherent states, squeezed fluctuations, and the SU(2) and SU(1,1) groups in quantum-optics applications,” *J. Opt. Soc. Am. B* **2**, 458 (1985).
- [67] Arvind, B. Dutta, N. Mukunda, and R. Simon, “Two-mode quantum systems: Invariant classification of squeezing transformations and squeezed states,” *Phys. Rev. A* **52**, 1609–1620 (1995).
- [68] R. Simon, “Peres-Horodecki separability criterion for continuous variable systems,” *Phys. Rev. Lett.* **84**, 2726 (2000).
- [69] R. N. Alexander, P. Wang, N. Sridhar, M. Chen, O. Pfister, and N. C. Menicucci, “One-way quantum computing with arbitrarily large time-frequency continuous-variable cluster states from a single optical parametric oscillator,” *arXiv:1509.00484 [quant-ph]* **62** (2015).

-
- [70] P. Wang, M. Chen, N. C. Menicucci, and O. Pfister, “Weaving quantum optical frequency combs into hypercubic cluster states,” *Phys. Rev. A* **90**, 032325 (2014).
- [71] M. Chen, N. C. Menicucci, and O. Pfister, “Experimental realization of multipartite entanglement of 60 modes of a quantum optical frequency comb,” *Phys. Rev. Lett.* **112**, 120505 (2014).
- [72] M. A. Nielsen and C. M. Dawson, “Fault-tolerant quantum computation with cluster states,” *Phys. Rev. A* **71**, 042323 (2005).
- [73] N. C. Gabay and N. C. Menicucci, “Local interferometric symmetries for Gaussian pure states,” arXiv:1310.4831 [quant-ph] (2013).
- [74] A. Vourdas, “SU(2) and SU(1,1) phase states,” *Phys. Rev. A* **41**, 1653 (1990).
- [75] S. M. Barnett and D. T. Pegg, “Phase in quantum optics,” *Journal of Physics A: Mathematical and General* **19**, 3849 (1986).
- [76] C. C. Gerry and K. E. Urbanski, “Hermitian phase-difference operator analysis of microscopic radiation-field measurements,” *Phys. Rev. A* **42** (1990).
- [77] J. W. Noh, A. Fougères, and L. Mandel, “Measurement of the quantum phase by photon counting,” *Phys. Rev. Lett.* **67**, 1426–1429 (1991).
- [78] J. R. Torgerson and L. Mandel, “Is there a unique operator for the phase difference of two quantum fields?” *Phys. Rev. Lett.* **76**, 3939–3942 (1996).
- [79] K. L. Pregnell and D. T. Pegg, “Single-shot measurement of quantum optical phase,” *Phys. Rev. D Lett.* **89**, 173601 (2002).
- [80] M. Tsang, J. H. Shapiro, and S. Lloyd, “Quantum theory of optical temporal phase and instantaneous frequency,” *Physical Review A* **78**, 053820 (2008).
- [81] Z. Xie, T. Zhong, S. Shrestha, X. Xu, J. Liang, Y.-X. Gong, J. C. Bienfang, A. Restelli, J. H. Shapiro, F. N. C. Wong, and C. W. Wong, “Harnessing high-dimensional hyperentanglement through a biphoton frequency comb,” *Nature Photonics* p. 536542 (2015).